

Cover Page



Universiteit Leiden



The handle <http://hdl.handle.net/1887/37115> holds various files of this Leiden University dissertation

**Author:** Monti, Adriano

**Title:** Taking control of charge transfer : strategic design for solar cells

**Issue Date:** 2015-12-21

# Taking Control of Charge Transfer: *Strategic Design for Solar Cells*

PROEFSCHRIFT

ter verkrijging van  
de graad van Doctor aan de Universiteit Leiden,  
op gezag van Rector Magnificus prof.mr. C.J.J.M. Stolker,  
volgens besluit van het College voor Promoties  
te verdedigen op maandag 21 december 2015  
klokke 13.45 uur

door

Adriano Monti  
geboren te Milano, Italië  
in 1986

# Promotiecommissie

**Promotor:** Prof. Dr. Huub J. M. de Groot

**Copromotor:** Dr. Francesco Buda

**Overige leden:** Prof. Dr. Jaap Brouwer

Prof. Dr. Marc T. M. Koper

Prof. Dr. Victor S. Batista  
(Yale University, CT, U.S.A)

Prof. Dr. Benedetta Mennucci  
(Università di Pisa, Italy)

Adriano Monti

Taking Control of Charge Transfer: Strategic Design for Solar Cells  
Ph.D. thesis, Leiden University

ISBN: 978-94-6259-970-3

The research discussed in this dissertation was performed in the Solid State NMR/Biophysical Organic Chemistry group at the Leiden Institute of Chemistry. This project was financed by the Nederlandse Organisatie voor Wetenschappelijk Onderzoek (NWO) ECHO project (nr. 713.011.002). The use of supercomputer facilities was sponsored by NWO Physical Sciences.

PRACE-3IP (project FP7 RI-312763) is also acknowledged for granting access to the Boreasz supercomputer at the Interdisciplinary Centre for Mathematical and Computational Modelling (ICM) based in Poland.

Cover designed by Adriano Monti

No part of this thesis may be reproduced in any form without express written permission of the copyright holder.

To my parents, my family, and my grandparents.



# Table of Contents

<b>List of Abbreviation</b>	<b>iv</b>
<b>1. Introduction</b>	<b>1</b>
1.0. Abstract.....	1
1.1. Beyond Fossil Fuel.....	2
1.2. Photovoltaic Cells.....	6
1.2.1. Dye-Sensitized Solar Cell.....	7
1.3. Solar Fuel Cells.....	9
1.4. Electron Transfer.....	12
1.3.1. Marcus Theory.....	13
1.5. Outline of this Thesis.....	18
1.6. References.....	19
<b>2. Theory and Computational Details</b>	<b>25</b>
2.0. Abstract.....	25
2.1. The Born-Oppenheimer Approximation.....	26
2.2. Density Functional Theory.....	30
2.3. Exchange Correlation Functionals.....	34
2.4. Car-Parrinello Molecular Dynamics.....	36
2.4.1. Periodic Boundary Condition and Plane Waves Basis Set.....	37
2.5. Time-Dependent Density Functional Theory (TD-DFT).....	39
2.5.1. Linear Response TD-DFT.....	40
2.6. Constrained Density Functional Theory.....	43
2.7. Semi-Empirical Methods.....	45
2.8. References.....	48
<b>3. Engineering Donor-Antenna-Acceptor Triads for Photoinduced Charge Separation</b>	<b>51</b>
3.0. Abstract.....	51
3.1. Introduction.....	52
3.2. Methods and Computational Details.....	57
3.2.1. Ground State Calculations.....	57
3.2.2. Time-Dependent DFT.....	57

3.2.3. Ground and Excited State Redox Potentials .....	58
3.2.4. Excited State Geometry Optimizations.....	58
3.2.5. Electronic Coupling calculations.....	59
3.2.5.1. Charge Transfer Integral (CTI) Method .....	59
3.2.5.2. Constrained DFT (CDFT) .....	59
3.2.6. Bridge-Mediated Electron Transfer .....	60
3.3. Results and Discussion.....	61
3.3.1. xc-Functional Benchmarking for TD-DFT	
Absorption Spectra .....	62
3.3.2. Redox Potential Calculations .....	64
3.3.3. Optical Excitation and Excited State Geometrical	
Optimizations .....	64
3.3.4. Charge Transfer Integrals and Charge Separation Rates .....	69
3.4. Conclusions .....	73
3.5. References .....	74
3.6. Appendix .....	78
<b>4. Crucial Role of Nuclear Dynamics in Heterogeneous Electron</b>	
<b>Transfer</b>	<b>81</b>
4.0. Abstract.....	81
4.1. Introduction .....	82
4.2. Methods and Computational Details .....	84
4.2.1. Optimization of the Extended Hückel Parameters .....	84
4.2.2. Quantum-Classical Dynamics of hole/electron	
wavepackets .....	86
4.2.3. Normal Mode Analysis.....	90
4.3. Results and Discussion.....	90
4.3.1. The Optimized EH Parameters.....	90
4.3.2. Electron Quantum Dynamics Simulations.....	91
4.4. Conclusions .....	98
4.5. References .....	99
4.6. Appendix .....	103
4.6.1. Test on Geometrical Relaxation in the Excited State .....	103
4.6.2. Test on T-Stilbene-TiO <sub>2</sub> .....	103
<b>5. Fully Atomistic Simulation of Solvent Mediated Proton-Coupled</b>	
<b>Electron Transfer Assisting Photodriven Catalytic Water</b>	
<b>Oxidation</b>	<b>105</b>
5.0. Abstract.....	105
5.1. Introduction .....	106

5.2. Methods and Computational Details .....	109
5.2.1. System 1a: Preparation and Electron Quantum Dynamics Simulations .....	109
5.2.2. System 1b: Preparation, Characterization and Constrained <i>ab initio</i> MD .....	110
5.3. Results and Discussion .....	112
5.3.1. TD-DFT Characterization of the Electronic Excitations of the Dye-Catalyst Complex and Molecular Orbitals Localization .....	112
5.3.2. Photoinduced Electron Injection Dynamics in the Dye-TiO <sub>2</sub> Model .....	113
5.3.3. First PCET Catalytic Water Oxidation Step .....	115
5.4. Conclusions .....	122
5.5. References .....	123
5.6. Appendix .....	126
<b>6. Conclusions and Outlook</b>	<b>129</b>
<b>Summary</b>	<b>133</b>
<b>Samenvatting</b>	<b>137</b>
<b>Curriculum Vitae</b>	<b>140</b>
<b>List of Publications</b>	<b>143</b>



# List of Abbreviations

ADF	:	Amsterdam Density Functional
AO	:	Atomic Orbital
BO	:	Born-Oppenheimer
CB	:	Conduction Band
CDFT	:	Constrained Density Functional Theory
COSMO	:	Continuum Solvation Model
CPMD	:	Carr-Parrinello Molecular Dynamics
CS	:	Charge Separated State
CTI	:	Charge Transfer Integrals
D-A	:	Donor-Acceptor
D-An-A	:	Donor-Antenna-Acceptor
DCM	:	Dichloromethane
DFT	:	Density Functional Theory
DOS	:	Density of States
DS-PEC	:	Dye-Sensitized Photoelectrochemical Cells
DSSC	:	Dye-Sensitized Solar Cell
EA	:	Electron Acceptor
ED	:	Electron Donor
EHT	:	Extended Hückel Theory
EQD	:	Electron Quantum Dynamics
ET	:	Electron Transfer
FMO	:	Frontier Molecular Orbital
FNR	:	Ferredoxin-NADP <sup>+</sup> Reductase
GGA	:	Generalized Gradient Approximation
HF	:	Hartree-Fock
HK	:	Hohenberg-Kohn
HEC	:	Hydrogen Evolving Catalyst
HOMO	:	Highest Occupied Molecular Orbital
LC	:	Long-range Corrected
LDA	:	Local Density Approximation

LUMO	:	Lowest Unoccupied Molecular Orbital
MO	:	Molecular Orbital
NDI <sub>1</sub>	:	2,6-diethoxy-1,4,5,8-diimidenaphthalene
NDI <sub>2</sub>	:	2,6-dicarbonitrile-1,4,5,8-diimidenaphthalene
OEC	:	Oxygen Evolving Center
PBC	:	Periodic Boundary Condition
PCET	:	Proton-Coupled Electron Transfer
PEM	:	Proton Exchange Membrane
PES	:	Potential Energy Surface
Ph	:	Phenyl Ring
Ph	:	Phenyl bridge
PSII	:	Photosystem II
PTZ	:	10,10a-dihydro-4aH-phenothiazine
PW	:	Plane Waves
SP	:	Survival Probability
STO	:	Slater-type orbitals
TD-DFT	:	Time-dependent density functional theory
TDKS	:	Time-dependent Kohn Sham
VB	:	Valence Band
WOC	:	Water Oxidation Catalyst
xc	:	Exchange-Correlation



## Introduction

### **1.0. ABSTRACT**

---

*One of the biggest scientific challenges of our times is to achieve direct conversion of solar energy into electricity or solar fuel, efficiently and cost effectively. This will be needed in the near future in order to avoid not only more serious consequences due to pollution induced climate change, but also to be able to satisfy an ever growing energy demand.*

*Biological systems are able to perform solar energy conversion through the process of photosynthesis, during which light energy is stored in highly energetic sugar bonds. Inspired by this process, the ideal solution to the energy problem would be to produce fuels through artificial photosynthesis. That is, use water and CO<sub>2</sub> as feedstock to produce high-energy chemical compounds exploiting sun light as power source.*

*The design of systems able to undertake this task still represents a phenomenal challenge due to the complexity and the interdependence of the mechanisms involved.*

*This dissertation is concerned with addressing fundamental questions regarding photoinduced charge transfer processes in artificial photosynthesis devices, in order to identify the key features for their design optimization. Through the analysis of donor-acceptor models for artificial photosynthesis, we investigate the photoinduced processes of charge separation, electron injection and water oxidation.*

*It is shown how molecular structural modifications can be used to control the directionality of the photoinduced charge transfer, achieve a stable charge separated state, and prevent charge recombination. It is also found that electron transfer processes are driven by coherent vibronic coupling effects that can be exploited for the design of more efficient devices. Finally, we show how proton-coupled electron transfer plays a central role in driving the process of photoinduced water oxidation in a prototypical photoanode for solar water splitting.*

---

## **1.1. BEYOND FOSSIL FUEL**

Throughout history, mankind has developed the ability to exploit the available natural resources to produce work and wealth in an increasingly more efficient and sophisticated way. As a result, its life expectancy and life quality have increased dramatically.

In the pre-industrial world, despite the use of wind and hydropower, technologies relied primarily on human and animal power, to produce work. They were therefore burdened by huge economic and social costs and able to provide well-being just for a small portion of the society.

In the mid-eighteen century, however, the industrial revolution began. Fossil fuel became the primary energy source for work production. Machineries equipped with internal combustion engines changed the transportation and manufacturing methods around the world. Goods production became soon cheaper and achievable on a mass scale, increasing their accessibility also for the socially less advantaged classes. The widespread electrification and the technologies that came with it, continued the revolution and marked a further step towards modern society.

The improved living conditions dictated a stunning increase in the world population. Modern society accounts in fact for about 7 billion people, while at the beginning of the industrial revolution it was only 700 million, and it is expected to rise up to approximately 10 billion in less than a century<sup>1</sup>.

However, modernization has come at a price. Burning massive amounts of fossil fuels to meet the world's energy demand, releases a large amount of greenhouse gases in the atmosphere, particularly carbon dioxide. Over time, the atmospheric pollution has risen to the point of creating serious climate change which can endanger our way of living. Moreover, the competition between countries for the control over the reserves of fossil fuels represents already a delicate geo-political issue, destined to exacerbate as those reserves will be depleted.

In this context, the research for renewable and environmentally sustainable primary energy carriers that can replace fossil fuel, is of primary importance.

Sustainable, or "green", technologies already exist, such as solar panels, or hydro- and wind-power plants. However, these fossil fuel alternatives generate power in the form of electricity, which is complicated to store and distribute on demand. Moreover, the availability of wind and hydropower sources is strongly bound to specific geographical regions, and the output they can generate may significantly vary on a seasonal base.

The only source of energy virtually inexhaustible, able to fulfil the world's power demand, and globally distributed, although unevenly, is sunlight<sup>2-6</sup>.

The direct conversion of solar power into electrical energy is at present achieved

through photovoltaic cells<sup>7-9</sup>. Unfortunately, the daily intermittency of sunlight, also subject to seasonal changes, is a major drawback of this technology, and ultimately affects the ability of photovoltaics to provide a stable and constant energy flux.

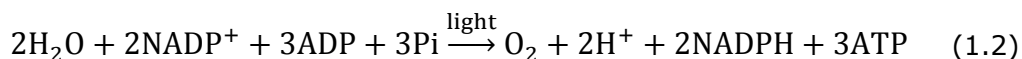
A solution to this problem can be represented by converting sunlight energy into simple chemical bonds<sup>10</sup> while using water as feedstock. The result is the production of oxygen,<sup>11</sup> on one end, and highly energetic and storable chemicals that can be transported and used at convenience, on the other side.

This process, already employed by nature, is called photosynthesis. A schematic representation of the entire photosynthetic mechanism is presented in **Figure 1.1**.

Plants absorb sunlight through their chloroplasts. Once the photonic energy reaches the photosystem II (PSII) inside the chloroplast, specific vibrational modes are enhanced in the protein so that charge separation between a photoexcited electron and an oxidative hole is induced<sup>11</sup>. The oxidative hole created upon charge separation, activates a  $Mn_4CaO_x$  cluster known as oxygen evolving center (OEC). The OEC binds two water molecules, and it is able to store four positive charges or holes. These oxidizing equivalents are used by OEC to oxidize the water molecules to molecular oxygen, four protons and four electrons as



While the molecular oxygen is released, the electrons and protons are moved, through a complex mechanism named electron transport chain, to two different reaction centers NADP<sup>+</sup> reductase and the ATP synthase, where they are ultimately used to reduce NADP<sup>+</sup> and ADP to NADPH and ATP respectively (see **Figure 1.1b**). With the incorporation of equation 1.1, the total equation for the photo-activated mechanism is



Ultimately, the newly generated NADPH and ATP are used in the light independent Calvin cycle to fix atmospheric CO<sub>2</sub> into carbohydrates (see **Figure 1.1a**).

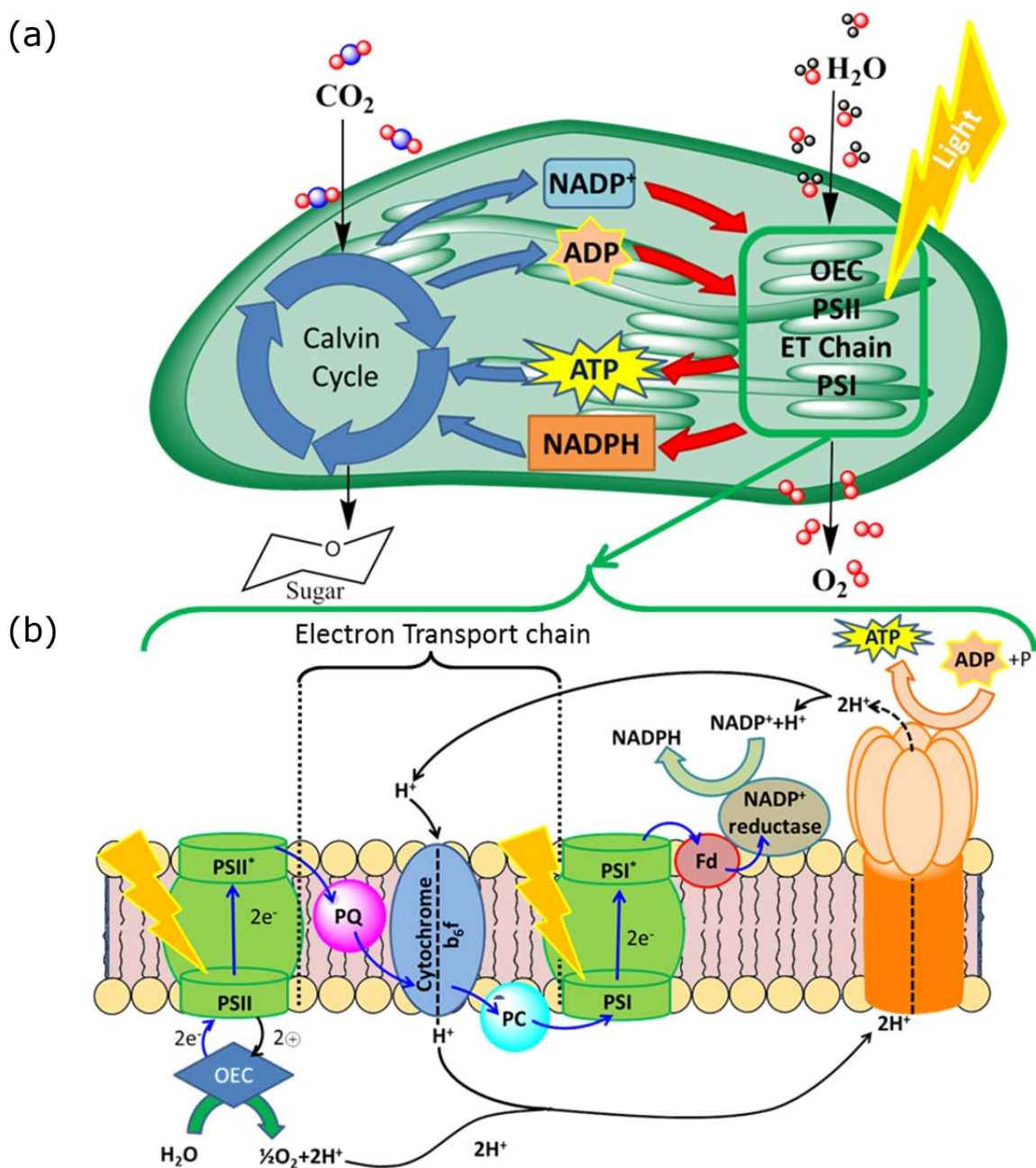


**Figure 1.1.** (a) Schematic representation of the photosynthetic processes leading to the production of molecular oxygen and sugar from water and  $\text{CO}_2$ . These processes also produce the side products  $\text{NADP}^+$ , ADP, ATP and NADPH, necessary for the sustainability of the cycle. (b) Description of the light-dependent reduction mechanism of ADP and  $\text{NADP}^+$  to ATP and NADPH, supported by the concomitant photolysis of water.

The consumption of the carbohydrates in the presence of O<sub>2</sub> releases again CO<sub>2</sub>, making this a perfectly cycle process for fuel production and consumption.

It is therefore not surprising that the development of both photovoltaic and artificial photosynthesis technologies have been inspired by the natural photosynthesis machinery, particularly by PSII<sup>12-17</sup>.

A photon is used to excite the device's antenna and induce a bound electron and hole in the form of an excitonic state. This can then decay into a stable charge separated state (CS), upon mixing of a charge transfer state into the exciton state and transfer of an electron to an electron acceptor subunit, usually a semiconductor material. After reduction of the acceptor/semiconductor, the electron can be either extracted to generate electricity through an external circuit or transferred to a catalytic half-cell for solar fuel production. The first type of device takes the name of photovoltaic cell<sup>2,6,12,18,19</sup>, the second that of solar fuel cell<sup>3,10,20-23</sup>.

In a photovoltaic system, the oxidized chromophore is ultimately reduced by a sacrificial reductant agent, which is then regenerated electrochemically at the cathode side of the cell. In artificial photosynthesis instead, the reduction of the light absorber is achieved by the oxidation of the water oxidation catalyst (WOC). The activated WOC can then catalyze the oxidation of water (equation 1.1), assuming the same role the OEC has in natural photosynthesis.



## 1.2. PHOTOVOLTAIC CELLS

A photovoltaic cell is a device that generate an electrical output through the conversion of sunlight. In such a device, a photon is used to excite a semiconductor and promote one electron from the valence to the conduction band (CB) of the material. By doing so, a hole is created in the valence band (VB) forming, together with the excited electron in CB, the electron-hole pair. The hole and the electron are subsequently driven apart and separately used to power an external circuit.

The first photovoltaic cell was made commercially available over 40 years ago, and was based on a crystalline silicon semiconductor. Silicon based solar cells, are at the moment, still the reference standard for the photovoltaic industry. The efficiency of this type of cells have been greatly improved since the first prototype (<1%) to a current ~25% for a single junction cell, or even ~40% for some state-of-the-art multi-junction cells<sup>24,25</sup>.

Beside their efficiency, the great success of silicon-based solar cells is due to their robustness, which allows for their usage for more than 20 years, and their relatively low maintenance and operating costs. However, this technology suffers from some major drawbacks correlated with the need of pure silicon, which is not encountered as such in nature. In fact, pure silicon crystals must be obtained from the purification of silicates through an expensive and strongly endothermic process, which presents additional difficulties related to the necessity of avoiding any unwanted contamination of the final product.

Although the manufacturing costs have been decreased during the years, and new types of Si-based cells have been developed to overcome some of the previously mentioned problems, a variety of new lines of research, aiming at developing cheaper alternatives for solar cells applications, have been emerging in the past decades. Among them, the dye-sensitized solar cells (DSSC) attract a lot of attention, becoming the subject of a vast research effort, due to low production costs and high power conversion efficiency, which has recently reached >20% for perovskite based devices<sup>26-29</sup>. However, this technology is far from being mature and further investigation is required to improve cell performances. Particularly important is here the study of mechanisms that control the intricate interplay of factors driving the electron transfer processes between components in DSSC. In this field of research, computational chemistry proved to be able to bring a significant contribution, not only through the interpretation of experimental results, but also by proactively provide answers to more fundamental questions, observe processes otherwise experimentally inaccessible, and by inspiring the design of new materials for systematic optimization by molecular engineering<sup>7,19,30-39</sup>.

### 1.2.1. Dye-sensitized solar cells

The concept of dye-sensitized solar cells was first introduced by O'Regan and Grätzel in 1991<sup>13</sup>. In the original DSSC design, the photoanode was composed of a film of titanium dioxide ( $\text{TiO}_2$ ) nanoparticles (**Figure 1.2a**, blue spheres), coated with a light-harvesting ruthenium-based dye (**Figure 1.2a**, red spheres). The anode was immersed in a iodide/triiodide electrolyte solution (**Figure 1.2a**, orange spheres), and contacted with a photocathode for the regeneration of the electrolyte.

Since that first publication, various modifications of the O'Regan and Grätzel original idea have been proposed, where one or more of the original device's components are replaced<sup>12,40-42</sup>. However, the general design of the DSSC has undergone very little modifications, and **Figure 1.2a** can very well represent any modern DSSC device.

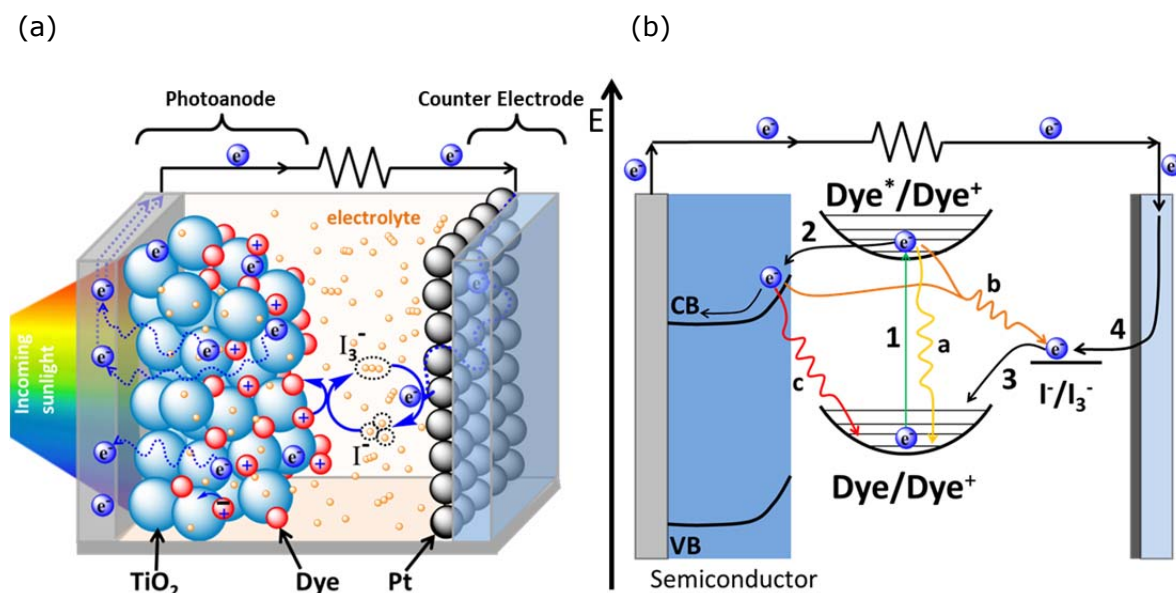


**Figure 1.2** (a) schematic representation of a dye-sensitized solar cell in which the photoanode, constituted by semiconductor nanoparticles (blue spheres) functionalized with a molecular chromophore (red spheres), is immersed in an electrolyte solution containing a redox mediator ( $\text{I}^-/\text{I}_3^-$ , orange spheres). The anode is connected to a counter electrode for the regeneration of the redox mediator through an external circuit (black straight arrows). The zigzag line represents a resistance (or work performed) along the external circuit. (b) energy diagram of the electron transfer processes (black arrows) occurring upon photoexcitation of the molecular chromophore (green arrow), and of the possible recombination paths (wiggly lines) of the excited state to the initial ground state. CB and VB are the abbreviation for conduction and valence band, respectively.

A photovoltaic Grätzel cell ideally cycles through four concatenated steps:

1. A photon of the incoming sunlight is initially absorbed by a dye molecule. The absorption promotes the chromophore into an excited state ( $\text{Dye}^*$ ) via an intramolecular electronic transition from an occupied to an unoccupied molecular orbital (**Figure 1.2b**, green arrow 1).
2. The photogenerated exciton is dissociated upon injection of the excited electron into the semiconductor CB (**Figure 1.2b**, black arrow 2)<sup>43, 44</sup>. The electron can diffuse into the bulk of the semiconductor, and be extracted to perform work at the resistance.
3. At the same time, the oxidized dye molecule ( $\text{Dye}^+$ ) is reduced to its natural charge by a sacrificial reductant present in the electrolyte solution ( $\text{I}/\text{I}_3^-$  redox couple). After regeneration, the chromophore can undergo another photoexcitation cycle.
4. From the external circuit, after performing work, the photogenerated electrons are reintroduced into the cell through the photocathode to reduce the oxidized reductant agent to its original form and complete the cycle.

Unfortunately, along the cycle, the photoexcited electron can also undergo alternative quenching paths, which can affect the efficiency of the cell:

- a) If the injection is not sufficiently fast, the electron may relax into a chromophore state energetically lower than the semiconductor CB edge, thus making the electron injection impossible, or ultimately to the ground state;
- b) it can also recombine with the positive charges carried by the electrolyte if the injection into the semiconductor is delayed, or if, after injection, it remains trapped in the semiconductor defects states;
- c) if trapped, it can also recombine with the oxidized chromophore to reconstitute the ground state configuration.

The efficiency of a dye-sensitized solar cell is therefore dictated by the balance between the desired electronic cycle, and the occurrence of one, or more, of the possible quenching paths. The optimization of the cell performances can therefore be achieved by trying to increase the efficiency of the processes 1, 2, 3, and 4, while decreasing the incidence of the quenching paths (a, b, and c) described above (see **Figure 1.2b**). This is a complicated task since all these processes are strongly correlated, and may be very differently affected by any modification to the cell. This

difficulty in finding the “perfect mix” of cell components has led to a heuristic approach based on a vast production of devices, in which numerous combinations of different chromophore<sup>40,45-49</sup>, electrolytes<sup>38,42,50</sup>, anchoring groups<sup>51-53</sup> and semiconductors<sup>54-57</sup> are explored.

In this scenario, the theoretical and computational study of the fundamental mechanisms underlying the DSSC processes can have a primary role in predicting the effects of modifications for achieving an optimal balance between the devices’ components. In chapter 3 it is discussed how the electronic properties of a molecular charge separator for solar energy conversion can be optimized to achieve unidirectional electron transfer and to prevent charge recombination.

### **1.3.SOLAR FUEL CELLS**

As previously explained, a solar fuel cell has the purpose of converting solar energy into storable chemical fuel by oxidizing water and, at the same time, reducing protons.

This type of cell can be divided into two separated half-cells, where the water oxidation and the proton reduction half-reactions can take place separately from each other. The separation, necessary to efficiently collect the produced molecular oxygen and hydrogen, or other fuel, is obtained by interposing a proton exchange membrane (PEM) between the two half-cells. In the complete system, the anode and the cathode are connected through an external circuit, which allows for the electrons to flow between them.

Depending on the cell design, at least one of the electrodes acts as light absorber. The visible light absorption occurs either directly through the semiconductor if it possesses the correct band gap, or, as in DSSC devices, through a dye molecule functionalizing the surface of the semiconductor based electrode, which therefore acts as primary acceptor for the photoexcited electron.

In a solar fuel cell, the water oxidation and the proton reduction reactions occur respectively at the anode and at the cathode electrodes. The integration of the catalytic properties onto the electrodes can be achieved in various ways.

In some devices, the electrode is fabricated directly with catalytic material, often metal oxide or semiconductor nanoparticles, and acts as both photoabsorber and catalyst. Several designs based on UV- and visible-light absorbing materials have been proposed<sup>58-63</sup>. To increase the number of reactive points, thus accelerating the catalytic reaction and increasing the cell efficiency, the photoelectrodes are often coupled to co-catalysts, which can be either dissolved in the homogeneous phase in.

contact with the electrode, or directly functionalized onto the electrode surface<sup>64-67</sup>. Other systems, employing tandem cell configurations<sup>68-71</sup>, Z-scheme<sup>72,73</sup> structures, or multi-junction devices<sup>14,74,75</sup> to connect water oxidation and proton reduction catalytic sites, have also been suggested.

Inspired by dye-sensitized solar cell devices, a different approach to photo-driven solar fuel production has recently attracted interest in the scientific community. It is based on the use of dye-sensitized semiconductor nanoparticles, coupled to oxygen, or hydrogen, evolving catalysts. These systems take the name of dye-sensitized photoelectrochemical cells (DS-PECs)<sup>15</sup>.

In **Figure 1.3** a schematic energy diagram of the thermodynamics involved in a dye sensitized photoelectrochemical cell is presented.

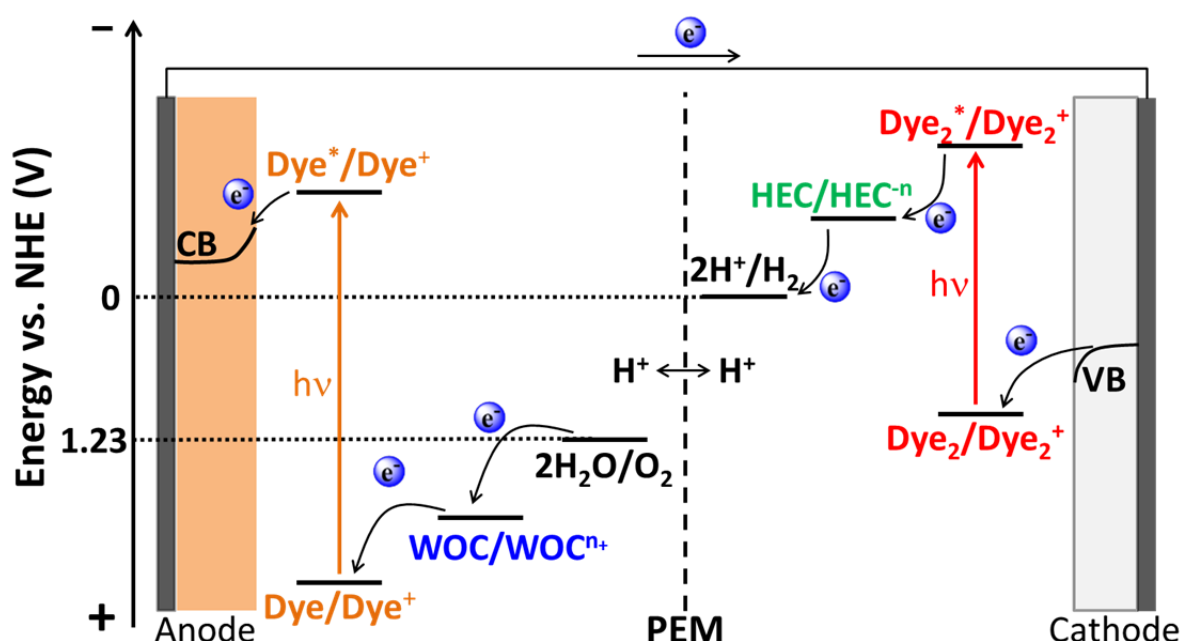


**Figure 1.3.** Structure of a prototypical device for solar fuel production. The photoanode (left) is functionalized with a chromophore and a water oxidation catalyst (WOC). The photocathode (right) is functionalized by a different chromophore and a hydrogen evolving catalyst (HEC). The two electrodes are separated by a proton exchange membrane (PEM) preventing the mixing of molecular hydrogen and oxygen.

As in DSSC devices, the photoexcitation of the dye functionalizing the n-type anodic semiconductor, creates an initial electron-hole pair, which is subsequently dissociated when the excited electron is injected into the semiconductor conduction band. While the injected electron is collected and transferred to the counter electrode, a WOC is activated by reducing the dye to its original form and can undergo the first catalytic step of water oxidation. This removes the need for an electrolyte.

At the cathode, the chromophore is absorbed onto a p-type semiconductor and

contacted with a HEC. Upon photoexcitation, the dye is oxidized by the HEC, acting as electron acceptor, and regenerated to its ground state upon electron transfer from the semiconductor. Using the protons and the electrons derived from the photo-oxidation of water, hydrogen is evolved at the HEC, and the cathodic semiconductor is regenerated.

Since water splitting is a multi-electrons redox reaction (equation 1.1), these processes have to be repeated iteratively several times before molecular hydrogen and oxygen can be released. Multiple charges, or redox equivalents, are therefore accumulated on the WOC and HEC along the cycle. The critical hurdle is to prevent that at each step the previously accumulated redox equivalents quench the excited state of the light absorber.

Examples of DS-PEC integrating both photoactive anode and cathode like in **Figure 1.3** are still very rare<sup>76</sup>, while it remains common practice to optimize the two half-cells separately.

Although significant progress has been recently achieved in the optimization of the cathodic half-cell<sup>77-81</sup>, the four-electron water oxidation reaction at the photoanode, still represents a major design challenge.

The photoanode should integrate both the photoabsorption and the catalytic functions. The difficulties arise from the fact that the chromophore not only must be able to absorb in a wide range of the visible light spectrum and perform fast electron injection into the semiconductor like in the DSSC, but it must be also able to recursively oxidize the WOC and thus drive the water oxidation catalysis.

Different strategies have been proposed to couple both the chromophore and the catalyst units. In the co-absorption strategy, both the chromophore and the catalyst units are bound directly onto the semiconductor surface. In this configuration, upon photoinduced electron injection from the dye into the electrode conduction band, an electron is transferred from the catalyst to the oxidized chromophore nearby. Thus, the activated catalyst can initiate the process of water oxidation. The advantage of this technique is that it allows to use different types of dye to absorb in a wider spectrum of the incident light, and also to increase the chromophore/dye ratio in favor of the latter. This provides a higher number of oxidized dye molecules surrounding the catalyst, thus favoring the completion of the four-step water oxidation process. However, it has been observed that co-absorption may lead to the inhibition of electron injection, probably due to aggregation or interferences between chromophores.

Another strategy, instead, consists in covalently binding the dye and the WOC in a dyad-like structure, where the dye acts as molecular bridge between the semiconductor and the catalyst. This configuration should promote fast through bond

electron transfer between the catalyst and the chromophore, and facilitate the control of the directionality of the process. Additionally, the interposition of the dye in between the oxidized WOC and the reduced semiconductor, enhances the effect of screening of the two charges, therefore stabilizing the charge separated state and reducing the probability of charge recombination.

The investigation of such a system is presented in chapter 5. The study shows how, upon photoinduced electron injection from the dye into the semiconductor, the process of water oxidation is driven by a proton-coupled electron transfer (PCET) mechanism.

Recently, it has become evident that coherent nuclear-electron dynamics has a prominent role in driving intramolecular charge transfer processes<sup>19,82-84</sup>. Therefore, understanding the fundamental mechanisms behind the coherent motion of nuclei and electrons can provide a completely new strategy for the design and optimization of solar fuel cells. The effect of this coherent motion on the electron injection process from a prototypical dye functionalizing a TiO<sub>2</sub> semiconductor surface, is presented in chapter 4 of this thesis.

#### **1.4. ELECTRON TRANSFER**

The term electron transfer (ET), in its simplest definition, describes the transition of one electron between a donor (D) and an acceptor (A) species. When it is triggered by the absorption of a photon from an external light source such as the sun, bringing either D or A in an excited state, this process is referred to as photoinduced electron transfer.

The latter is one of the most pivotal events occurring in natural and artificial photosynthesis, and consequently, a main subject in this thesis.

It can be schematically represented as



where the reactant state ( $D^* + A$ ), obtained through photoexcitation of the donor, evolves into the charge separated product state ( $D^+ + A^-$ ), in concomitance with electron transfer between the two species.

A major contribution in the development of ET theories was brought by the Nobel prize winner Rudolph A. Marcus, who proposed, in 1956, the famous Marcus theory of electron transfer<sup>85</sup>. This is still one of the most important and commonly used tools for the study of electron transfer.

In this section the fundamentals of this theory are presented, together with a brief discussion on its limitations.

### 1.4.1. Marcus Theory

In Marcus theory, electron transfer is described as a sudden event from a donor to an acceptor, with consequent transition from reactant to product state, in response to the creation, due to thermal fluctuations, of favorable conditions along a collective reaction coordinate  $Q$  (see **Figure 1.4**). This collective coordinate accounts for the coordinates of the D-A solute complex, as well as of the solvent molecules surrounding it.

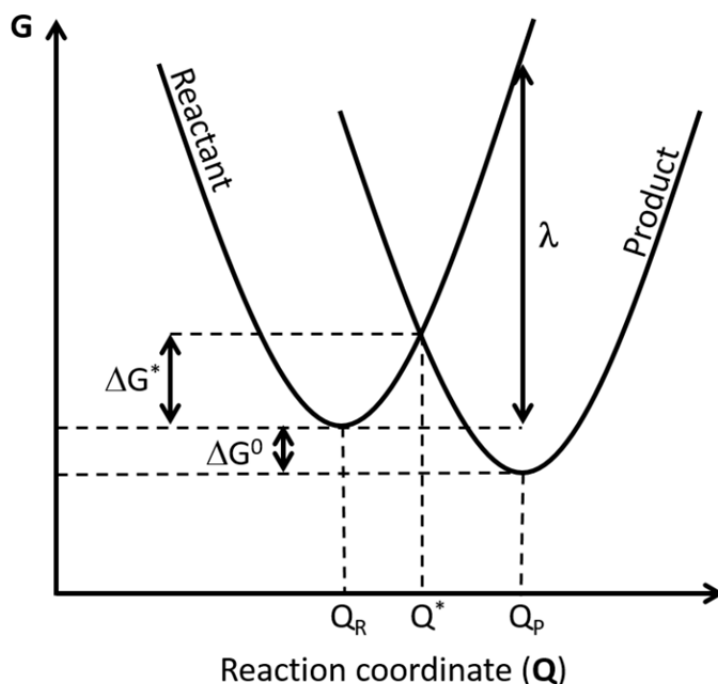


**Figure 1.4.** Representation of the free energy curves of the diabatic reactant and product states along the collective coordinate  $Q$ .  $\Delta G^*$  is the free energy barrier for charge separation,  $\Delta G^0$  is the overall Gibbs free energy change between reactant and product, and  $\lambda$  is the total reorganization energy of the electron transfer process.

As shown in **Figure 1.4**, the free energy curves of the reactant and product states are approximated by two parabolas crossing each other at the transition state  $Q^*$ , and with minima respectively at  $Q_R$  and  $Q_P$ . It is worth noticing that the reactant and product, in this formalism, are diabatic states, since their nature do not vary with changes in the reaction coordinates.

During the electronic jump, the system comprising the donor, the acceptor, and the solvent is assumed stationary, following the Franck-Condon principle, and the energy is conserved. Therefore, the electron tunneling can occur only at the transition state geometry  $Q^*$ , which is communal to both reactant and product state. In other words, every time the system reaches the transition state it exist a possibility for the electron to tunnel from the reactant to the donor state.



This implies that the rate constant for the ET reaction depends on two factors: the probability for the reactant to reach  $Q^*$ , and, once in  $Q^*$ , the probability for the tunneling to occur. The first variable is controlled by the temperature and associated reorganization of the system, while the second one involves the electronic coupling elements between the two diabatic states.

In the adiabatic limit, the electron transfer rate can be expressed by the Arrhenius equation

$$k_{\text{ET}} = k_{\text{el}} \nu_{\text{N}} \exp \left[ \frac{-\Delta G^*}{k_{\text{B}} T} \right], \quad (1.4)$$

where  $k_{\text{el}}$  is the electronic transmission coefficient,  $\nu_{\text{N}}$  is the average nuclear frequency factor, and  $\Delta G^*$  is the activation energy, which is the energy needed to reach the transition state from the minimum of the reactant state free energy surface<sup>86</sup>.

On the basis of the approximation that the reactant and product free energy curves are parabolic, it is possible to define  $\Delta G^*$  through the quadratic expression

$$\Delta G^* = \frac{(\lambda + \Delta G^0)^2}{4\lambda} \quad (1.5)$$

where  $\Delta G^0$  is the free energy difference between reactant and product states in their respective equilibrium configurations, and  $\lambda$  is the reorganization energy. The latter is defined as the energy needed to bring the reactant state into the equilibrium configuration of the product state, before the electron transfer occurs.

$k_{\text{el}}$  in equation 1.4, depends on the electronic coupling between the reactant and product states, and is correlated with the probability of electron transfer to occur at the crossing point between the two potential energy surfaces.

If the two diabatic states are electronically strongly coupled then we can assume  $k_{\text{el}} \approx 1$ . This means that, under these conditions, every time the system is brought by its fluctuations to the crossing point between the reactant and the product states, the probability for the electron tunneling to occur is also  $\approx 1$ . Thus, the electron transfer reaction becomes an adiabatic process, which can be described by a motion along a unique adiabatic energy surface with a barrier between the two minima  $Q_{\text{R}}$  and  $Q_{\text{P}}$ <sup>87</sup>, and where the electrons of the solute system respond immediately to changes in the solvent polarization. Within this so called Marcus adiabatic limit, the electron transfer rate constant is simply determined by the Arrhenius probability of

overcoming the activation free energy barrier through thermal fluctuations (equation 1.4).

In the opposite scenario, where the electronic coupling between reactant and product states is small ( $k_{el} \ll 1$ ), the system needs to explore  $Q^*$  several time before the tunneling takes place. The ET rate constant is therefore strongly dependent on the electronic interaction between initial and final states at the transition state  $Q^*$ , and the process becomes nonadiabatic.

In this nonadiabatic limit, the electron transfer rate constant is given by the Fermi's golden rule<sup>88</sup> expression

$$k_{ET} = \frac{2\pi}{\hbar} \langle \Psi_{D^*A} | \hat{H}^{el} | \Psi_{D+A^-} \rangle^2 FC^{el} \quad (1.6)$$

where  $FC^{el}$  is the thermally averaged nuclear Franck-Condon factor, which contains the overlap integrals between isoenergetic nuclear vibrational wavefunctions belonging to the reactant ( $\Psi_{D^*A}$ ) and product ( $\Psi_{D+A^-}$ ) states, and account for the energetic effects imposed by the nuclear changes following the electron transfer. In the high temperature limit ( $h\nu < k_B T$ ), this term assumes the form:

$$FC^{el} = \left( \frac{1}{4\pi\lambda k_B T} \right)^{1/2} \exp \left[ \frac{-(\Delta G^0 + \lambda)^2}{4\lambda k_B T} \right] \quad (1.7)$$

where  $\lambda$  contains the reorganizational energy terms for both the inner and outer sphere nuclear terms.

The Marcus equation for ET obtained by combining equation 1.6 and 1.7 shows that the electron transfer rate does not behave linearly with respect to the variation of the reaction free energy  $-\Delta G^0$ . Two separate ET regimes can be identified.

In the normal regime, in which  $-\Delta G^0 < \lambda$  (**Figure 1.5a**, normal region), the electron transfer rate ( $k_{ET}$ ) increases as the driving force increases, until a maximum rate is reached for  $-\Delta G^0 = \lambda$ . If this condition is met, the system is in the Marcus optimal point, since the electron transfer becomes a barrierless process.

If the reaction free energy change is further increased beyond the optimal point ( $-\Delta G^0 > \lambda$ , **Figure 1.5a**, inverted region), a counterintuitive observation is made: for increasingly larger driving forces  $k_{ET}$  begins to progressively decrease. This is known as Marcus inverted regime of electron transfer (**Figure 1.5b**, solid line).

The prediction of an inverted regime of electron transfer is one of the most important aspects of Marcus theory, which was observed experimentally, years later,

by Miller and Closs<sup>89,90</sup>. This behavior can be understood by comparing the energy of the crossing point between the reactant and product states in the inverted region, against the optimal point.

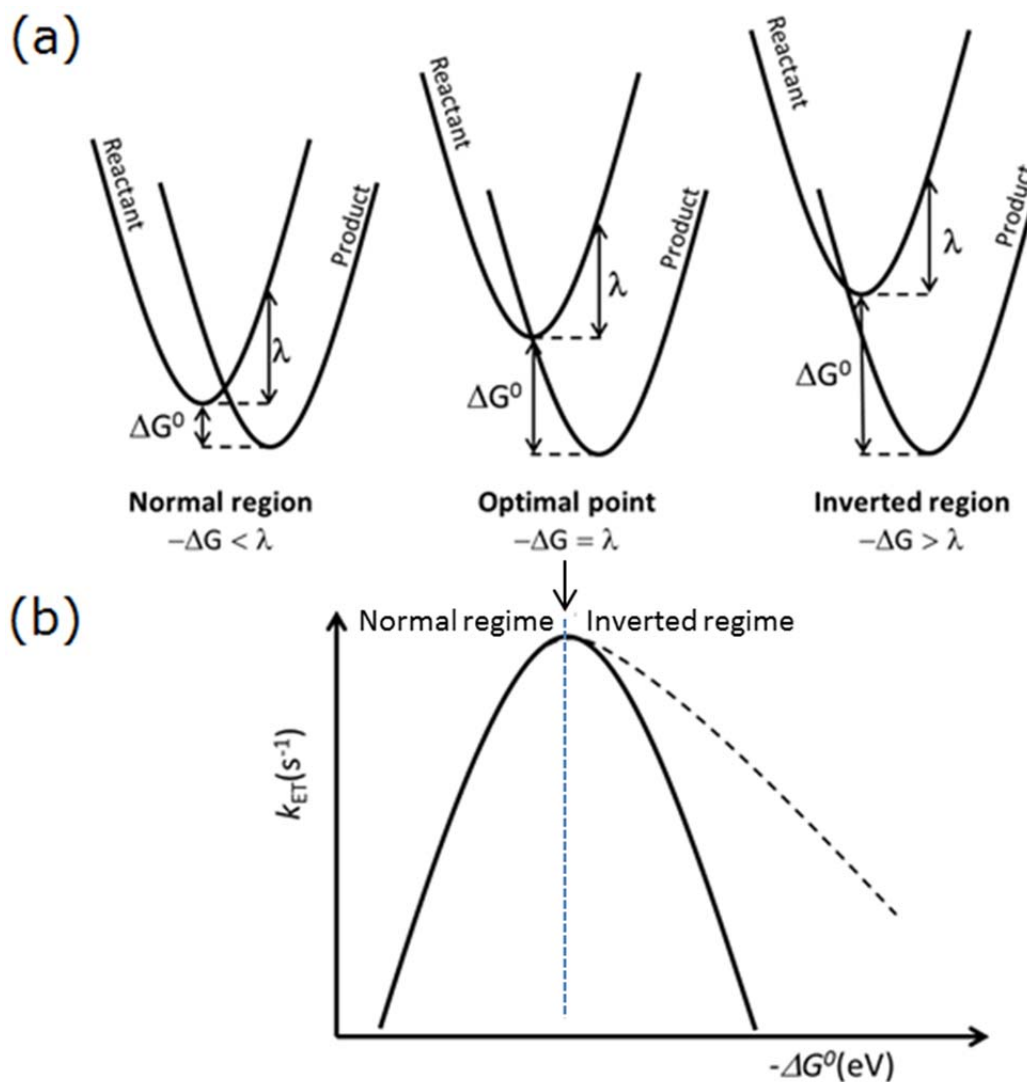


**Figure 1.5** (a) Representation of the different Marcus theory regions, together with the Gibbs free energy difference, and the reorganization energy. (b) Representation of electron transfer rate coefficient dependence on the Gibbs free energy variation predicted by Marcus (solid line), and of its deviation due to electron tunneling effects (black dashed line).

As shown in **Figure 15a**, increasing the value of  $\Delta G^0$  beyond the optimal conditions, results in shifting  $Q^*$  from the minimum of the reactant state curve, to an energetically higher point. This means that additional energy is required to reach the curves crossing point, which in turn decreases the reaction rate.

However, another observation to be made is that, although the classical Marcus expression for ET is extremely powerful in describing processes in the normal and optimal region, it underestimates the values of  $k_{ET}$  for reactions following the

inverted regime. This deviation (**Figure 1.5b**, dashed line) from the classical Marcus picture (solid line) is due to the fact that Marcus considers only classical vibrational modes as available channels for barrier crossing, while ignoring quantum tunneling effects that, in the inverted regime, allow the electron to “see” a thinner barrier, and proceed faster than expected.

The classical Marcus equation can therefore be extended to include intramolecular high frequency quantum modes for the solute, leading to the so called semi-classical Marcus expression<sup>91,92</sup>, in which electron transfer is treated as the sum of vibronic transitions from quantum levels of the reactant, to those of the product state<sup>93,94</sup>.

### **1.5. OUTLINE OF THIS THESIS**

The Marcus theory of electron transfer is very powerful in predicting the behavior of organic redox materials. Thus, it has become one of the fundamental tools for the analysis of materials for solar cell applications.

In chapter 3 of this thesis, Marcus theory is used as theoretical basis to judge the quality of the design of different molecular rectifiers, with respect to the predicted electron transfer rate constants. The influence of different structural modifications on the Marcus parabolic term variables,  $\Delta G$  and  $\lambda$ , and on the electronic coupling between donor and acceptor, is used to find an optimized design able to achieve fast and unidirectional charge transfer.

Marcus theory is however an equilibrium theory. That is, it was initially developed to describe outer sphere electron transfer events, driven by the slow reorganization of the solvent, between a reactant and a product state at the equilibrium configurations. However, photoinduced electron transfer is usually not an equilibrium process, and occurs on time scales much shorter than those of solvent rearrangement. This implies that, although Marcus theory may give an accurate rate value for the overall electron transfer process on long time scales, it can give very little information on how the transfer dynamically proceeds.

Recently, it has been shown that the photoinduced electron transfer in natural and artificial systems is controlled by quantum coherence effects between nuclei and electrons. Therefore, the ability of identifying the vibrational modes coupled to the electron transfer dynamics can represent an important advantage for the design and the optimization of molecular systems for solar cell applications.

In chapter 4 it is shown how specific vibrational modes of a molecular chromophore designed to achieve unidirectional electron transfer, can drive the photoinduced electron injection into  $\text{TiO}_2$ , thereby suggesting how to modify the system to improve its performance.

Another example of coupled electron-nuclear motion is given in chapter 5, where the oxidation of water, occurring at a dye-sensitized photoanode, is shown to proceed through a proton-coupled electron transfer mechanism initiated by photoinduced electron injection into a semiconductor.

**1.6. REFERENCES**

- (1) Chu, S.; Majumdar, A. Opportunities and Challenges for a Sustainable Energy Future. *Nature* **2012**, *488* (7411), 294–303.
- (2) Cook, T. R.; Dogutan, D. K.; Reece, S. Y.; Surendranath, Y.; Teets, T. S.; Nocera, D. G. Solar Energy Supply and Storage for the Legacy and Nonlegacy Worlds. *Chem. Rev.* **2010**, *110* (11), 6474–6502.
- (3) Gust, D.; Moore, T. A.; Moore, A. L. Solar Fuels via Artificial Photosynthesis. *Acc. Chem. Res.* **2009**, *42* (12), 1890–1898.
- (4) Faunce, T.; Styring, S.; Wasielewski, M. R.; Brudvig, G. W.; Rutherford, A. W.; Messinger, J.; Lee, A. F.; Hill, C. L.; deGroot, H.; Fontecave, M.; et al. Artificial Photosynthesis as a Frontier Technology for Energy Sustainability. *Energy Environ. Sci.* **2013**, *6* (4), 1074–1076.
- (5) Lewis, N. S.; Nocera, D. G. Powering the Planet: Chemical Challenges in Solar Energy Utilization. *Proc. Natl. Acad. Sci.* **2006**, *103* (43), 15729–15735.
- (6) Nozik, A. J.; Miller, J. Introduction to Solar Photon Conversion. *Chem. Rev.* **2010**, *110* (11), 6443–6445.
- (7) De Angelis, F. Modeling Materials and Processes in Hybrid/Organic Photovoltaics: From Dye-Sensitized to Perovskite Solar Cells. *Acc. Chem. Res.* **2014**, *47* (11), 3349–3360.
- (8) Berardi, S.; Drouet, S.; Francàs, L.; Gimbert-Suriñach, C.; Guttentag, M.; Richmond, C.; Stoll, T.; Llobet, A. Molecular Artificial Photosynthesis. *Chem. Soc. Rev.* **2014**, *43* (22), 7501–7519.
- (9) Coridan, R. H.; Nielander, A. C.; Francis, S. A.; McDowell, M. T.; Dix, V.; Chatman, S. M.; Lewis, N. Methods for Comparing the Performance of Energy-Conversion Systems for Use in Solar Fuels and Solar Electricity Generation. *Energy Environ. Sci.* **2015**.
- (10) Walter, M. G.; Warren, E. L.; McKone, J. R.; Boettcher, S. W.; Mi, Q.; Santori, E. A.; Lewis, N. S. Solar Water Splitting Cells. *Chem. Rev.* **2010**, *110* (11), 6446–6473.
- (11) Eisenmayer, T. J.; de Groot, H. J. M.; van de Wetering, E.; Neugebauer, J.; Buda, F. Mechanism and Reaction Coordinate of Directional Charge Separation in Bacterial Reaction Centers. *J. Phys. Chem. Lett.* **2012**, *3* (6), 694–697.
- (12) Hagfeldt, A.; Boschloo, G.; Sun, L.; Kloo, L.; Pettersson, H. Dye-Sensitized Solar Cells. *Chem. Rev.* **2010**, *110* (11), 6595–6663.
- (13) O'Regan, B.; Grätzel, M. A Low-Cost, High-Efficiency Solar Cell Based on Dye-Sensitized Colloidal TiO<sub>2</sub> Films. *Nature* **1991**, *353* (6346), 737–740.
- (14) Nattestad, A.; Mozer, A. J.; Fischer, M. K. R.; Cheng, Y. B.; Mishra, A.; Bauerle, P.; Bach, U. Highly Efficient Photocathodes for Dye-Sensitized Tandem Solar Cells. *Nat. Mater.* **2010**, *9* (1).
- (15) Yu, Z.; Li, F.; Sun, L. Recent Advances in Dye-Sensitized Photoelectrochemical Cells for Solar Hydrogen Production Based on Molecular Components. *Energy Environ. Sci.* **2015**, *8* (3), 760–775.
- (16) Megiatto Jr, J. D.; Méndez-Hernández, D. D.; Tejeda-Ferrari, M. E.; Teillout, A.-L.; Llansola-Portolés, M. J.; Kodis, G.; Poluektov, O. G.; Rajh, T.; Mujica, V.; Groy, T. L.; et al. A Bioinspired Redox Relay That Mimics Radical Interactions of the Tyr–His Pairs of Photosystem II. *Nat. Chem.* **2014**, *6* (5), 423–428.
- (17) Wang, T.; Brudvig, G. W.; Batista, V. S. Study of Proton Coupled Electron Transfer in a Biomimetic Dimanganese Water Oxidation Catalyst with Terminal Water Ligands. *J. Chem. Theory Comput.* **2010**, *6* (8), 2395–2401.
- (18) Bairu, S. G.; Mghanga, E.; Hasan, J.; Kola, S.; Rao, V. J.; Bhanuprakash, K.; Giribabu, L.; Wiederrecht, G. P.; da Silva, R.; Rego, L. G. C.; et al. Ultrafast Interfacial Charge-Transfer Dynamics in a Donor- $\pi$ -Acceptor Chromophore Sensitized TiO<sub>2</sub> Nanocomposite. *J. Phys. Chem. C* **2013**, *117* (9), 4824–4835.

- (19) Nieto-Pescador, J.; Abraham, B.; Gundlach, L. Photoinduced Ultrafast Heterogeneous Electron Transfer at Molecule–Semiconductor Interfaces. *J. Phys. Chem. Lett.* **2014**, *5* (20), 3498–3507.
- (20) Kim, D.; Sakimoto, K. K.; Hong, D.; Yang, P. Artificial Photosynthesis for Sustainable Fuel and Chemical Production. *Angew. Chem. Int. Ed.* **2015**, *54* (11), 3259–3266.
- (21) Tachibana, Y.; Vayssieres, L.; Durrant, J. R. Artificial Photosynthesis for Solar Water-Splitting. *Nat. Photonics* **2012**, *6* (8), 511–518.
- (22) Young, K. J.; Martini, L. A.; Milot, R. L.; Snoeberger III, R. C.; Batista, V. S.; Schmuttenmaer, C. A.; Crabtree, R. H.; Brudvig, G. W. Light-Driven Water Oxidation for Solar Fuels. *Coord. Chem. Rev.* **2012**, *256* (21–22), 2503–2520.
- (23) Ding, X.; Gao, Y.; Zhang, L.; Yu, Z.; Liu, J.; Sun, L. Visible Light-Driven Water Splitting in Photoelectrochemical Cells with Supramolecular Catalysts on Photoanodes. *ACS Catal.* **2014**, *4* (7), 2347–2350.
- (24) King, R. R.; Law, D. C.; Edmondson, K. M.; Fetzer, C. M.; Kinsey, G. S.; Yoon, H.; Sherif, R. A.; Karam, N. H. 40% Efficient Metamorphic GaInP/GaInAs/Ge Multijunction Solar Cells. *Appl. Phys. Lett.* **2007**, *90* (18), 183516.
- (25) Aho, A.; Tukiainen, A.; Polojärvi, V.; Guina, M. Performance Assessment of Multijunction Solar Cells Incorporating GaInNAsSb. *Nanoscale Res. Lett.* **2014**, *9* (1), 61.
- (26) Yang, W. S.; Noh, J. H.; Jeon, N. J.; Kim, Y. C.; Ryu, S.; Seo, J.; Seok, S. I. SOLAR CELLS. High-Performance Photovoltaic Perovskite Layers Fabricated through Intramolecular Exchange. *Science* **2015**, *348* (6240), 1234–1237.
- (27) Jeon, N. J.; Noh, J. H.; Yang, W. S.; Kim, Y. C.; Ryu, S.; Seo, J.; Seok, S. I. Compositional Engineering of Perovskite Materials for High-Performance Solar Cells. *Nature* **2015**, *517* (7535), 476–480.
- (28) Sun, L. Perovskite Solar Cells: Crystal Crosslinking. *Nat. Chem.* **2015**, *7* (9), 684–685.
- (29) Li, X.; Dar, M. I.; Yi, C.; Luo, J.; Tschumi, M.; Zakeeruddin, S. M.; Nazeeruddin, M. K.; Han, H.; Grätzel, M. Improved Performance and Stability of Perovskite Solar Cells by Crystal Crosslinking with Alkylphosphonic Acid  $\Omega$ -Ammonium Chlorides. *Nat. Chem.* **2015**, *7* (9), 703–711.
- (30) Sobuś, J.; Karolczak, J.; Komar, D.; Anta, J. A.; Ziółek, M. Transient States and the Role of Excited State Self-Quenching of Indoline Dyes in Complete Dye-Sensitized Solar Cells. *Dyes Pigments* **2015**, *113*, 692–701.
- (31) Chapman, C. T.; Liang, W.; Li, X. Ultrafast Coherent Electron–Hole Separation Dynamics in a Fullerene Derivative. *J. Phys. Chem. Lett.* **2011**, *2* (10), 1189–1192.
- (32) Hoff, D. A.; da Silva, R.; Rego, L. G. C. Coupled Electron–Hole Quantum Dynamics on D–n–A Dye-Sensitized TiO<sub>2</sub> Semiconductors. *J. Phys. Chem. C* **2012**, *116* (40), 21169–21178.
- (33) Meng, S.; Kaxiras, E. Electron and Hole Dynamics in Dye-Sensitized Solar Cells: Influencing Factors and Systematic Trends. *Nano Lett.* **2010**, *10* (4), 1238–1247.
- (34) Listorti, A.; O’Regan, B.; Durrant, J. R. Electron Transfer Dynamics in Dye-Sensitized Solar Cells. *Chem. Mater.* **2011**, *23* (15), 3381–3399.
- (35) Ma, W.; Zhang, F.; Meng, S. Dye-Sensitized Solar Cells: Atomic Scale Investigation of Interface Structure and Dynamics. *Chin. Phys. B* **2014**, *23* (8), 086801.
- (36) Caprasecca, S.; Mennucci, B. Excitation Energy Transfer in Donor-Bridge-Acceptor Systems: A Combined Quantum-Mechanical/Classical Analysis of the Role of the Bridge and the Solvent. *J. Phys. Chem. A* **2014**, *118* (33), 6484–6491.
- (37) Duncan, W. R.; Craig, C. F.; Prezhdo, O. V. Time-Domain Ab Initio Study of Charge Relaxation and Recombination in Dye-Sensitized TiO<sub>2</sub>. *J. Am. Chem. Soc.* **2007**, *129* (27), 8528–8543.

- (38) Mathew, S.; Yella, A.; Gao, P.; Humphry-Baker, R.; Curchod, B. F. E.; Ashari-Astani, N.; Tavernelli, I.; Rothlisberger, U.; Nazeeruddin, M. K.; Grätzel, M. Dye-Sensitized Solar Cells with 13% Efficiency Achieved through the Molecular Engineering of Porphyrin Sensitizers. *Nat. Chem.* **2014**, *6* (3), 242–247.
- (39) Akimov, A. V.; Neukirch, A. J.; Prezhdo, O. V. Theoretical Insights into Photoinduced Charge Transfer and Catalysis at Oxide Interfaces. *Chem. Rev.* **2013**, *113* (6), 4496–4565.
- (40) Urbani, M.; Grätzel, M.; Nazeeruddin, M. K.; Torres, T. Meso-Substituted Porphyrins for Dye-Sensitized Solar Cells. *Chem. Rev.* **2014**, *114* (24), 12330–12396.
- (41) Roy-Mayhew, J. D.; Aksay, I. A. Graphene Materials and Their Use in Dye-Sensitized Solar Cells. *Chem. Rev.* **2014**, *114* (12), 6323–6348.
- (42) Wu, J.; Lan, Z.; Lin, J.; Huang, M.; Huang, Y.; Fan, L.; Luo, G. Electrolytes in Dye-Sensitized Solar Cells. *Chem. Rev.* **2015**, *115* (5), 2136–2173.
- (43) Ribó, J. M.; Bofill, J. M.; Crusats, J.; Rubires, R. Point-Dipole Approximation of the Exciton Coupling Model Versus Type of Bonding and of Excitons in Porphyrin Supramolecular Structures. *Chem. – Eur. J.* **2001**, *7* (13), 2733–2737.
- (44) Huijser, A.; Savenije, T. J.; Kroeze, J. E.; Siebbeles, L. D. A. Exciton Diffusion and Interfacial Charge Separation in Meso-Tetraphenylporphyrin/TiO<sub>2</sub> Bilayers: Effect of Ethyl Substituents. *J. Phys. Chem. B* **2005**, *109* (43), 20166–20173.
- (45) Kim, K.-H.; Lee, S.-M.; Seo, M.-H.; Cho, S.-E.; Hwang, W.-P.; Park, S.-H.; Kim, Y.-K.; Lee, J.-K.; Kim, M.-R. Syntheses of Organic Dyes Based on Phenothiazine as Photosensitizers and Effects of Their  $\Pi$ -Conjugated Bridges on the Photovoltaic Performances of Dye-Sensitized Solar Cells. *Macromol. Res.* **2012**, *20* (2), 128–137.
- (46) Kishore, R. S. K.; Kel, O.; Banerji, N.; Emery, D.; Bollot, G.; Mareda, J.; Gomez-Casado, A.; Jonkheijm, P.; Huskens, J.; Maroni, P.; et al. Ordered and Oriented Supramolecular N/p-Heterojunction Surface Architectures: Completion of the Primary Color Collection. *J. Am. Chem. Soc.* **2009**, *131* (31), 11106–11116.
- (47) Sakai, N.; Mareda, J.; Vauthey, E.; Matile, S. Core-Substituted Naphthalenediimides. *Chem. Commun.* **2010**, *46* (24), 4225–4237.
- (48) Martini, L. A.; Moore, G. F.; Milot, R. L.; Cai, L. Z.; Sheehan, S. W.; Schmuttenmaer, C. A.; Brudvig, G. W.; Crabtree, R. H. Modular Assembly of High-Potential Zinc Porphyrin Photosensitizers Attached to TiO<sub>2</sub> with a Series of Anchoring Groups. *J. Phys. Chem. C* **2013**, *117* (28), 14526–14533.
- (49) Pei, K.; Wu, Y.; Islam, A.; Zhu, S.; Han, L.; Geng, Z.; Zhu, W. Dye-Sensitized Solar Cells Based on Quinoxaline Dyes: Effect of  $\Pi$ -Linker on Absorption, Energy Levels, and Photovoltaic Performances. *J. Phys. Chem. C* **2014**, *118* (30), 16552–16561.
- (50) Yella, A.; Lee, H.-W.; Tsao, H. N.; Yi, C.; Chandiran, A. K.; Nazeeruddin, M. K.; Diao, E. W.-G.; Yeh, C.-Y.; Zakeeruddin, S. M.; Grätzel, M. Porphyrin-Sensitized Solar Cells with Cobalt (II/III)-Based Redox Electrolyte Exceed 12 Percent Efficiency. *Science* **2011**, *334* (6056), 629–634.
- (51) Ambrosio, F.; Martsinovich, N.; Troisi, A. What Is the Best Anchoring Group for a Dye in a Dye-Sensitized Solar Cell? *J. Phys. Chem. Lett.* **2012**, *3* (11), 1531–1535.
- (52) Xiao, D.; Martini, L. A.; Snoeberger, R. C.; Crabtree, R. H.; Batista, V. S. Inverse Design and Synthesis of Acac-Coumarin Anchors for Robust TiO<sub>2</sub> Sensitization. *J. Am. Chem. Soc.* **2011**, *133* (23), 9014–9022.
- (53) Ernstorfer, R.; Gundlach, L.; Felber, S.; Storck, W.; Eichberger, R.; Willig, F. Role of Molecular Anchor Groups in Molecule-to-Semiconductor Electron Transfer†. *J. Phys. Chem. B* **2006**, *110* (50), 25383–25391.



- (54) Tebby, Z.; Uddin, T.; Nicolas, Y.; Olivier, C.; Toupance, T.; Labrugère, C.; Hirsch, L. Low-Temperature UV Processing of Nanoporous SnO<sub>2</sub> Layers for Dye-Sensitized Solar Cells. *ACS Appl. Mater. Interfaces* **2011**, *3* (5), 1485–1491.
- (55) Zheng, H.; Tachibana, Y.; Kalantar-zadeh, K. Dye-Sensitized Solar Cells Based on WO<sub>3</sub>. *Langmuir* **2010**, *26* (24), 19148–19152.
- (56) Diamant, Y.; Chappel, S.; Chen, S. G.; Melamed, O.; Zaban, A. Core-shell Nanoporous Electrode for Dye Sensitized Solar Cells: The Effect of Shell Characteristics on the Electronic Properties of the Electrode. *Coord. Chem. Rev.* **2004**, *248* (13–14), 1271–1276.
- (57) Lenzmann, F.; Krueger, J.; Burnside, S.; Brooks, K.; Grätzel, M.; Gal, D.; Rühle, S.; Cahen, D. Surface Photovoltage Spectroscopy of Dye-Sensitized Solar Cells with TiO<sub>2</sub>, Nb<sub>2</sub>O<sub>5</sub>, and SrTiO<sub>3</sub> Nanocrystalline Photoanodes: Indication for Electron Injection from Higher Excited Dye States. *J. Phys. Chem. B* **2001**, *105* (27), 6347–6352.
- (58) Kato, H.; Asakura, K.; Kudo, A. Highly Efficient Water Splitting into H<sub>2</sub> and O<sub>2</sub> over Lanthanum-Doped NaTaO<sub>3</sub> Photocatalysts with High Crystallinity and Surface Nanostructure. *J. Am. Chem. Soc.* **2003**, *125* (10), 3082–3089.
- (59) Lutterman, D. A.; Surendranath, Y.; Nocera, D. G. A Self-Healing Oxygen-Evolving Catalyst. *J. Am. Chem. Soc.* **2009**, *131* (11), 3838–3839.
- (60) Sfirloaga, P.; Miron, I.; Malaescu, I.; Marin, C. N.; Ianasi, C.; Vlazan, P. Structural and Physical Properties of Undoped and Ag-Doped NaTaO<sub>3</sub> Synthesized at Low Temperature. *Mater. Sci. Semicond. Process.* **2015**, *39*, 721–725.
- (61) Busser, G. W.; Mei, B.; Weide, P.; Vesborg, P. C. K.; Stührenberg, K.; Bauer, M.; Huang, X.; Willinger, M.-G.; Chorkendorff, I.; Schlögl, R.; et al. Cocatalyst Designing: A Regenerable Molybdenum-Containing Ternary Cocatalyst System for Efficient Photocatalytic Water Splitting. *ACS Catal.* **2015**, 5530–5539.
- (62) Zou, Z.; Ye, J.; Sayama, K.; Arakawa, H. Direct Splitting of Water under Visible Light Irradiation with an Oxide Semiconductor Photocatalyst. *Nature* **2001**, *414* (6864), 625–627.
- (63) Fujishima, A.; Honda, K. Electrochemical Photolysis of Water at a Semiconductor Electrode. *Nature* **1972**, *238* (5358), 37–38.
- (64) Maeda, K.; Teramura, K.; Lu, D.; Takata, T.; Saito, N.; Inoue, Y.; Domen, K. Photocatalyst Releasing Hydrogen from Water. *Nature* **2006**, *440* (7082), 295–295.
- (65) Moriya, Y.; Takata, T.; Domen, K. Recent Progress in the Development of (oxy)nitride Photocatalysts for Water Splitting under Visible-Light Irradiation. *Coord. Chem. Rev.* **2013**, *257* (13–14), 1957–1969.
- (66) Zhang, G.; Kim, G.; Choi, W. Visible Light Driven Photocatalysis Mediated via Ligand-to-Metal Charge Transfer (LMCT): An Alternative Approach to Solar Activation of Titania. *Energy Environ. Sci.* **2014**, *7* (3), 954–966.
- (67) Cao, S.; Chen, Y.; Hou, C.-C.; Lv, X.-J.; Fu, W.-F. Cobalt Phosphide as a Highly Active Non-Precious Metal Cocatalyst for Photocatalytic Hydrogen Production under Visible Light Irradiation. *J. Mater. Chem. A* **2015**, *3* (11), 6096–6101.
- (68) Grätzel, M. Photoelectrochemical Cells. *Nature* **2001**, *414* (6861), 338–344.
- (69) Duret, A.; Grätzel, M. Visible Light-Induced Water Oxidation on Mesoscopic A-Fe<sub>2</sub>O<sub>3</sub> Films Made by Ultrasonic Spray Pyrolysis. *J. Phys. Chem. B* **2005**, *109* (36), 17184–17191.
- (70) Xu, M.; Zai, J.; Yuan, Y.; Qian, X. Band Gap-Tunable (CuIn)<sub>x</sub>Zn<sub>2(1-x)</sub>S<sub>2</sub> Solid Solutions: Preparation and Efficient Photocatalytic Hydrogen Production from Water under Visible Light without Noble Metals. *J. Mater. Chem.* **2012**, *22* (45), 23929–23934.
- (71) Iii, J. W. A.; Shaner, M.; Walczak, K.; Sharp, I. D.; Ardo, S. Experimental Demonstrations of Spontaneous, Solar-Driven Photoelectrochemical Water Splitting. *Energy Environ. Sci.* **2015**.

- (72) Maeda, K.; Higashi, M.; Lu, D.; Abe, R.; Domen, K. Efficient Nonsacrificial Water Splitting through Two-Step Photoexcitation by Visible Light Using a Modified Oxynitride as a Hydrogen Evolution Photocatalyst. *J. Am. Chem. Soc.* **2010**, *132* (16), 5858–5868.
- (73) Chen, S.; Qi, Y.; Hisatomi, T.; Ding, Q.; Asai, T.; Li, Z.; Ma, S. S. K.; Zhang, F.; Domen, K.; Li, C. Efficient Visible-Light-Driven Z-Scheme Overall Water Splitting Using a  $\text{MgTa}_2\text{O}_6\text{-xNy/TaON}$  Heterostructure Photocatalyst for  $\text{H}_2$  Evolution. *Angew. Chem.* **2015**, *127* (29), 8618–8621.
- (74) Brillet, J.; Yum, J.-H.; Cornuz, M.; Hisatomi, T.; Solarska, R.; Augustynski, J.; Graetzel, M.; Sivula, K. Highly Efficient Water Splitting by a Dual-Absorber Tandem Cell. *Nat. Photonics* **2012**, *6* (12), 824–828.
- (75) Reece, S. Y.; Hamel, J. A.; Sung, K.; Jarvi, T. D.; Esswein, A. J.; Pijpers, J. J. H.; Nocera, D. G. Wireless Solar Water Splitting Using Silicon-Based Semiconductors and Earth-Abundant Catalysts. *Science* **2011**, *334* (6056), 645–648.
- (76) Fan, K.; Li, F.; Wang, L.; Daniel, Q.; Gabrielsson, E.; Sun, L. Pt-Free Tandem Molecular Photoelectrochemical Cells for Water Splitting Driven by Visible Light. *Phys. Chem. Chem. Phys.* **2014**, *16* (46), 25234–25240.
- (77) Wu, L.-Z.; Chen, B.; Li, Z.-J.; Tung, C.-H. Enhancement of the Efficiency of Photocatalytic Reduction of Protons to Hydrogen via Molecular Assembly. *Acc. Chem. Res.* **2014**, *47* (7), 2177–2185.
- (78) Wang, M.; Han, K.; Zhang, S.; Sun, L. Integration of Organometallic Complexes with Semiconductors and Other Nanomaterials for Photocatalytic  $\text{H}_2$  Production. *Coord. Chem. Rev.* **2015**, *287*, 1–14.
- (79) Ruberu, T. P. A.; Dong, Y.; Das, A.; Eisenberg, R. Photoelectrochemical Generation of Hydrogen from Water Using a CdSe Quantum Dot-Sensitized Photocathode. *ACS Catal.* **2015**, *5* (4), 2255–2259.
- (80) Li, L.; Duan, L.; Wen, F.; Li, C.; Wang, M.; Hagfeldt, A.; Sun, L. Visible Light Driven Hydrogen Production from a Photo-Active Cathode Based on a Molecular Catalyst and Organic Dye-Sensitized P-Type Nanostructured NiO. *Chem. Commun.* **2012**, *48* (7), 988–990.
- (81) Ji, Z.; He, M.; Huang, Z.; Ozkan, U.; Wu, Y. Photostable P-Type Dye-Sensitized Photoelectrochemical Cells for Water Reduction. *J. Am. Chem. Soc.* **2013**, *135* (32), 11696–11699.
- (82) Fuller, F. D.; Pan, J.; Gelzinis, A.; Butkus, V.; Senlik, S. S.; Wilcox, D. E.; Yocum, C. F.; Valkunas, L.; Abramavicius, D.; Ogilvie, J. P. Vibronic Coherence in Oxygenic Photosynthesis. *Nat. Chem.* **2014**, *6* (8), 706–711.
- (83) Andrea Rozzi, C.; Maria Falke, S.; Spallanzani, N.; Rubio, A.; Molinari, E.; Brida, D.; Maiuri, M.; Cerullo, G.; Schramm, H.; Christoffers, J.; et al. Quantum Coherence Controls the Charge Separation in a Prototypical Artificial Light-Harvesting System. *Nat. Commun.* **2013**, *4*, 1602.
- (84) Falke, S. M.; Rozzi, C. A.; Brida, D.; Maiuri, M.; Amato, M.; Sommer, E.; Sio, A. D.; Rubio, A.; Cerullo, G.; Molinari, E.; et al. Coherent Ultrafast Charge Transfer in an Organic Photovoltaic Blend. *Science* **2014**, *344* (6187), 1001–1005.
- (85) Marcus, R. A. On the Theory of Oxidation-Reduction Reactions Involving Electron Transfer. I. *J. Chem. Phys.* **1956**, *24* (5), 966–978.
- (86) Arrhenius S. A. Über Die Dissociationswärme Und Den Einfluß Der Temperatur Auf Den Dissociationsgrad Der Elektrolyte. *Z Phys. Chem* *4*, 96–116.
- (87) Spargaglione, M.; Mukamel, S. Adiabatic vs. Nonadiabatic Electron Transfer and Longitudinal Solvent Dielectric Relaxation: Beyond the Debye Model. *J. Phys. Chem.* **1987**, *91* (15), 3938–3943.
- (88) Dirac, P. a. M. The Quantum Theory of the Emission and Absorption of Radiation. *Proc. R. Soc. Lond. Math. Phys. Eng. Sci.* **1927**, *114* (767), 243–265.

- (89) Miller, J. R.; Calcaterra, L. T.; Closs, G. L. Intramolecular Long-Distance Electron Transfer in Radical Anions. The Effects of Free Energy and Solvent on the Reaction Rates. *J. Am. Chem. Soc.* **1984**, *106* (10), 3047–3049.
- (90) Closs, G. L.; Miller, J. R. Intramolecular Long-Distance Electron Transfer in Organic Molecules. *Science* **1988**, *240* (4851), 440–447.
- (91) Jortner, J. Temperature Dependent Activation Energy for Electron Transfer between Biological Molecules. *J. Chem. Phys.* **1976**, *64* (12), 4860–4867.
- (92) Freed, K. F.; Jortner, J. Multiphonon Processes in the Nonradiative Decay of Large Molecules. *J. Chem. Phys.* **1970**, *52* (12), 6272–6291.
- (93) Weinberg, D. R.; Gagliardi, C. J.; Hull, J. F.; Murphy, C. F.; Kent, C. A.; Westlake, B. C.; Paul, A.; Ess, D. H.; McCafferty, D. G.; Meyer, T. J. Proton-Coupled Electron Transfer. *Chem. Rev.* **2012**, *112* (7), 4016–4093.
- (94) Hammes-Schiffer, S. Theoretical Perspectives on Proton-Coupled Electron Transfer Reactions. *Acc. Chem. Res.* **2001**, *34* (4), 273–281.

## Theory and Computational Methodology

### **2.0.ABSTRACT**

---

*This chapter is meant to provide the reader with a general overview of the computational methodology applied throughout this thesis and explain their theoretical basis.*

*The chapter is structured as follows. At first, a general description of the Born-Oppenheimer approximation is presented (section 2.1). Then, an introduction to the theoretical basis of the density functional theory (DFT) method (section 2.2) and a brief discussion on the most commonly used type of approximations for the exchange-correlation functional (section 2.3) are given.*

*The Car-Parrinello Molecular Dynamics method, which unifies DFT and classical MD, is described in section 2.4, while section 2.5 is dedicated to the description of the theoretical basis of Time-dependent DFT (TD-DFT) and linear-response TD-DFT.*

*Finally, in the last two sections of this chapter (2.6 and 2.7), the constrained DFT method, employed in chapter 3 for the electron coupling calculations, and the semiempirical Hückel and Extended Hückel theories are explained. The latter, together with the Car-Parrinello MD method, is central to the work presented in chapter 4 and chapter 5.*

---

## 2.1. THE BORN-OPPENHEIMER APPROXIMATION

In its most general form, the time-dependent Schrödinger equation can be written as

$$\hat{H}_{\text{tot}}\Psi = i\hbar \frac{\partial}{\partial t}\Psi, \quad (2.1)$$

where  $\Psi$  is the total wavefunction,  $i$  is the imaginary unit,  $t$  represents the time,  $\hbar$  is the reduced Planck constant, and  $\hat{H}_{\text{tot}}$  is the total Hamiltonian of the system under investigation. The latter contains both the nuclear and electronic kinetic-energy operators, and the potential-energy operators describing particles interactions:

$$\hat{H}_{\text{tot}} = \hat{T}_{\text{nuc}} + \hat{T}_{\text{el}} + \hat{V}_{\text{nuc,nuc}} + \hat{V}_{\text{el,el}} + \hat{V}_{\text{nuc,el}} \quad (2.2)$$

In a more explicit form, for a system with  $N$  nuclei and  $n$  electrons, the nuclear ( $\hat{T}_{\text{nuc}}$ ) and electronic ( $\hat{T}_{\text{el}}$ ) kinetic-energy operators can be written as

$$\hat{T}_{\text{nuc}} = - \sum_{I=1}^N \frac{\hbar^2}{2m_I} \nabla_I^2 \quad (2.3)$$

$$\hat{T}_{\text{el}} = - \sum_{i=1}^n \frac{\hbar^2}{2m} \nabla_i^2 \quad (2.4)$$

The potential-energy operators, describing in order the nucleus-nucleus, electron-electron, and nucleus-electron Coulomb interactions, can be expressed as

$$\hat{V}_{\text{nuc,nuc}} = \sum_{I=1}^N \sum_{J>I}^N \frac{1}{4\pi\epsilon_0} \frac{Z_I Z_J e^2}{|\mathbf{R}_I - \mathbf{R}_J|} \quad (2.5)$$

$$\hat{V}_{\text{el,el}} = \sum_{i=1}^n \sum_{j>i}^n \frac{1}{4\pi\epsilon_0} \frac{e^2}{|\mathbf{r}_i - \mathbf{r}_j|} \quad (2.6)$$

$$\hat{V}_{\text{el,nuc}} = - \sum_{I=1}^N \sum_{i=1}^n \frac{1}{4\pi\epsilon_0} \frac{Z_I e^2}{|\mathbf{R}_I - \mathbf{r}_i|} \quad (2.7)$$

In this notation the capital indexes refer to the nuclei, while the small ones point to the electrons.  $Z_I$  and  $-e$  are the atomic number of the  $I^{\text{th}}$  nucleus, and the electron charge, while  $\mathbf{R}_I$  and  $\mathbf{r}_i$  represent the coordinates of the  $I^{\text{th}}$  nucleus and  $i^{\text{th}}$

electron. Finally,  $\epsilon_0$  is the vacuum permittivity and the masses of nuclei and electrons are respectively referred to as  $m_I$  and  $m$ .

The Schrödinger equation (equation 2.1), combined with the expression of the total Hamiltonian  $\hat{H}_{\text{tot}}$  (equation 2.2), implies a direct dependency of the total wavefunction  $\Psi$  on the entire set of nuclear and electronic coordinates as well as on time,  $\Psi(\mathbf{R}, \mathbf{r}, t)$ .

Unfortunately, an analytical solution of equation 2.1 cannot be found in general. A first simplification of this problem can be achieved by factorizing the wavefunction into terms depending on different variables. In this way it is possible to separate equation 2.1 into simpler equations.

Due to the large mass difference between nuclei and electrons  $m_I \gg m$ , the electrons generally move much faster than the nuclei and can therefore instantaneously respond to changes in the nuclear configuration.

This regime is known as the Born-Oppenheimer (BO) approximation<sup>1</sup> and allows to consider nuclear and electronic motions separately. The total wavefunction can be written as a product between electronic  $\psi_i(\mathbf{r}; \mathbf{R})$  and nuclear  $\chi_i(\mathbf{R}, t)$  wavefunctions, according to

$$\Psi(\mathbf{R}, \mathbf{r}, t) = \sum_{i=1}^{\infty} \psi_i(\mathbf{r}; \mathbf{R}) \chi_i(\mathbf{R}, t). \quad (2.8)$$

The electronic wavefunctions are parametrically dependent on the nuclear coordinates that define the "external" potential energy field  $\hat{V}_{\text{el,nuc}}$  experienced by the electrons. This implies that, if we assume the nuclei to be fixed in a specific nuclear configuration  $\{\mathbf{R}\}$ , we can solve the electronic Schrödinger equation

$$\hat{H}_{\text{el}} \psi_i(\mathbf{r}; \mathbf{R}) = E_{\text{el},i}(\mathbf{R}) \psi_i(\mathbf{r}; \mathbf{R}) \quad (2.9)$$

and calculate the electronic eigenfunctions and eigenvalues that uniquely correspond to that specific geometrical configuration. The electronic Hamiltonian is then defined as  $\hat{H}_{\text{el}} = \hat{H}_{\text{tot}} - \hat{T}_{\text{nuc}}$ , or

$$\hat{H}_{\text{el}} = \hat{T}_{\text{el}} + \hat{V}_{\text{nuc,nuc}} + \hat{V}_{\text{el,el}} + \hat{V}_{\text{nuc,el}}. \quad (2.10)$$

The combination of equation 2.1 and 2.9, solved for a specific electronic wavefunction  $\psi_j$  gives the equation

$$\left(\hat{T}_{\text{nuc}} + E_{\text{el},j}(\mathbf{R})\right) \chi_j(\mathbf{R}, t) + \sum_{i=1}^{\infty} \hat{C}_{ji} \chi_i(\mathbf{R}, t) = i\hbar \frac{\partial}{\partial t} \chi_j(\mathbf{R}, t) \quad (2.11)$$

where

$$\hat{C}_{ji} = \sum_{I=1}^N \frac{\hbar^2}{m_I} \int_{\Omega_{\text{TOT}}} d\mathbf{r} \psi_j^*(\mathbf{r}; \mathbf{R}) \left( -\frac{1}{2} [\nabla_I^2 \psi_i(\mathbf{r}; \mathbf{R})] - [\nabla_I \psi_i(\mathbf{r}; \mathbf{R})] \nabla_I \right) \quad (2.12)$$

Here, and throughout the whole thesis, the integration over the spatial coordinates  $\mathbf{r}$  runs over the entire space  $\Omega_{\text{TOT}}$ .

Due to the large difference between nuclear and electronic masses, in the Born-Oppenheimer approximation the  $\hat{C}_{ji}$  coefficients can be considered negligible and this leads to the effective Schrödinger equation

$$\left(\hat{T}_{\text{nuc}} + E_{\text{el},j}(\mathbf{R})\right) \chi_j(\mathbf{R}, t) = i\hbar \frac{\partial}{\partial t} \chi_j(\mathbf{R}, t). \quad (2.13)$$

This equation shows clearly that the nuclei move on a potential energy surface (PES) given by the  $\hat{H}_{\text{el}}$  expectation value  $E_{\text{el},j}(\mathbf{R})$ .

The Born-Oppenheimer approximation is generally sufficient. However, when two electronic states are close in energy or cross each other, the approximation introduced in equation 2.12 is not applicable and the  $\hat{C}_{ji}$  coefficients have to be, at least in part, calculated.

One way to improve the BO approximation is through the so called *adiabatic correction*<sup>2</sup>. It consists in the introduction of a first order correction to the BO electronic energy to account for nuclear motion. This is done by including only the  $\hat{C}_{ji}$  coefficients of equation 2.12 for which  $i = j$ . These terms are rather easy to calculate, but they usually introduce very small corrections.

More important are the  $\hat{C}_{ji}$  terms for which  $i \neq j$ , also called *nonadiabatic* coupling terms. The inclusion of these terms is essential to study nuclear dynamics in regions where near-degeneracy between different adiabatic states occurs. This is the case for many photochemical reactions. Nonadiabatic crossings are also involved during the photoinduced charge transfer processes which are subject of this thesis.

The most commonly employed methodologies for the description of nonadiabatic dynamics of a system are the Ehrenfest dynamics and the surface hopping

algorithm<sup>3-5</sup>. In Ehrenfest dynamics the nuclei move according to the mean force induced by the time-evolution of the electronic wavefunction. Instead, in surface hopping the electronic wavefunction follows the motion of the nuclei on a specific PES. The transition between two adiabatic states occurs, based on their nonadiabatic coupling, according to a stochastic algorithm.

First principles implementations of these methodologies are currently available. However, their applicability is hampered by high computational costs, which can limit the size of the studied system and the time scale of the simulations.

In this thesis a different strategy is adopted in which a unitary transformation is used to move from an adiabatic to a diabatic description of the system at each time step. The quantum evolution of the electronic wavefunction is performed in the molecular orbital adiabatic base for a fixed set of nuclear coordinates, while the nuclear positions are evolved in the atomic orbital diabatic base.

Together with a semiempirical description of the electronic structure, this method allows for quantum-classical study of heterogeneous electron transfer processes on a time scale of picoseconds.



## 2.2. DENSITY FUNCTIONAL THEORY

Every wavefunction method dedicated to electronic structure calculations is based on the same principles: an initial ansatz for the total wavefunction is proposed, which is progressively optimized through the variational principle to minimize the energy expectation value. The energy is therefore a functional of the electronic wavefunction.

The total wavefunction is, however, a very complicated object, which depends on  $3n$  electronic coordinates, where  $n$  is the number of interacting electrons, and whose complexity increases with the dimension of the system. This implies that the application of such methods becomes computationally infeasible for chemical systems with large  $n$ .

The limited applicability of wavefunction-based methodologies is the main motivation for the success that density functional theory (DFT) is experiencing in the last decades.

Based on a completely different theoretical approach, DFT does not aim for the optimal approximation to the total wavefunction, but rather describes a many-electron system based on its ground state density  $\rho(\mathbf{r})$ , which is a function only of 3 spatial coordinates:

$$\rho(\mathbf{r}_1) = n \int_{\Omega_{\text{TOT}}} d\mathbf{r}_2 \dots d\mathbf{r}_n \int_{s^{\uparrow\downarrow}} |\Psi(\mathbf{r}_1 s_1 \mathbf{r}_2 s_2 \dots \mathbf{r}_n s_n)|^2 ds_1 ds_2 \dots ds_n \quad (2.14)$$

where  $\mathbf{r}_i$  and  $s_i$  indicate the electron coordinates and the spin variables. The integration runs over  $n - 1$  spatial coordinates and all spin variables.

The foundations of this theory were first laid down by Hohenberg and Kohn in 1964<sup>6</sup> through two theorems.

The first theorem states that if the ground state electron density of the system under investigation is known, it is possible to construct the Hamiltonian, determine the wavefunction, and consequently extract any observable of the system. It can be in fact demonstrated that a bijective mapping exists between the nuclear-electron interaction or external potential,  $\hat{V}_{\text{ext}}$ , the ground state electronic wavefunction  $\Psi$ , and the electron density  $\rho$

$$\hat{V}_{\text{ext}} \leftrightarrow \Psi \leftrightarrow \rho \quad (2.15)$$

such that to a particular external potential corresponds a unique electron density, and vice versa.

This relation implies that every observable of the system is a functional of the electron density, including the ground state energy

$$\begin{aligned}
 E[\rho] &= \langle \Psi[\rho] | \hat{T} + \hat{V}_{\text{el,el}} + \hat{V}_{\text{ext}} | \Psi[\rho] \rangle \\
 &= \int_{\Omega_{\text{TOT}}} \rho(\mathbf{r}) v_{\text{ext}}(\mathbf{r}) d\mathbf{r} + F_{\text{HK}}[\rho],
 \end{aligned} \tag{2.16}$$

where

$$F_{\text{HK}}[\rho] = T[\rho] + V_{\text{el,el}}[\rho] \tag{2.17}$$

is a universal density functional independent of the external potential, named Hohenberg-Kohn (HK) functional. It has to be noted that the employed Hamiltonian (equation 2.16) differs from equation 2.2 in the following: i) the kinetic operator involves only the kinetics of the electrons since the nuclei are assumed to be fixed; ii) the nucleus-nucleus term is not included since it is a constant term that can be added to the total electronic energy at a later stage; iii) the electron-nuclear term is described as  $\hat{V}_{\text{ext}}$ , an external potential that could in principle include other contributions than the electrostatic field from the nuclei.

The second HK theorem states that for a given density the corresponding energy functional will have an absolute minimum at the ground state energy  $E_0$ . The exact ground state density  $\rho_0$  is the one associated with the lowest energy, and can be found through the minimization of  $E[\rho]$  according to equation 2.16.

Unfortunately, these theorems do not provide an explicit form for the universal functional  $F_{\text{HK}}[\rho]$ , but merely prove that such a functional exists and, once known, can yield the ground state density  $\rho_0$  and the system properties.

To address this problem, Kohn and Sham postulated in 1965<sup>7</sup> that for every system with  $n$  interacting electrons moving in an external potential  $v_{\text{ext}}$ , a local external potential  $v_s$  exists that acts on an hypothetical reference system of  $n$  non-interacting fermions, in such a way that the density of the non-interacting and interacting systems match, *i.e.*  $\rho_s(\mathbf{r}) = \rho(\mathbf{r})$ .

Since the particles of this reference system do not interact, the exact ground state wavefunction can be described as a single Slater determinant, whose orbitals  $\phi_i$  are obtained by solving the equations

$$\left[-\frac{1}{2}\nabla^2 + v_s(\mathbf{r})\right]\phi_i(\mathbf{r}) = \varepsilon_i\phi_i(\mathbf{r}), \quad (2.18)$$

where only the kinetic energy and the one-body local external potential terms  $v_s(\mathbf{r})$  appear. In equation 2.18, and for the remaining of this chapter, we use atomic units to simplify the notation. The total density of the non-interacting system is therefore obtained as

$$\rho_s(\mathbf{r}) = \sum_{i=1}^n |\phi_i(\mathbf{r})|^2 \quad (2.19)$$

As previously said, an exact form of the energy functional for the interacting system cannot be written since an expression for the electronic kinetic energy and the electron-electron repulsion terms of equation 2.17 are unknown.

However, it is possible to approximate the term for the electron-electron repulsion energy  $V_{\text{el,el}}[\rho]$  as a sum between a classical Coulomb interaction term  $J[\rho]$  and a non-classical part  $V_{\text{NC}}[\rho]$

$$\begin{aligned} V_{\text{el,el}}[\rho] &= J[\rho] + V_{\text{NC}}[\rho] \\ &= \left( \frac{1}{2} \int_{\Omega_{\text{TOT}}} d\mathbf{r}_1 \int_{\Omega_{\text{TOT}}} d\mathbf{r}_2 \left[ \frac{\rho(\mathbf{r}_1)\rho(\mathbf{r}_2)}{r_{12}} \right] \right) + V_{\text{NC}}[\rho] \end{aligned} \quad (2.20)$$

Using the same approach, it is also possible to approximate the kinetic energy functional as the sum between the kinetic energy of the non-interacting system  $T_s[\rho]$  and the kinetic correlation energy term  $T_c[\rho]$

$$T[\rho] = T_s[\rho] + T_c[\rho] = \left( \sum_{i=1}^n \langle \phi_i | -\frac{\nabla^2}{2} | \phi_i \rangle \right) + T_c[\rho] \quad (2.21)$$

The functional for the total energy can therefore be rewritten as

$$E[\rho] = T_s[\rho] + V_{\text{ext}}[\rho] + J[\rho] + E_{\text{xc}}[\rho] + V_{\text{nuc,nuc}} \quad (2.22)$$

where  $E_{\text{xc}}[\rho] = V_{\text{NC}}[\rho] + T_c[\rho]$  is the exchange-correlation (xc) functional. In equation 2.22 we have now included also the nucleus-nucleus energy term  $V_{\text{nuc,nuc}}$ .

Since the form of  $v_s(\mathbf{r})$  is unknown, so are the electron densities  $\rho_s(\mathbf{r}) = \rho(\mathbf{r})$ , and consequently the orbitals of the non-interacting system  $\{\phi_i\}$ .

Under the constraint that the density is normalized to the number of electrons  $n$ , the minimization of the energy from equation 2.22 with respect to the density leads to the expression of the Kohn-Sham equations

$$\left[ -\frac{\nabla^2}{2} + v_{\text{ext}}(\mathbf{r}) + \int_{\Omega_{\text{TOT}}} \frac{\rho(\mathbf{r}')}{|\mathbf{r} - \mathbf{r}'|} d\mathbf{r}' + v_{\text{xc}}(\mathbf{r}) \right] \phi_i(\mathbf{r}) = \varepsilon_i \phi_i(\mathbf{r}) \quad (2.23)$$

where the potential  $v_{\text{xc}}(\mathbf{r})$  depends on the approximation chosen for the functional  $E_{\text{xc}}[\rho]$  (see section 2.3).

The self-consistent solution of equations 2.23 leads to a set of one-electron orbitals  $\{\phi_i(\mathbf{r})\}_n$  that generate the electron density for the interacting system

$$\rho(\mathbf{r}) = \sum_{i=1}^n |\phi_i(\mathbf{r})|^2 \quad (2.24)$$

### 2.3. EXCHANGE-CORRELATION FUNCTIONALS

The exact form of  $E_{xc}[\rho]$  in the Kohn-Sham formalism is unknown and has to be approximated. Therefore, the quality of the DFT results depends on how accurately this functional is approximated.

The Local Density Approximation (LDA) is an approximation for the exchange-correlation term in which it is assumed that the system behaves locally as a uniform electron gas:

$$E_{xc}^{LDA}[\rho] = \int_{\Omega_{TOT}} \varepsilon_{xc}^{hom}(\rho(\mathbf{r})) \rho(\mathbf{r}) d\mathbf{r}. \quad (2.25)$$

Here,  $\varepsilon_{xc}^{hom}(\rho(\mathbf{r}))$  is the exchange-correlation energy per particle of the uniform electron gas of charge density  $\rho(\mathbf{r})$ . This function is most commonly parametrized based on the very accurate results obtained from Quantum Monte Carlo calculations on homogeneous electron gases at different densities<sup>8-12</sup>.

The LDA is most suited for the treatment of systems with slow-varying densities, such as metals and semiconductors. However, it has been proved to perform poorly for molecular systems where the electron density is strongly inhomogeneous.

To account for the non-homogeneity of the electron density, a first approximation of the xc-functional  $E_{xc}[\rho]$  beyond LDA must include not only the information about the local density  $\rho(\mathbf{r})$  at a particular position  $\mathbf{r}$ , but also about the gradient of the density at that position:  $\nabla\rho(\mathbf{r})$ . This approximation takes the name of Generalized Gradient Approximation (GGA)

$$E_{xc}^{GGA}[\rho, \nabla\rho] = \int_{\Omega_{TOT}} \varepsilon_{xc}^{hom}(\rho(\mathbf{r})) \rho(\mathbf{r}) d\mathbf{r} + \int_{\Omega_{TOT}} F_{xc}[\rho(\mathbf{r}), \nabla\rho(\mathbf{r})] \rho(\mathbf{r}) d\mathbf{r} \quad (2.26)$$

Here  $F_{xc}[\rho(\mathbf{r}), \nabla\rho(\mathbf{r})]$  is the factor which depends on the approach adopted in writing the xc-functional. In fact, several different GGA functionals have been developed to address specific requirements. Among the most popular GGA xc-functionals we can mention: BP (exchange functional from Becke<sup>13,14</sup>, and correlations according to Perdew<sup>15</sup>), PBE<sup>16</sup> (both exchange and correlation parts developed by Perdew, Burke and Ernzerhof) and BLYP (exchange functional according to Becke<sup>13</sup>, and the Lee-Yang-Parr correlation functional<sup>17</sup>).

Another class of approximation to  $E_{xc}[\rho]$  for DFT are the so called hybrid

functionals, in which a fraction of exact Hartree-Fock (HF) exchange energy is added to the exchange and correlation from pure DFT functionals.

The exact HF exchange is calculated in terms of the Kohn-Sham orbitals as

$$E_x^{\text{HF}} = -\frac{1}{2} \sum_{i,j}^{\text{occ}} \int_{\Omega_{\text{TOT}}} d\mathbf{r}_1 \int_{\Omega_{\text{TOT}}} d\mathbf{r}_2 \phi_i^*(\mathbf{r}_1) \phi_j^*(\mathbf{r}_1) \frac{1}{r_{12}} \phi_i(\mathbf{r}_2) \phi_j(\mathbf{r}_2) \quad (2.27)$$

and their general form is

$$E_{\text{xc}}^{\text{hybrid}} = cE_x^{\text{HF}} + (1 - c)E_x^{\text{DFT}} + E_c^{\text{DFT}} \quad (2.28)$$

where  $c$  is the coefficient that determines the extent by which the HF and the DFT exchange are mixed. A variety of hybrid functionals have been developed where the amount of HF exchange energy included varies.

A remarkably popular hybrid functional is the xc-functional B3LYP (Becke<sup>13</sup>, 3 parameters, Lee-Yang-Parr<sup>17</sup>), which is defined as

$$E_{\text{xc}}^{\text{B3LYP}} = c_0 E_x^{\text{HF}} + (1 - c_0) E_x^{\text{S}} + c_x E_x^{\text{B88}} + (1 - c_c) E_c^{\text{VWN}} + c_c E_c^{\text{LYP}} \quad (2.29)$$

where  $c_0 = 0.20$ ,  $c_x = 0.72$ ,  $c_c = 0.81$ . These parameters control the ratio between the Becke 88 (B88)<sup>13</sup> and Slater (S)<sup>18</sup> exchange functionals, the Lee-Yang-Parr (LYP)<sup>17</sup> and Vosko-Wilk-Nusair (VWN)<sup>9</sup> correlation functionals, and the Hartree-Fock (HF) integral.

GGA and hybrid functionals are very effective in describing properties depending on short-range effects of the exchange and correlation energy terms. However, they are unsuccessful in describing properties where the long-range behavior of the xc-potential is important, such as the description of charge transfer excitations or the polarizability of extended conjugated systems. The reason behind this failure can be found in the local character of their xc-potentials, which induces a qualitatively wrong asymptotic behavior of the exchange potential<sup>19-22</sup>.

To overcome this problem, the class of the long-range corrected (LC) functionals has been developed. The basic idea of these functionals is to achieve a correct asymptotic behavior by partitioning the electron repulsion operator into short and long-range terms. At short range, the GGA exchange is maintained while the exact HF exchange is asymptotically introduced via a range-separated Coulomb attenuation method which ensures a smooth transition between the two different

ranges<sup>19-22</sup>.

A particular LC-functional which has been widely used to study charge-transfer excitations is CAM-B3LYP<sup>19</sup>. In chapter 3 of this thesis, we make use of this functional to compute charge-transfer excitations and optimize excited state geometries, within the framework of time-dependent DFT (TD-DFT, see section 2.5).

## 2.4. CAR-PARRINELLO MOLECULAR DYNAMICS

The Car-Parrinello Molecular Dynamics<sup>23</sup> (CPMD) method was proposed in 1985 to unify classical MD simulations with DFT methods.

In this approach the nuclei move, according to classical mechanics, in an electron-induced effective potential, which is computed by solving the electronic time-evolving problem “on the fly”.

In the Car-Parrinello MD, the electronic degrees of freedom are treated as fictitious dynamical variables. Their evolution is carried on in parallel with the ionic dynamics, avoiding however energy exchange between the two subsystems.

The energy of the electronic subsystem can be considered a functional of the one-particle orbitals set  $\{\psi_i\}$ . Therefore, given an appropriate Lagrangian<sup>24</sup>, the derivative of the electronic energy with respect to the orbitals yields the forces acting on the orbitals and the electrons can be evolved as classical particles.

The Lagrangian postulated by Car and Parrinello takes the form

$$\begin{aligned} \mathcal{L}_{CP} = & \sum_{I=1}^N \frac{1}{2} M_I \dot{R}_I^2 + \sum_{i=1}^n \frac{1}{2} \mu_i \langle \dot{\psi}_i | \dot{\psi}_i \rangle - E^{KS}[\{R_I\}, \{\psi_i\}] \\ & + \sum_{i,j=1}^n \lambda_{ij} (\langle \psi_i | \psi_j \rangle - \delta_{ij}) \end{aligned} \quad (2.30)$$

The first and the second terms of equation 2.30 are the classical kinetic energy of the nuclei and the fictitious kinetic energy of the KS electronic orbitals, respectively.  $E^{KS}[\{R_I\}, \{\psi_i\}]$  is the Kohn-Sham energy density functional, while the last term in the Lagrangian is the constraint needed to impose the orthonormality of the KS orbitals.

Like in classical mechanics, the Car-Parrinello equations of motion are obtained from the Euler-Lagrange equations

$$M_I \ddot{R}_I(t) = -\nabla_I E^{KS}[\{R_I\}, \{\psi_i\}] \quad (2.31)$$

$$\mu_i \ddot{\psi}_i = -\frac{\partial E^{\text{KS}}[\{R_I\}, \{\psi_i\}]}{\partial \psi_i^*} + \frac{\partial}{\partial \psi_i^*} \sum_{i,j=1}^n \lambda_{ij} (\langle \psi_i | \psi_j \rangle - \delta_{ij}) \quad (2.32)$$

In this notation, each dot on  $\dot{R}_I$  and  $\ddot{\psi}_i$  indicates a time derivative of the function. Here  $\mu$  is a fictitious mass assigned to the electrons. The value of  $\mu$  is chosen small enough to maintain adiabaticity; that is, to avoid significant energy transfer between nuclei and electrons.

According to the Car-Parrinello equations of motion, the nuclei evolve in time at a physical temperature proportional to their kinetic energy  $\sum_{I=1}^N \frac{1}{2} M_I \dot{R}_I^2$ . At the same time, to ensure that during time evolution they remain close to the Born-Oppenheimer surface, the electrons are maintained at a fictitious temperature which is low compared to the physical nuclear temperature, and proportional to their kinetic energy  $\sum_{i=1}^n \frac{1}{2} \mu_i \langle \dot{\psi}_i | \dot{\psi}_i \rangle$ . Therefore, if the electronic wavefunction has been optimized for an initial nuclear configuration, the electronic subsystem will remain close to its energy minimum along the MD trajectory.

In order for the electrons to remain at low temperature while following the motion of the nuclei along the dynamics, no energy transfer has to occur between the electronic and the nuclear subsystems. This adiabatic separation can be achieved if the lowest electronic frequency  $\omega_{\text{el}}^{\text{min}}$  is much higher than the highest nuclear frequency  $\omega_{\text{nuc}}^{\text{max}}$ ; that is, if there is no substantial overlap in the frequency domain of the two subsystems.

The electronic frequency spectrum is inversely proportional to the square root of the fictitious mass  $\mu$ :  $\omega_{\text{el}}^{\text{min}} \propto (E_{\text{gap}}/\mu)^{1/2}$ , where  $E_{\text{gap}}$  is the electronic energy difference between the lowest unoccupied and the highest occupied orbital.

Since the  $E_{\text{gap}}$  and  $\omega_{\text{nuc}}^{\text{max}}$  values are inherently correlated to the properties of the system,  $\mu$  is the only parameter that can be decreased to increase  $\omega_{\text{el}}^{\text{min}}$ , and consequently the  $\omega_{\text{el}}^{\text{min}} - \omega_{\text{nuc}}^{\text{max}}$  separation. However, increasing  $\omega_{\text{el}}^{\text{min}}$  implies also decreasing the maximum time step applicable in a simulation since  $\Delta t^{\text{max}} \propto \mu^{1/2}$ . Therefore, the value of  $\mu$  has to be chosen in order to provide the largest possible time step, while conserving adiabaticity. A  $\mu$  value of 400 a.u. is used for all the CPMD simulations presented in this thesis.

#### **2.4.1. Periodic boundary conditions and plane wave basis set**

In MD the simulation box is repeated in space using periodic boundary conditions (PBC) to mimic macroscopic systems and minimize surface effects. PBC can also be



used when simulating an isolated molecule, provided that the dimension of the box is large enough to avoid spurious interactions between periodic images.

Within the context of chapter 4 of this thesis, PBC are used to simulate an infinite slab of  $\text{TiO}_2$  functionalized with a molecular chromophore. Due to the presence of the chromophore, the unit cell of the crystal cannot be taken as the simulation box. Instead, a supercell has to be used. Its dimension must be large enough to, on one side, avoid spurious interactions between the chromophore images, while also accurately describe the density of states of the  $\text{TiO}_2$  surface. In chapter 5, PBC are used to simulate a molecular complex in an explicit water environment.

PBC are used within the CPMD program, allowing the expansion of the orbitals as linear combinations of plane wave (PW) basis functions:

$$\psi_i(\mathbf{r}) = \frac{1}{\sqrt{\Omega_{\text{SC}}}} \sum_{\mathbf{G}}^{G_{\text{max}}} c_i(\mathbf{G}) \exp[i\mathbf{G}\mathbf{r}]. \quad (2.33)$$

Here, the plane wave basis function

$$f_{\mathbf{G}}^{\text{PW}}(\mathbf{r}) = \frac{1}{\sqrt{\Omega_{\text{SC}}}} \exp[i\mathbf{G}\mathbf{r}] \quad (2.34)$$

is expressed in terms of the reciprocal lattice vectors  $\mathbf{G}$ .  $\Omega_{\text{SC}}$ , which is included in the normalization factor  $1/\sqrt{\Omega_{\text{SC}}}$ , represents the volume of the supercell. It has to be noted that equation 2.34 does not show any dependency on the nuclear positions  $\{\mathbf{R}_I\}$ , since the plane waves are originless functions delocalized over the entire space. This allows to control the accuracy of the calculations with an energy cutoff,  $E_{\text{cut}} = \frac{1}{2}G_{\text{max}}^2$  (in a.u.), which determines the number of plane waves used. Increasing this parameter, increases the largest reciprocal lattice vector included in the finite expansion of equation 2.33.

Fast Fourier transform algorithms can be used to move from the real to the reciprocal space, and vice versa. Consequently, the different terms in the energy functional can be more easily evaluated in one or the other space, depending on the efficiency of the calculation.

Additionally, since the PW functions are originless, the Pulay forces are zero, which greatly facilitates the calculation of nuclear forces.

A disadvantage of using PW functions is that to describe the electrons at a decreasingly small distance from the nucleus, requires a large increase in the PW basis set, making therefore their use unpractical. To solve this problem, a distinction

between core and valence electrons is made when using PW functions. It is assumed that the core electrons are practically inert. This allows to take the core electrons out of the explicit calculation, by replacing them with smooth and nodeless potentials called pseudopotentials<sup>25-28</sup>.

### **2.5. TIME-DEPENDENT DENSITY FUNCTIONAL THEORY (TD-DFT)**

Crucial for the study of photochemical processes is the description of the excited electronic states. In 1984 Runge and Gross generalized the density functional formalism for time-dependent systems<sup>29</sup>, thus paving the way for efficient calculations of excited state properties for large molecular systems.

The Runge-Gross theorem considers an arbitrary system which evolves under the influence of a time dependent external potential  $v(\mathbf{r}, t)$ . As in the first HK theorem, they proved that a bijective map exists between the time-dependent external potential  $v(\mathbf{r}, t)$  and the time-dependent electron density  $\rho(\mathbf{r}, t)$ , as well as the time-dependent total wavefunction:  $v(\mathbf{r}, t) \leftrightarrow \Psi(t) \leftrightarrow \rho(\mathbf{r}, t)$ .

It follows that every observable of the system is a unique functional of the density at time  $t$ :

$$O[\rho_t](t) = \langle \Psi[\rho](t) | \hat{O}(t) | \Psi[\rho](t) \rangle \quad (2.35)$$

Again, the time-dependent density of the interacting system  $\rho(\mathbf{r}, t)$  can be calculated as the density of a non-interacting system  $\rho_s(\mathbf{r}, t)$  under the influence of the local potential  $v_s(\mathbf{r}, t)$

$$\rho(\mathbf{r}, t) = \rho_s(\mathbf{r}, t) = \sum_{i=1}^n |\phi_i(\mathbf{r}, t)|^2 \quad (2.36)$$

where  $\phi_i(\mathbf{r}, t)$  are the non-interacting single particle KS orbitals obtained by solving the time-dependent Kohn-Sham equations of the non-interacting system

$$i \frac{\partial}{\partial t} \phi_i(\mathbf{r}, t) = \left( -\frac{\nabla^2}{2} + v_s[\rho](\mathbf{r}, t) \right) \phi_i(\mathbf{r}, t) \quad (2.37)$$

The time-dependent single particle KS potential is again written as

$$v_s[\rho](\mathbf{r}, t) = v_{\text{ext}}(\mathbf{r}, t) + \int_{\Omega_{\text{TOT}}} \frac{\rho(\mathbf{r}', t)}{|\mathbf{r} - \mathbf{r}'|} d\mathbf{r}' + v_{\text{xc}}[\rho](\mathbf{r}, t) \quad (2.38)$$

where the first and the second term on the right hand side of the equation are, respectively, the external time-dependent field and the Hartree potential, while  $v_{\text{xc}}[\rho](\mathbf{r}, t)$  is the exchange-correlation potential. The latter has to be approximated since its exact form is unknown.

TD-DFT describes the interaction of an arbitrary system, *e.g.* a molecule, with a time-dependent external field. If the effect of the external field on the system is sufficiently small in the sense that it does not disrupt completely the ground state system's structure, then the system response can be more efficiently described with a perturbative method, rather than explicitly solving iteratively the TDKS equations.

This is the case for the determination of properties like excitation energies and polarizabilities, which are obtained through the linear response of the ground state density while avoiding the explicit evaluation of the excited states.

### 2.5.1. Linear response TD-DFT

A time-dependent external potential  $v_{\text{ext}}(\mathbf{r}, t)$  acting on a system, such as an electromagnetic field, induces a time-dependent change in the electron density of the system.

We assume that the external potential acting on the system has the form

$$v_{\text{ext}}(\mathbf{r}, t) = \begin{cases} v_0(\mathbf{r}) & ; t \leq t_0 \\ v_0(\mathbf{r}) + v_1(\mathbf{r}, t) & ; t > t_0 \end{cases} \quad (2.39)$$

This means that at  $t \leq t_0$  the system is subject solely to the potential imposed by the nuclei  $v_0(\mathbf{r})$  in its ground state, and that its electron density is  $\rho_0(\mathbf{r})$ . At  $t > t_0$ , the perturbation  $v_1(\mathbf{r}, t)$  is switched on, leading to a total external potential  $v_{\text{ext}}(\mathbf{r}; t) = v_0(\mathbf{r}) + v_1(\mathbf{r}, t)$ . The variation in the total external potential will induce a variation in the electron density of the system.

Using perturbation theory, the effect of a variation in the external field  $v_1$  on any system's observable, and thus also on  $\rho(\mathbf{r}, t)$ , can be represented as a Taylor series

$$\rho(\mathbf{r}, t) = \rho_0(\mathbf{r}) + \rho_1(\mathbf{r}, t) . \quad (2.40)$$

In linear response only the first order term in the density perturbation  $\rho_1(\mathbf{r}, t)$  is

considered<sup>30</sup>. It can be defined as

$$\rho_1(\mathbf{r}, t) = \int_0^\infty dt' \int_{\Omega_{\text{TOT}}} \chi(\mathbf{r}t, \mathbf{r}'t') \delta v_1(\mathbf{r}', t) d\mathbf{r}' \quad (2.41)$$

where

$$\chi(\mathbf{r}t, \mathbf{r}'t') = \left. \frac{\delta \rho(\mathbf{r}, t)}{\delta v_1(\mathbf{r}', t')} \right|_{v_0} \quad (2.42)$$

takes the name of linear response function.

In TD-DFT, the density of a system of interacting electrons can be obtained from a KS system for which the electrons do not interact. Consequently, the linear electron density change  $\rho_1(\mathbf{r}, t)$  induced by the perturbation acting on the interacting system can be calculated as the response of the non-interacting KS system:

$$\rho_1(\mathbf{r}, t) = \int_0^\infty dt' \int_{\Omega_{\text{TOT}}} \chi_s(\mathbf{r}t, \mathbf{r}'t') v_{s,1}(\mathbf{r}', t') d\mathbf{r}' \quad (2.43)$$

Here  $\chi_s(\mathbf{r}t, \mathbf{r}'t')$  is the linear response function of the non-interacting system evaluated at the unperturbed density, while  $v_{s,1}(\mathbf{r}', t)$  is the effective time-dependent potential evaluated as the first order perturbation of the external potential acting on the KS system.

Moving to a non-interacting framework makes possible to write  $\chi_s$  in terms of the unperturbed stationary KS orbitals as

$$\chi_s(\mathbf{r}, \mathbf{r}'; \omega) = \lim_{\eta \rightarrow 0^+} \sum_{i,k=1}^K (f_k - f_i) \frac{\phi_i(\mathbf{r}) \phi_k^*(\mathbf{r}) \phi_i^*(\mathbf{r}') \phi_k(\mathbf{r}')}{\omega - (\varepsilon_i - \varepsilon_k) + i\eta} \quad (2.44)$$

where  $f_i$  is the occupation number of the ground-state KS orbital  $\phi_i$ ,  $\varepsilon_i$  its energy,  $\eta$  is a positive infinitesimal, and  $\omega$  is the frequency of the external perturbation field. The summation of equation 2.44 runs over all the  $K$  occupied and unoccupied orbitals of the system. It has to be noted that for convenience, in equation 2.44 the KS density response function has been written in the Lehmann representation by

Fourier transformation into the frequency domain.

To solve equation 2.43, an expression for the first order variation of the time-dependent KS potential has to be given.

The exchange-correlation kernel is defined as the functional derivative of the xc-potential with respect to the ground state density  $\rho_0$ . It is defined as:

$$f_{xc}[\rho_0](\mathbf{r}t, \mathbf{r}'t') = \left. \frac{\delta v_{xc}[\rho](\mathbf{r}, t)}{\delta \rho(\mathbf{r}', t')} \right|_{\rho=\rho_0} \quad (2.45)$$

Therefore, for any given  $v_1$  it is possible to write the expression for the time-dependent KS potential as

$$v_s(\mathbf{r}, t) = v_1(\mathbf{r}, t) + \int_{\Omega_{TOT}} \frac{\rho_1(\mathbf{r}', t)}{|\mathbf{r} - \mathbf{r}'|} d\mathbf{r}' + \int_{t_0}^t dt' \int_{\Omega_{TOT}} d\mathbf{r}' f_{xc}[\rho_0](\mathbf{r}t, \mathbf{r}'t') \rho_1(\mathbf{r}', t'). \quad (2.46)$$

Again, the exact form of equation 2.45 is unknown and has to be approximated. The simplest approximation for this kernel is the Adiabatic LDA (ALDA). The term adiabatic derives from the assumption that the electron density of the system readjusts instantaneously to a variation in the external field, thus reducing the kernel dependency only to local density and time:  $f_{xc}[\rho_0](\mathbf{r}, t)$ .

By applying equation 2.46 and 2.44 into equation 2.43, it is obtained an exact representation of the linear response of the interacting system density to the effective time-dependent perturbation.

TD-DFT has proven to provide accurate excitation energies as long as low-energy transitions involving valence states are investigated.

TD-DFT has become a standard tool for the characterization of molecular systems, particularly if designed for optical applications.

With the development of more and more sophisticated exchange-correlation functionals that can account for long-range correction (see section 2.3), TD-DFT is assuming an ever growing role in studying photoinduced charge transfer processes.

## 2.6. CONSTRAINED DENSITY FUNCTIONAL THEORY

The process of electron transfer (ET) from a donor (D) to and acceptor (A) state is a nonadiabatic process whose description has been proven computationally challenging<sup>31,32</sup>.

In this context, given a donor-acceptor (D-A) system, the objective is to calculate the rate of electron transfer between them (*i.e.*  $D - A \xrightarrow{k_{ET}} D^+ - A^-$ ).

In 1956, R.A. Marcus proposed a theory<sup>33</sup> (see section 1.4 of this thesis) to estimate the rate of such a process through the expression

$$k_{ET} = \frac{2\pi}{\hbar} \langle |H_{ab}|^2 \rangle (4\pi k_B T \lambda)^{-1/2} \exp \left[ \frac{(\Delta G^0 + \lambda)^2}{4\lambda k_B T} \right], \quad (2.47)$$

where  $H_{ab}$  is the coupling between the donor and the acceptor states ( $\psi_d$  and  $\psi_a$ , respectively),  $\Delta G^0$  is the driving force of the process, and  $\lambda$  is the reorganization free energy. Among these three parameters, essential for  $k_{ET}$  calculations,  $H_{ab}$  is the one proven more challenging to accurately estimate since it requires the use of expensive wavefunction based *ab initio* methods<sup>34</sup>. In principle, DFT-based methods could also be used as less computationally intensive alternatives for such tasks. However, their results are often biased by the electron delocalization error of commonly used exchange-correlation approximations<sup>35,36</sup>.

Inspired by previous works<sup>37-39</sup> on DFT-based methods in which the energy is minimized under certain density constraints, Van Voorhis and collaborators have recently proposed a new approach for calculating  $H_{ab}$ ,  $\Delta G^0$  and  $\lambda$  from charge-localized diabatic states. Due to their localized nature, the use of these states strongly reduces the electron delocalization error previously mentioned.

Constrained DFT (CDFT) methods allow the construction of the two diabatic states  $D - A$  and  $D^+ - A^-$  and thus the computation of the parameters in equation 2.47. This is done by minimizing the KS energy functional  $E^{KS}[\rho]$  under the constraint that the charge difference between D and A is equal to a certain value  $N_c$ . The purpose is to find that particular external potential associated to a ground-state corresponding to the constrained state<sup>40</sup>.

The minimization is carried out by using a Lagrange multiplier as

$$W[\rho, V_c] = E^{KS}[\rho] + V_c \left( \int_{\Omega_{tot}} w(\mathbf{r}) \rho(\mathbf{r}) d\mathbf{r} - N_c \right), \quad (2.48)$$

where  $W[\rho, V_c]$  is the energy functional for the constrained state,  $E^{KS}[\rho]$  is the KS energy functional and  $V_c$  is the Lagrange multiplier used to enforce the constraint

$$\int_{\Omega_{\text{tot}}} w(\mathbf{r})\rho(\mathbf{r})d\mathbf{r} = N_c. \quad (2.49)$$

Here,  $w(\mathbf{r})$  is the weight function that defines the partition of the electron density between donor and acceptor.

Making equation 2.48 stationary for normalized orbitals yields

$$\left[ -\frac{\nabla^2}{2} + v_{\text{ext}}(\mathbf{r}) + \int_{\Omega_{\text{tot}}} \frac{\rho(\mathbf{r}')}{|\mathbf{r} - \mathbf{r}'|} d\mathbf{r}' + v_{\text{xc}}(\mathbf{r}) + V_c w_c(\mathbf{r}) \right] \psi_i(\mathbf{r}) = \varepsilon_i \psi_i(\mathbf{r}), \quad (2.50)$$

which is the same as equation 2.23, except for the last term in the effective Hamiltonian, which represents the constraint potential.

For every  $V_c$  then exists a unique set of orbitals  $\{\psi_i\}$  that can be used to calculate the system's electron density associated with that specific constraint potential. This implies that  $W$  is itself a function of  $V_c$ . It can be shown<sup>40</sup> that  $W(V_c)$  is a concave function, which has only one stationary point of maximum. Therefore, it can be optimized with respect to  $V_c$ , to find the potential value that produces the constrained ground state density.

The optimization procedure involves a double loop which proceeds as follows: i) an initial set of orbitals is used to construct the KS Hamiltonian; ii) an initial value is assigned to the constraint potential to build the total effective Hamiltonian and solve equation 2.50; iii) the first and second derivative of  $W$  with respect to  $V_c$  are calculated to optimize the potential. Since to every new potential corresponds a new electron density, the process is restarted from point (i) and is iterated until it converges self consistently. Self-consistency is considered reached when the total deviation of the constraint with respect to  $N_c$  is lower than  $10^{-5}$ .

Once  $V_c$  is found for both diabatic states, then the calculation of  $\Delta G$ ,  $\lambda$  and  $H_{ab}$  can be done assuming the validity of Marcus theory. A detailed mathematical description of the procedures leading to these parameters can be found in the literature<sup>34,40,41</sup>.

## 2.7. SEMI-EMPIRICAL METHODS: Hückel and Extended Hückel Method

One of the first semi-empirical methods to be proposed was the Hückel Molecular Orbital (MO) theory in 1930. Introduced by Erich Hückel, this method is intended for studying planar conjugated hydrocarbon systems.

In the Hückel MO method one of the central assumptions is that the general properties of a conjugated hydrocarbon molecule are determined by its  $\pi$ -electron MOs. This allows to disregard all the  $\sigma$ -electrons in a molecule, and simply treat  $\sigma$ -bonds as the backbone on which  $\pi$ -electrons delocalize. This approximation is made possible by the planarity of a conjugated molecule. In a planar molecule, in fact,  $\sigma$  and  $\pi$  molecular orbitals are respectively symmetric and anti-symmetric with respect to reflection in the molecular plane. Consequently, the  $\sigma$  and  $\pi$  orbitals are orthogonal and can be treated independently from each other. Despite its simplicity, this method is able to predict the effects of delocalization on orbital stability and identify whether a specific structure will or will not be aromatic. However, due to the strong approximations introduced, its applicability is limited solely to planar systems.

To overcome the limitations presented by the Hückel MO theory, in 1963<sup>42</sup> Roald Hoffmann developed the Extended Hückel theory (EHT). Differently from Hückel MO theory, in the EHT method not only the  $\pi$  but all the valence electrons are considered. This enlargement of basis set allows the determination of molecular energies and structures, transition states and energy barriers.

In the EHT formalism, the total electronic wavefunction for a system with  $n$  valence electrons is described as a product of one-electron wavefunctions  $\psi_j(\mathbf{r}_j)$

$$\Psi_{\text{EHT}} = \psi_1(\mathbf{r}_1)\psi_2(\mathbf{r}_2)\dots\psi_j(\mathbf{r}_j)\dots\psi_n(\mathbf{r}_n). \quad (2.51)$$

In turn, these one-electron molecular orbitals can be written as linear combinations of normalized valence atomic orbitals  $\varphi_\nu$

$$\psi_j = \sum_{\nu=1}^K c_{\nu j} \varphi_\nu \quad (2.52)$$

In the EHT, the basis set is formed by Slater-type orbitals (STOs) chosen to represent the valence orbitals of the atoms in the molecule. Once the molecular orbitals are constructed, it is possible to calculate the total energy of the system as the sum of the one-electron energies  $\varepsilon_j$ , which can be evaluated by applying the effective one-electron Hamiltonian  $\hat{h}_{eff}$  to the one-electron molecular orbital  $\psi_j$



$$\hat{h}_{eff}\psi_j = \varepsilon_j\psi_j \quad (2.53)$$

The  $\hat{h}_{eff}$  describes the interaction of an electron with the rest of the molecule. However, the exact expression of this Hamiltonian is not needed in EHT.

The crucial step in obtaining the eigenfunctions for an effective Hamiltonian is the construction of the secular determinant

$$\begin{vmatrix} H_{11} - ES_{11} & H_{12} - ES_{12} & \cdots & H_{1K} - ES_{1K} \\ H_{21} - ES_{21} & H_{22} - ES_{22} & \cdots & H_{2K} - ES_{2K} \\ \vdots & \vdots & \ddots & \vdots \\ H_{K1} - ES_{K1} & H_{K2} - ES_{K2} & \cdots & H_{KK} - ES_{KK} \end{vmatrix} = 0 \quad (2.54)$$

To solve this equation it is necessary to calculate a series of overlap ( $S_{\mu\nu}$ ) and resonance integrals ( $H_{\nu\mu}$ ). The solution to the first problem is rather simple. Since we know the form and the position of the atomic orbitals, their overlap can be readily evaluated as a function of interatomic distances. The diagonal resonance integral  $H_{\mu\mu}$  is called Coulomb integral and represents the kinetic and potential energy of an electron in a specific atomic orbital  $\varphi_\mu$ . Its value is parametrized against a specific reference value, which is usually taken as the negative of the orbital ionization potential. On the contrary, the off diagonal resonance integral  $H_{\mu\nu}$  describes the energy of an electron in the region where the orbitals  $\varphi_\mu$  and  $\varphi_\nu$  overlap. This term can be approximated as

$$H_{\mu\nu} = \frac{1}{2} k_{\mu\nu} (H_{\mu\mu} + H_{\nu\nu}) S_{\mu\nu} \quad (2.55)$$

Equation 2.55 indicates that  $H_{\mu\nu}$  is proportional to the energy of the atomic orbitals involved, and to the extent of their overlap. The term  $k_{\mu\nu}$  is an empirical factor usually assumed equal to 1.75, which takes the name of Wolfsberg-Helmholtz constant.

Through the application of these conventions it is possible to solve the secular equation and obtain qualitatively correct energy values and wavefunctions for the molecular orbitals of the investigated system. However, since EHT is not a self-consistent method, it is not able to generate potential energy surfaces accurately. Therefore, it is best applied in combination with structures or trajectories obtained

from higher levels of theory. This is the strategy adopted in chapter 4 and 5 of this thesis.

## 2.8. REFERENCES

- (1) Born, M.; Oppenheimer, R. Zur Quantentheorie Der Molekeln. *Ann. Phys.* **1927**, *389* (20), 457–484.
- (2) Handy, N. C.; Yamaguchi, Y.; Iii, H. F. S. The Diagonal Correction to the Born–Oppenheimer Approximation: Its Effect on the Singlet–triplet Splitting of CH<sub>2</sub> and Other Molecular Effects. *J. Chem. Phys.* **1986**, *84* (8), 4481–4484.
- (3) Ehrenfest, P. Bemerkung Über Die Angenäherte Gültigkeit Der Klassischen Mechanik Innerhalb Der Quantenmechanik. *Z. Für Phys.* **1927**, *45*, 455–457.
- (4) Fischer, S. A.; Chapman, C. T.; Li, X. Surface Hopping with Ehrenfest Excited Potential. *J. Chem. Phys.* **2011**, *135* (14), 144102.
- (5) Tully, J. C.; Preston, R. K. Trajectory Surface Hopping Approach to Nonadiabatic Molecular Collisions: The Reaction of H<sup>+</sup> with D<sub>2</sub>. *J. Chem. Phys.* **1971**, *55* (2), 562–572.
- (6) Hohenberg, P.; Kohn, W. Inhomogeneous Electron Gas. *Phys. Rev.* **1964**, *136* (3B), B864–B871.
- (7) Kohn, W.; Sham, L. J. Self-Consistent Equations Including Exchange and Correlation Effects. *Phys. Rev.* **1965**, *140* (4A), A1133–A1138.
- (8) Ceperley, D. M.; Alder, B. J. Ground State of the Electron Gas by a Stochastic Method. *Phys. Rev. Lett.* **1980**, *45* (7), 566–569.
- (9) Vosko, S. H.; Wilk, L.; Nusair, M. Accurate Spin-Dependent Electron Liquid Correlation Energies for Local Spin Density Calculations: A Critical Analysis. *Can. J. Phys.* **1980**, *58* (8), 1200–1211.
- (10) Perdew, J. P.; Wang, Y. Accurate and Simple Analytic Representation of the Electron-Gas Correlation Energy. *Phys. Rev. B* **1992**, *45* (23), 13244–13249.
- (11) Perdew, J. P.; Zunger, A. Self-Interaction Correction to Density-Functional Approximations for Many-Electron Systems. *Phys. Rev. B* **1981**, *23* (10), 5048–5079.
- (12) Cole, L. A.; Perdew, J. P. Calculated Electron Affinities of the Elements. *Phys. Rev. A* **1982**, *25* (3), 1265–1271.
- (13) Becke, A. D. Density-Functional Exchange-Energy Approximation with Correct Asymptotic Behavior. *Phys. Rev. A* **1988**, *38* (6), 3098–3100.
- (14) Becke, A. D. Density-functional Thermochemistry. III. The Role of Exact Exchange. *J. Chem. Phys.* **1993**, *98* (7), 5648–5652.
- (15) Perdew, J. P. Density-Functional Approximation for the Correlation Energy of the Inhomogeneous Electron Gas. *Phys. Rev. B Condens. Matter* **1986**, *33* (12), 8822–8824.
- (16) Perdew, J. P.; Burke, K.; Ernzerhof, M. Generalized Gradient Approximation Made Simple. *Phys. Rev. Lett.* **1996**, *77* (18), 3865–3868.
- (17) Lee, C.; Yang, W.; Parr, R. G. Development of the Colle-Salvetti Correlation-Energy Formula into a Functional of the Electron Density. *Phys. Rev. B* **1988**, *37* (2), 785–789.
- (18) Slater, J. C. A Simplification of the Hartree-Fock Method. *Phys. Rev.* **1951**, *81* (3), 385–390.
- (19) Yanai, T.; Tew, D. P.; Handy, N. C. A New Hybrid Exchange–correlation Functional Using the Coulomb-Attenuating Method (CAM-B3LYP). *Chem. Phys. Lett.* **2004**, *393* (1–3), 51–57.
- (20) Rohrdanz, M. A.; Martins, K. M.; Herbert, J. M. A Long-Range-Corrected Density Functional That Performs Well for Both Ground-State Properties and Time-Dependent Density Functional Theory Excitation Energies, Including Charge-Transfer Excited States. *J. Chem. Phys.* **2009**, *130* (5), 054112.
- (21) Tawada, Y.; Tsuneda, T.; Yanagisawa, S.; Yanai, T.; Hirao, K. A Long-Range-Corrected Time-Dependent Density Functional Theory. *J. Chem. Phys.* **2004**, *120* (18), 8425–8433.

- (22) Kobayashi, R.; Amos, R. D. The Application of CAM-B3LYP to the Charge-Transfer Band Problem of the Zincbacteriochlorin-bacteriochlorin Complex. *Chem. Phys. Lett.* **2006**, *420* (1–3), 106–109.
- (23) Car, R.; Parrinello, M. Unified Approach for Molecular Dynamics and Density-Functional Theory. *Phys. Rev. Lett.* **1985**, *55* (22), 2471–2474.
- (24) Sprik, M.; Ciccotti, G. Free Energy from Constrained Molecular Dynamics. *J. Chem. Phys.* **1998**, *109* (18), 7737–7744.
- (25) Phillips, J. C. Energy-Band Interpolation Scheme Based on a Pseudopotential. *Phys. Rev.* **1958**, *112* (3), 685–695.
- (26) Phillips, J. C.; Kleinman, L. New Method for Calculating Wave Functions in Crystals and Molecules. *Phys. Rev.* **1959**, *116* (2), 287–294.
- (27) Hellmann, H. A New Approximation Method in the Problem of Many Electrons. *J. Chem. Phys.* **1935**, *3* (1), 61–61.
- (28) Hellmann, H.; Kassatotschkin, W. Metallic Binding According to the Combined Approximation Procedure. *J. Chem. Phys.* **1936**, *4* (5), 324–325.
- (29) Runge, E.; Gross, E. K. U. Density-Functional Theory for Time-Dependent Systems. *Phys. Rev. Lett.* **1984**, *52* (12), 997–1000.
- (30) Gross, E. K.; Maitra, N. T. Introduction to TDDFT. In *Fundamentals of Time-Dependent Density Functional Theory*; Springer, 2012; pp 53–99.
- (31) Duncan, W. R.; Prezhdo, O. V. Theoretical Studies of Photoinduced Electron Transfer in Dye-Sensitized TiO<sub>2</sub>. *Annu. Rev. Phys. Chem.* **2007**, *58*, 143–184.
- (32) Eshuis, H.; Voorhis, T. van. The Influence of Initial Conditions on Charge Transfer Dynamics. *Phys. Chem. Chem. Phys.* **2009**, *11* (44), 10293–10298.
- (33) Marcus, R. A. On the Theory of Oxidation-Reduction Reactions Involving Electron Transfer. I. *J. Chem. Phys.* **1956**, *24* (5), 966–978.
- (34) Oberhofer, H.; Blumberger, J. Electronic Coupling Matrix Elements from Charge Constrained Density Functional Theory Calculations Using a Plane Wave Basis Set. *J. Chem. Phys.* **2010**, *133* (24), 244105–244105 – 10.
- (35) Cohen, A. J.; Mori-Sánchez, P.; Yang, W. Insights into Current Limitations of Density Functional Theory. *Science* **2008**, *321* (5890), 792–794.
- (36) Zhang, Y.; Yang, W. A Challenge for Density Functionals: Self-Interaction Error Increases for Systems with a Noninteger Number of Electrons. *J. Chem. Phys.* **1998**, *109* (7), 2604–2608.
- (37) Akai, H.; Blügel, S.; Zeller, R.; Dederichs, P. H. Isomer Shifts and Their Relation to Charge Transfer in Dilute Fe Alloys. *Phys. Rev. Lett.* **1986**, *56* (22), 2407–2410.
- (38) Dederichs, P. H.; Blügel, S.; Zeller, R.; Akai, H. Ground States of Constrained Systems: Application to Cerium Impurities. *Phys. Rev. Lett.* **1984**, *53* (26), 2512–2515.
- (39) Prezhdo, O. V.; Kindt, J. T.; Tully, J. C. Perturbed Ground State Method for Electron Transfer. *J. Chem. Phys.* **1999**, *111* (17), 7818–7827.
- (40) Wu, Q.; Van Voorhis, T. Direct Optimization Method to Study Constrained Systems within Density-Functional Theory. *Phys. Rev. A* **2005**, *72* (2), 024502.
- (41) Wu, Q.; Voorhis, T. V. Extracting Electron Transfer Coupling Elements from Constrained Density Functional Theory. *J. Chem. Phys.* **2006**, *125* (16), 164105.
- (42) Hoffmann, R. An Extended Hückel Theory. I. Hydrocarbons. *J. Chem. Phys.* **1963**, *39* (6), 1397–1412.



# Engineering a Donor-Antenna-Acceptor Triad for Photoinduced Charge Separation

### **3.0.ABSTRACT**

---

*In this chapter a series of donor-antenna-acceptor molecular rectifiers designed as modules for solar energy conversion devices are investigated via Density Functional Theory. We consider triad modules containing phenothiazine (PTZ) as electron donor and different derivatives of naphthalene diimide (NDI) as antenna and secondary electron acceptor. The choice of the molecular components in the triad is guided by the redox and optical properties of each subunit. Using time-dependent DFT in combination with the long-range corrected xc-functional CAM-B3LYP we investigate how photoinduced charge transfer states are affected by systematic modifications of the triad molecular structure. In particular, we show how by controlling the length of the molecular bridges connecting the different charge separator subunits it is possible to control the driving force for the evolution of the excitonic reactant state into the charge separated product state. Based on these findings we propose a supramolecular triad consisting of inexpensive and readily available molecular components that can find its implementation in artificial devices for solar energy transduction.*

---

**This chapter is based on the publication:**

Monti, A.; de Groot, H.J.M.; Buda, F. In-Silico Design of a Donor–Antenna–Acceptor Supramolecular Complex for Photoinduced Charge Separation. *J. Phys. Chem. C* **2014**, *118*, 15600-15609.

### **3.1. INTRODUCTION**

Progress in the design and synthesis of nanodevices for photovoltaics and artificial photosynthesis can be strongly supported by computational modeling methods able to predict optimal target properties for light energy conversion in the computer prior to the realization in chemical laboratories<sup>1,2,3,4,5</sup>.

In the past decades, the efficiency of photovoltaic and photochemical systems has been significantly improved. A clear example is represented by the power conversion efficiency of dye-sensitized solar cells, which has been increasing from the 7% of the first cell proposed by O' Regan and Grätzel, to the current value of 20% of perovskite based systems<sup>6,7</sup>. Despite these results, optimization of these devices for solar energy conversion is far from being achieved.

As explain in chapter 1, these systems are often composed of a molecular or solid-state chromophore coupled to a wide band-gap semiconductor. The chromophore photoabsorption induces the formation of an exciton reactant state. This is then dissociated as the excited electron is injected into the semiconductor conduction band, to form the charge separated product state. The collected electron can then be used to perform work or generating solar fuel. The positive hole left on the oxidized chromophore is quenched by means of a sacrificial reducing agent, or through water oxidation catalysis. The solar energy stored by photoexciting the chromophore may be lost if the system recombines to its ground state before the product state can be stabilized by driving the hole and the electron apart.

This undesired process, which can severely hamper the energy conversion efficiency of a devices, takes the name of charge recombination or back electron transfer. Recombination to the ground state can occur directly from the excitonic state or, if an electron is trapped at the semiconductor surface, even after the electron injection has occurred.

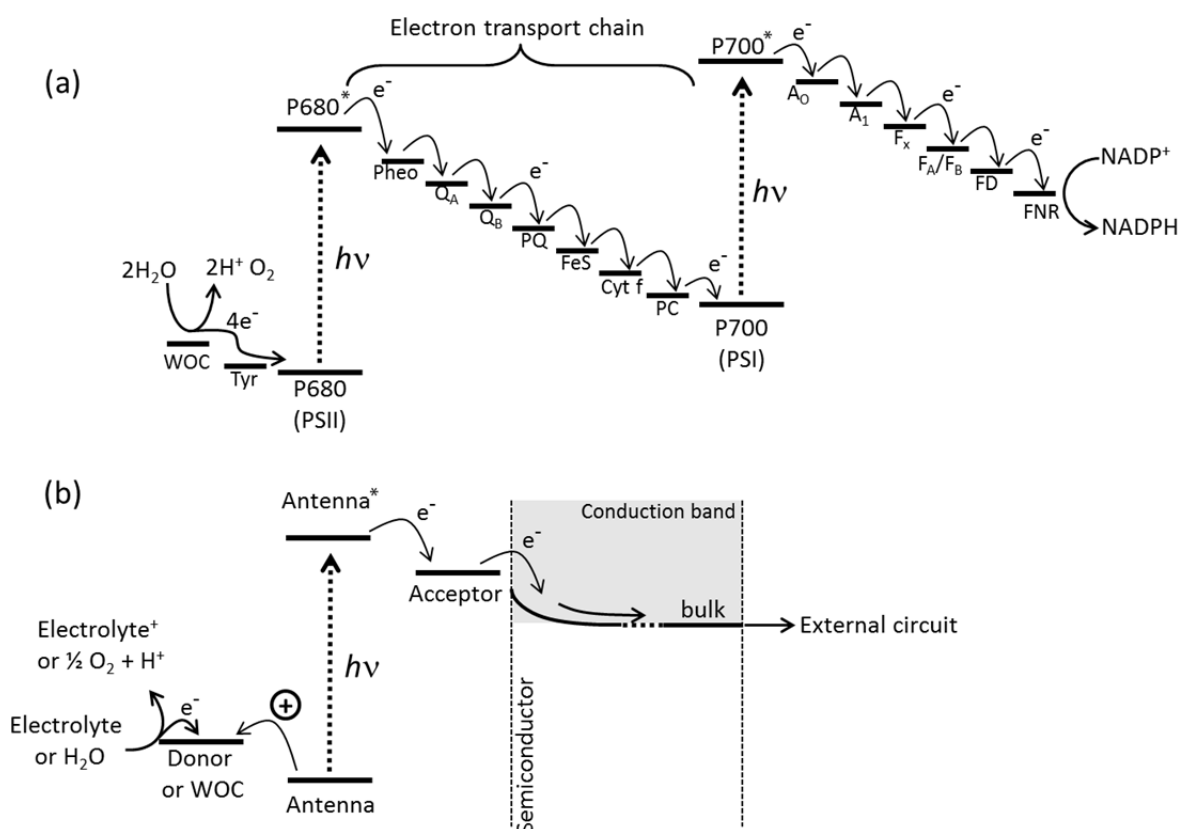
In natural systems, back electron transfer is prevented by quickly spatially separating the electron and the hole generated upon photoexcitation. This is achieved through a series of redox reactions between consecutive compounds with increasingly lower redox-potentials. It is observed that the charge recombination rate decays exponentially with the distance between the electron donor and acceptor units<sup>8,9</sup>.

Through the electron transport chain depicted in **Scheme 3.1a**, the excited electron is transferred from the electron donor pigment P680\* in PSII to the pigment P700 in PSI. The P680<sup>+</sup> is then reduced by a tyrosine residue (Tyr) in PSII, which is later reduced by the water oxidation catalyst.

In PSI, the photoexcitation of P700 initiates a secondary electron transfer cascade culminating in NADPH production (see **Scheme 3.1a**).

The transfer of the photoexcited electron from P680\* to the quinone  $Q_A$  occurs on a sub-nanosecond time scale preventing the slower exciton recombination to the ground state. Additionally, once the excited electron reaches  $Q_A$ , its distance from P680\* becomes too large to allow the recombination of the charges.

The number of subunits employed by the natural photosynthetic system to achieve the electron/hole charge separation, is however too large to be efficiently reproduced in an artificial device. A different design strategy is needed that requires a smaller number of subunits while still avoiding charge recombination events.



**Scheme 3.1.** (a) Schematic energy diagram of the natural photosynthesis mechanisms driven by the photoabsorption of the chromophore pigments P680 and P700, leading to electron flowing between the water oxidation catalyst (WOC) and the ferredoxin- $NADP^+$  reductase (FNR). This representation, readapted from references <sup>10,11</sup>, takes the name of Z-scheme. (b) Schematic energy diagram of a donor-antenna-acceptor triad applied as photosensitizer at the anode of a photovoltaic or photochemical cell.

Recent publications suggest that the recurrence of charge recombination in photochemical and photovoltaic devices can be reduced through systems composed of three or more subunits arranged in a Donor-Antenna-Acceptor (D-An-A) like design, presenting an optimized energy gradient and electronic coupling<sup>12,13,14,15</sup>. In this type of structures, upon photoexcitation of the antenna module, the charge



separation is achieved by transferring the electron and the hole in opposite directions. As shown in **Scheme 3.1b**, upon its formation, the exciton localized on the antenna is dissociated through two charge transfer processes: (i) transfer of the excited electron from the chromophore to the acceptor; (ii) reduction of the antenna through hole transfer onto the donor water oxidation catalyst (WOC), which becomes the oxidized species. The presence of the antenna complex between the donor and the acceptor should induce a considerable tunneling barrier for charge recombination and consequently reduce the electronic coupling between the charge separated and ground states of the triad. Like in the natural system, this will result in delaying the electronic recombination to the state of minimal energy and increase the lifetime of the charge separation for a time sufficient for redox reactions to occur at the donor and acceptor sites. In fact, within a photoanode for solar cell devices, these type of triads are bound directly to the surface of a suitable semiconductor through the acceptor unit. After formation of the charge separated state, electron injection can occur from the acceptor into the semiconductor, while the oxidized donor can be reduced to its neutral form by a sacrificial reductant, or through water oxidation (**Scheme 3.1b**). The regenerated triad can thus absorb another photon and reinitiate the cycle. If an electron is trapped at the semiconductor surface, it may quench the excitonic state induced by the second photon. The presence of the electron acceptor between the antenna and the semiconductor is meant to prevent this recombination by introducing a barrier for the back electron transfer.

In this chapter we show how Density Functional Theory (DFT) based methods can be used to optimize the optical and electronic properties of a molecular system designed for photovoltaics and photoelectrochemical applications prior to its experimental realization. The aim is to design a photosensitive triad-like charge separator which shows ultrafast unidirectional electron transfer leading to the formation of a charge separated state (CS) sufficiently stable to kinetically allow redox reactions at the donor (D) and the acceptor (A) moieties<sup>16</sup>. We choose the triad components on the basis of their ground and excited state redox potentials in order to obtain negative potential energy gradients between the donor-antenna and the antenna-acceptor subunits. Furthermore, the donor and the acceptor are chosen considering the potential boundaries necessary to couple the proposed triad within a device employing a silicon electrode and a commonly used electrolyte, such as iodide/triiodide.<sup>17</sup>

Through systematic changes in the linkage between the donor, the antenna and the acceptor, it is highlighted how structural modifications can be used to control the relative energies and electronic couplings between different excited states. In this way we are able to design a molecular triad for which the photoexcitation of the

antenna will trigger redox processes resulting into the formation of a final  $D^+ \text{-An-A}^-$  charge separated state. The molecular components used in this study as donor, antenna, and acceptor are respectively the 10,10a-dihydro-4aH-phenothiazine (PTZ), the 2,6-diethoxy-1,4,5,8-diimidenaphthalene ( $\text{NDI}_1$ ), and the 2,6-dicarbonitrile -1,4,5,8-diimidenaphthalene ( $\text{NDI}_2$ ). A schematic representation of the single components and of the different complexes analyzed is reported in **Figure 3.1**.

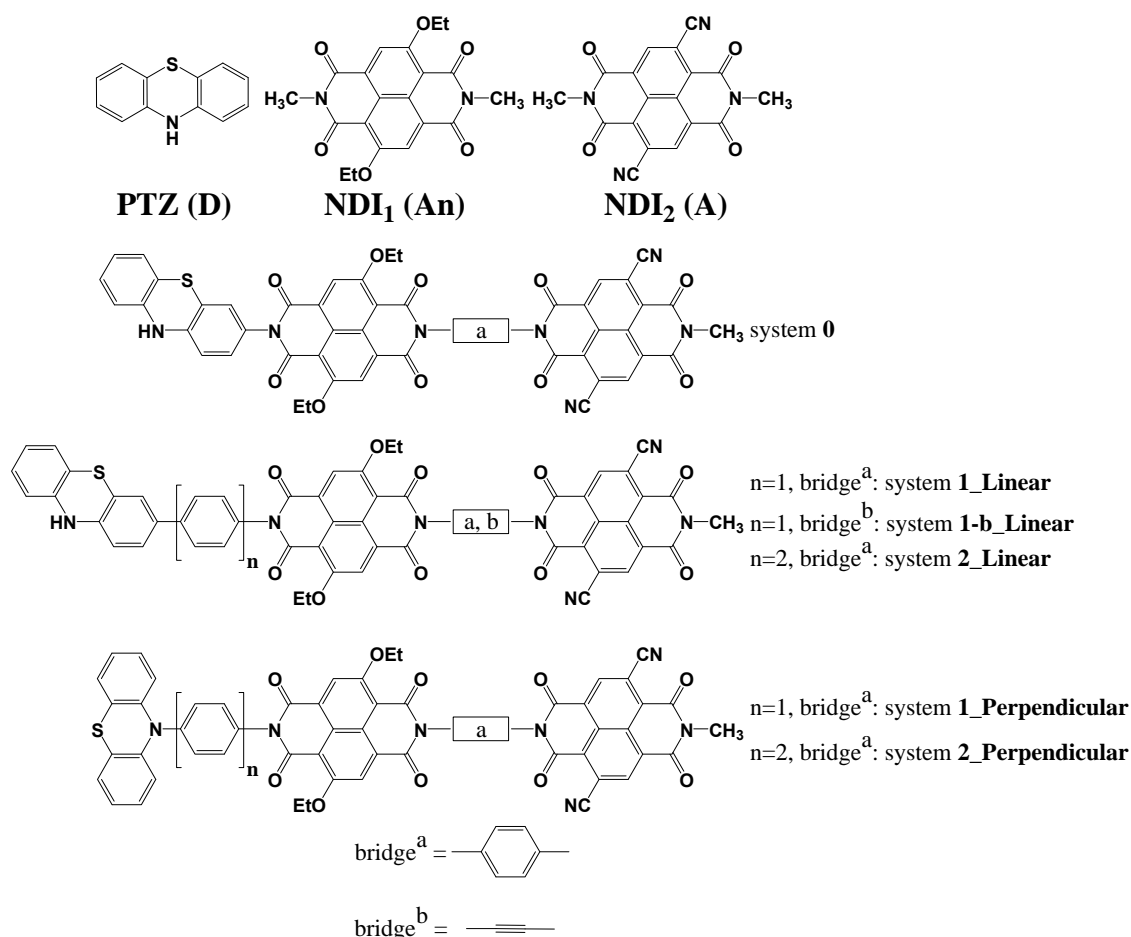


**Figure 3.1.** Molecular structures of the studied compounds. PTZ acts as electron donor (D),  $\text{NDI}_1$  as antenna (An) and  $\text{NDI}_2$  as electron acceptor (A). The number of phenyl units between D and An is indicated with  $n$ . Two different bridges (a and b) between An and A are considered. Linear and Perpendicular refer to the relative arrangements of PTZ and the phenyl bridge.

Individually, PTZ,  $\text{NDI}_1$  and  $\text{NDI}_2$  have already been discussed in the literature and are well known for their robustness and ease of synthesis. They have been chosen based on the perfect match between their well-characterized optical and electronic properties and the device requirements. The members of the naphthalene diimide family form an important class of chromophores which has been extensively analyzed in recent years and applied in a wide range of devices, such as

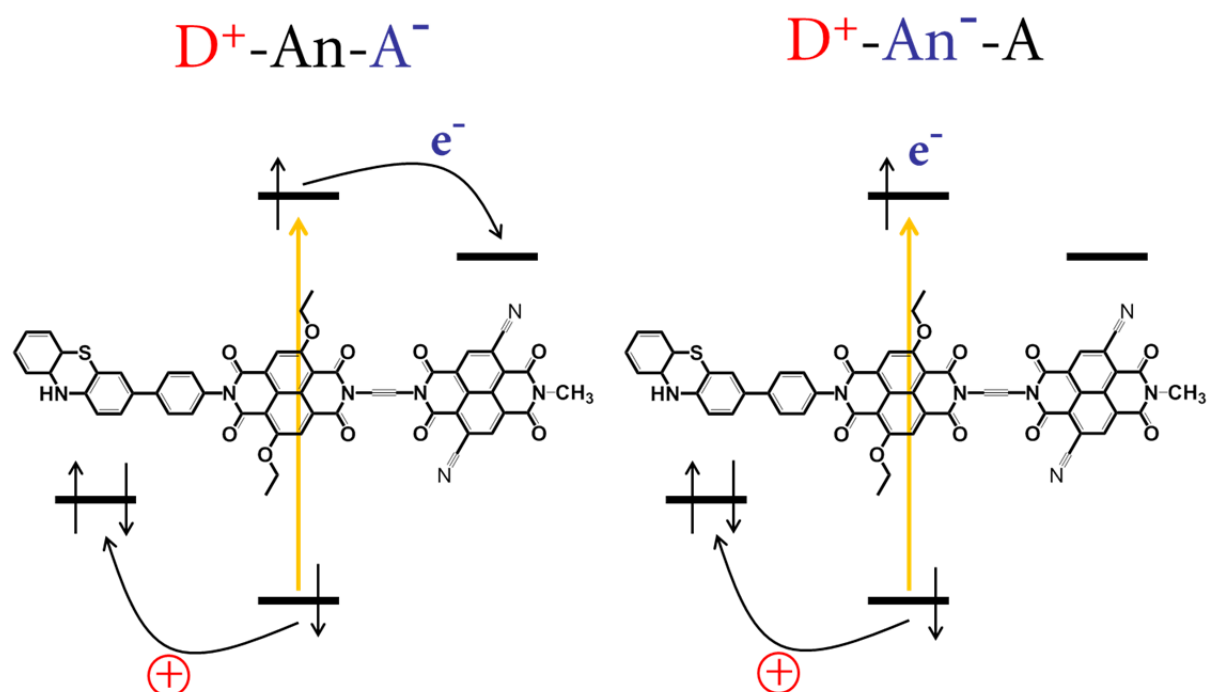
supramolecular switches, chemosensors, n-type semiconductor in organic transistors, light-harvesting chromophores in dye-sensitized solar cell (DSSC), and as electron acceptor in photoactivated artificial charge separators<sup>18-20,21,22</sup>. The versatility of these compounds is due to their peculiar electronic properties that can be easily tuned through a selective functionalization of the naphthalene core<sup>23</sup>. By choosing the appropriate functional groups it is possible to adjust the HOMOs and LUMOs orbital energies and their relative gaps. This allows to control the molecular absorption range and to adapt the molecular redox properties with respect to the environment requirements.

As shown by Sakai et al<sup>23</sup> due to their different functionalization NDI<sub>1</sub> and NDI<sub>2</sub> present absorptions in two different regions of the incoming photon spectrum. While the first is photoactive also into the visible, the second shows activity only in the UV-region. This ensures NDI<sub>1</sub> to be the only active chromophore for applications with visible light in solar energy conversion. On the other hand, NDI<sub>2</sub> is chosen not only for its absorption properties but also for its characteristic ability to form stable anionic radicals.<sup>24</sup> Especially in a context where several molecules are bound together through  $\pi$ - $\pi$  stacking, NDI<sub>2</sub> has been shown to behave as a n-type semiconductor material.<sup>25</sup> This characteristic makes it a very good candidate as electron acceptor able to increase the electron-hole distance through electron delocalization, thus decreasing the probability of its recombination into the ground state. Additionally, the LUMO energy of NDI<sub>2</sub> aligns well with the valence band of silicon, opening the possibility of establishing a p-n junction between the electron rectifier and a silicon-based electrode.

Finally, phenothiazine is a strong reducing agent photoactive only in the UV-region that is already widely employed as pesticide and in pharmaceutical or optical applications<sup>24,26,27</sup>. Thanks to the strong interaction between the 2p<sub>z</sub> electrons of the nitrogen atom of the central heterocyclic ring with the peripheral benzenes, PTZ can easily form cation-radical species and stabilize them through resonance delocalization of the positive charge into those electron-rich moieties<sup>26</sup>. PTZ is therefore an optimal electron donor able to quench the hole created into the antenna upon photoexcitation.

Herein we compare a series of molecular triads designed for photoinduced unidirectional charge separation. The Donor-Antenna distance proves to be a key parameter to control the relative energies of different excited states potential energy surfaces (PES). It is shown that it is possible to induce the concerted hole/electron transfer mechanism as dominant path for the formation of the charge separated state D<sup>+</sup>-An-A<sup>-</sup>, while avoiding the unwanted partially separated intermediate state D<sup>+</sup>-An<sup>-</sup>-A (see **scheme 3.2**). Geometrical and structural modifications are applied to

the bridge units to find an optimal balance between thermodynamics and electronic coupling requirements for a fast unidirectional charge transfer. The results lead to the design of the triad **1-b\_Linear** (Figure 3.1, third panel from top), for which ultrafast charge separation is predicted.



**Scheme 3.2.** Schematic energy diagram of the frontier molecular orbitals involved in the charge transfer processes leading to the formation of the charge separated ( $D^+ - An - A^-$ , left) and intermediate state ( $D^+ - An^- - A$ , right). The yellow arrow represents the photoexcitation of the antenna, while the curved arrows show the direction of the electron ( $e^-$ ) and hole ( $+$ ) transfer.

## 3.2. METHODS AND COMPUTATIONAL DETAILS

### 3.2.1. Ground State calculations

To optimize the ground state geometries of each monomer, dyad and triad presented in this work we make use of the ADF software package<sup>28-30</sup>. The geometries are optimized at the B3LYP<sup>53</sup>/TZP level of theory in a dichloromethane (DCM) environment described by the continuum solvent model COSMO<sup>31</sup>. Van der Waals dispersion interactions are included using the Grimme3-BJDAMP correction.<sup>32</sup>

### 3.2.2. Time-Dependent DFT

Time-Dependent DFT (TD-DFT) is used to calculate the absorption spectra of the investigated systems and to check how the optical properties of the singular components are affected by the assembling into the triad complexes. Several exchange-correlation functionals available in the ADF computational package have

been used to check the accuracy of our results against available experimental data (see results and discussion section 3.3.1).

### 3.2.3. Ground and excited state redox potentials

ADF is used for the calculation of the ground and excited state oxidation potentials of the donor, antenna and acceptor monomers. Following the procedure described by De Angelis et al<sup>33</sup>, the ground state oxidation potential is estimated as

$$G_{ox}^{GS} = G_{sol}^0 - G_{sol}^+ \quad (3.1)$$

Both  $G_{sol}^0$  and  $G_{sol}^+$  are obtained by adding the solvent effect to the energies of the molecules optimized in vacuum. The solvent contribution is estimated as the energy difference between the system in solution and in vacuum, calculated at the geometry optimized in solution.

The excited state oxidation potential  $G_{ox}^{ES}$  is obtained by subtracting from  $G_{ox}^{GS}$  the adiabatic lowest transition energy ( $E_{0-0}$ ):

$$G_{ox}^{ES} = G_{ox}^{GS} - E_{0-0} \quad (3.2)$$

where  $E_{0-0}$  is the energy difference between the excited and the ground states at their corresponding optimized geometries. Results were validated also by calculating the ground state oxidation potentials using the  $\Delta$ SCF and Born-Haber cycle methods<sup>34</sup>. All methods can reproduce the experimental redox values with an error <0.1 eV.

### 3.2.4. Excited state geometry optimizations

To investigate the possible electronic relaxations that can occur after photoabsorption, we optimize, for each charge separator, the (i) excitonic state, denoted throughout this chapter as S0, in which both hole and electron are localized on the antenna; (ii) the full charge separated state S1 in which the hole is on the donor and the electron on the acceptor; and (iii) the intermediate CS state S2 in which only the hole moves on the donor and the electron stays on the antenna. Other excited states have been investigated but they all turned out to be much higher in energy, indicating that their formation is strongly unlikely upon visible light absorption. For each complex, starting from their ground state optimized geometry, we initially induce a specific optical transition from the ground state to the diabatic state of interest and subsequently we optimize the geometry of such an excited state. In order to overcome the systematic underestimation of the excitation

energies associated with strong molecular charge transfer character shown by most xc-functional<sup>35</sup>, we make use of the long-range corrected functional CAM-B3LYP<sup>36</sup>, which has been shown to be quite accurate in describing electronic excitations with strong charge transfer character<sup>37,38</sup>. At the same time this functional is reasonably accurate in estimating the energy of excitation with strong excitonic character. These calculations are performed using the Gaussian 09 program package<sup>39</sup> using the cc-pVDZ basis set and the Polarizable Continuum Model to simulate the DCM solvation<sup>40</sup>.

### **3.2.5. Electronic coupling calculations**

To avoid confusion with the use of the terms donor and acceptor recurring in other sections, we need to specify that when describing hole-transfer processes, with the term donor we refer to the phenothiazine subunit, while with acceptor to the antenna NDI<sub>1</sub>. On the other hand, for the electron transfer calculations the terms donor and acceptor have to be intended as the subunits NDI<sub>1</sub> and NDI<sub>2</sub>, respectively.

The coupling strength between the orbitals involved in the hole/electron transfer processes are estimated using both the charge transfer integrals (CTI) method implemented in ADF<sup>41-43</sup>, and the Constrained DFT (CDFT) computational scheme<sup>44-46</sup> implemented in the software package CPMD<sup>47</sup>.

#### **3.2.5.1. Charge transfer integral (CTI) method**

This formalism computes the CTI through the equation:

$$H_{DA}^{CTI} = J_{DA} - \frac{1}{2} S_{DA} (e_D + e_A) \quad (3.3)$$

Here,  $J_{DA}$  represents the off-diagonal elements of the Fock matrix constructed using the HOMOs (for hole transfer calculations) or the LUMOs (for electron transfer) of the molecular subunits used as donor (D) or acceptor (A).  $S_{DA}$  is the overlap integral between the molecular orbitals of the two states considered, while  $e_D$  and  $e_A$  are the energies of the system bearing the electron/hole on the donor or the acceptor. These calculations are performed at the B3LYP/TZP level in dichloromethane simulated through the continuum solvation model COSMO.

#### **3.2.5.2. Constrained DFT (CDFT)**

This methodology is based on the idea of minimizing the Kohn-Sham energy functional under the constraint that the charge difference between two defined regions of space is equal to a specific value of interest (see section 2.6 of this thesis). Within the CPMD implementation, we can define these two regions of space

as the sum of the atoms constituting respectively the donor and the acceptor. For the process of hole-transfer, we consider the sub-system PTZ-phenyl-NDI<sub>1</sub> in its linear configuration. Here, PTZ and the phenyl bridge (Ph) form the donor, while NDI<sub>1</sub> is the acceptor. The electronic coupling is calculated between the two states donor<sup>+</sup>-acceptor and donor-acceptor<sup>+</sup>. Similarly, the electron coupling between NDI<sub>1</sub> and NDI<sub>2</sub> is estimated as the coupling between the two states NDI<sub>1</sub><sup>-</sup>-bridge-NDI<sub>2</sub> and NDI<sub>1</sub>-bridge-NDI<sub>2</sub><sup>-</sup>. For the bridge unit we consider either a phenyl ring, or an ethyne group; in this case the bridge is not included neither in the definition of donor nor in that of the acceptor. The CDFT calculations are performed in vacuum using the pseudopotentials of ref. <sup>48</sup> with a plane wave cut-off of 70 Rydberg.

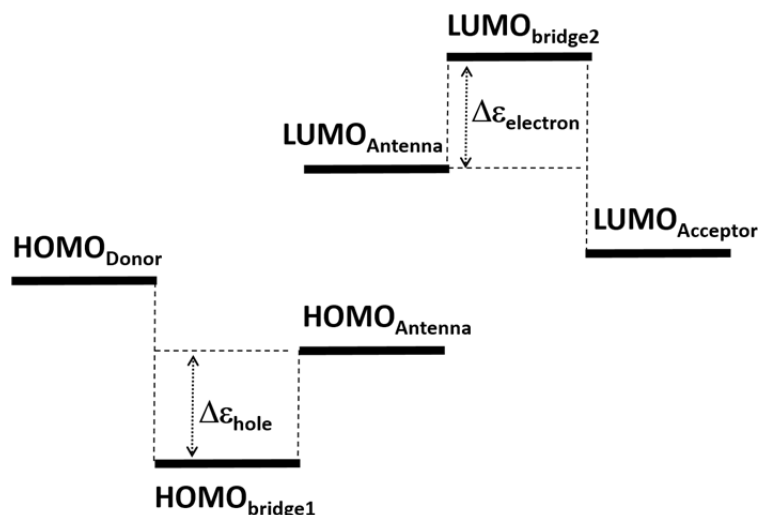
### 3.2.6. Bridge-mediated electron transfer

Depending on the structure of the triad considered, the process of hole-transfer can take place directly between donor and acceptor, or can proceed via bridge-mediated tunneling mechanism. In contrast, the electronic relaxation from NDI<sub>1</sub> to NDI<sub>2</sub> occurs as bridge-mediated electron tunneling for every system investigated. For those cases in which the charge transfer occurs through bridge-mediated tunneling, and the donor and acceptor are separated by  $M$  identical bridge units, the overall donor-acceptor electronic coupling is calculated following the McConnell's formalism<sup>49</sup>:

$$H_{DA}^{BM} = \frac{h_{Db}}{\Delta\varepsilon} \left( \frac{h_{bb}}{\Delta\varepsilon} \right)^{M-1} h_{bA} \quad (3.4)$$

In equation 3.4,  $h_{Db}$ ,  $h_{bA}$  and  $h_{bb}$  represent the coupling between a bridge unit and respectively the donor, the acceptor and another bridge unit (if present). These terms are calculated using both the CTI or the CDFT methods.

The other parameter,  $\Delta\varepsilon$ , represents either the hole, or the electron tunneling energy gap imposed by the bridge (**Scheme 3.3**). The height of the hole tunneling barrier ( $\Delta\varepsilon_{\text{hole}}$ ) is calculated as the difference between the HOMO energy values of the antenna and the bridge1 interposed between donor and antenna.



**Scheme 3.3.** Energy diagram of the Donor-Antenna-Acceptor orbitals used to calculate the energy barriers for the hole and electron tunneling, to be used in equation 3.4.

In contrast, for the electron tunneling,  $\Delta\varepsilon_{\text{electron}}$  is calculated as the energy difference between the LUMOs of the antenna and of bridge2, interposed between the antenna and the acceptor. It has been verified that this method provides values of  $\Delta\varepsilon$  very similar to those calculated with the computationally more expensive CDFT method by constraining the charge over the bridge.

Equation 3.4 is the generalized form of the McConnell's formalism, where  $M > 0$ . Since in this chapter the electronic coupling is calculated only for systems in which  $M=1$ , the second term on the right hand side of equation 3.4 becomes equal to 1. This formalism is applied only to the calculation of the coupling between states which are not delocalized over bridge units.

### **3.3.RESULTS AND DISCUSSION**

We initially present in section 3.3.1 the results of the TD-DFT analysis performed on a series of molecules used as benchmark to assess the quality of the results given by different GGA and hybrid *xc*-functionals, in reproducing the experimental absorption spectra published by Matile et al<sup>23,50</sup>. This analysis is useful to understand the level of theory required to accurately describe the optical response of the investigated triads to their initial photoexcitation.

An accurate calculation of the ground and excited state oxidation potentials of the chosen molecular subunits is essential to verify that the donor, antenna and acceptor moieties do indeed create the redox gradient required for the unidirectional charge transfer. In section 3.3.2 we compare the computed redox values obtained using the method described in section 3.2.3, with the experimental cyclic voltammetry data<sup>19</sup>.



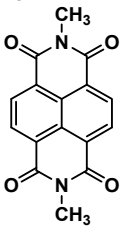
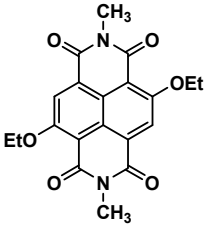
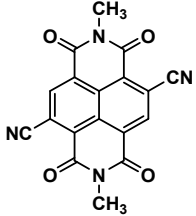
In section 3.3.3 and 3.3.4 we extend the TD-DFT study of molecular optical properties to a set of triads on which we apply specific structural changes. We study how these modifications affect the energetics of each excited state by TD-DFT geometry optimization. Starting from the systems showing the most promising thermodynamics we further modify the molecular structure in order to optimize also the electron-coupling between donor, antenna and acceptor. Finally, for the optimized molecular rectifier we estimate the charge separation rate constant.

### 3.3.1. xc-functional benchmarking for TD-DFT absorption spectra

TD-DFT studies are performed on the benchmark compounds NDI<sub>1</sub>, NDI<sub>2</sub> and NDI<sub>0</sub><sup>16,22,23</sup> making use of the exchange-correlation (xc) functionals OPBE<sup>51</sup>, SAOP<sup>52,53</sup>, OPBE0<sup>54</sup>, B3LYP<sup>55</sup> and M06<sup>56,57</sup>.

In **Table 3.1** we compare the calculated and the experimental values of the first characteristic absorption peak of each molecule investigated.

**Table 3.1.** Excitation energies analysis of the reference compounds NDI<sub>0</sub>, NDI<sub>1</sub>, NDI<sub>2</sub> performed with TD-DFT and various xc-functionals. The experimental value is also reported for comparison.

	<sup>a</sup> HF <sub>x</sub>	<sup>b</sup> transition	<sup>c</sup> f	<sup>d</sup> λ <sub>abs</sub> (nm)	<sup>e</sup> E <sub>g</sub> (eV)
<b>NDI<sub>0</sub></b> 	OPBE 0%	<b>H → L (98%)</b>	0.46	433	2.86
	SAOP 0%	<b>H → L (98%)</b>	0.47	443	2.80
	B3LYP 20%	<b>H → L (99%)</b>	0.59	409	3.04
	OPBE0 25%	<b>H → L (99%)</b>	0.61	391	3.17
	M06 25%	<b>H → L (98%)</b>	0.61	390	3.17
	Exp.				380
<b>NDI<sub>1</sub></b> 	OPBE 0%	<b>H → L (97%)</b>	0.31	561	2.21
	SAOP 0%	<b>H → L (98%)</b>	0.30	539	2.30
	B3LYP 20%	<b>H → L (99%)</b>	0.42	482	2.54
	OPBE0 25%	<b>H → L (98%)</b>	0.43	466	2.66
	M06 25%	<b>H → L (99%)</b>	0.43	474	2.62
	Exp.				470
<b>NDI<sub>2</sub></b> 	B3LYP 20%	<b>H → L (97%)</b>	0.47	424	2.92
	OPBE0 25%	<b>H → L (99%)</b>	0.49	406	3.05
	M06 25%	<b>H → L (99%)</b>	0.48	411	3.01
	Exp.				380

<sup>a</sup> Amount of exact HF-exchange for each functional. <sup>b</sup> Main molecular orbital transition (relative percentage) associated to electronic excitation E<sub>g</sub>. <sup>c</sup> Oscillator strength. <sup>d</sup> Maximum absorption wavelength corresponding to the computed electronic excitation energy. <sup>e</sup> Electronic excitation energy computed in methanol. Experimental values in methanol are adapted from references [22] and [23].

These results clearly indicate that hybrid and meta-hybrid functionals (B3LYP, OPBE0, and M06) are able to predict the lowest excitation energies of the benchmark molecules with much higher accuracy compared to the GGA functional OPBE<sup>51</sup> and the model potential SAOP<sup>52,53</sup>, which considerably underestimate the experimental values.

### 3.3.2. Redox potential calculations

To verify the presence of a potential gradient between the donor, the antenna and the acceptor suitable to induce charge separation, we compute the ground and excited state redox potentials of each subunit following the procedure described in section 3.2.3. As shown in **Table 3.2**, the redox values calculated at the B3LYP/DCM (COSMO) level compare well with the experimental cyclic voltammetry onset values<sup>22,23,26</sup>. These results overall confirm the validity of the applied method and computational set up. Considering also the positive results obtained with TD-DFT (B3LYP reproduces the NDI<sub>1</sub> excitation energy within 0.1 eV from the experiment), the choice of the hybrid B3LYP functional appears to be appropriate for studying the electronic and optical properties of molecular complexes employing these functional subunits.

**Table 3.2.** Ground ( $\Delta G_{ox}$ ) and excited state ( $\Delta G_{ox}^{ES}$ ) molecular redox potentials estimated for each molecular component of the triad.

Molecule	Redox Pot.	<sup>a</sup> E <sub>exp</sub> (eV)	<sup>b</sup> E <sub>calc</sub> (eV)
NDI <sub>1</sub>	$\Delta G_{ox}$	-6.16 <sup>22</sup>	-6.21
	$\Delta G_{ox}^{ES}$	-3.82 <sup>22</sup>	-3.68
NDI <sub>2</sub>	$\Delta G_{ox}$	-7.50 <sup>23</sup>	-7.53
	$\Delta G_{ox}^{ES}$	-4.50 <sup>23</sup>	-4.60
PTZ	$\Delta G_{ox}$	-4.77 <sup>26</sup>	-4.86

<sup>a</sup> Experimental onset redox potentials (measured in dichloromethane). <sup>b</sup> Redox potential values computed using B3LYP xc-functional in DCM (COSMO) model. All data are reported vs. vacuum.

### 3.3.3. Optical excitations and excited state geometrical optimizations

The electronic structure of system **0** (see **Figure 3.1**) is obtained at the ground state geometry after optimization in dichloromethane, for consistency with the redox potentials calculations. The frontier orbitals are depicted in **Figure 3.2**.

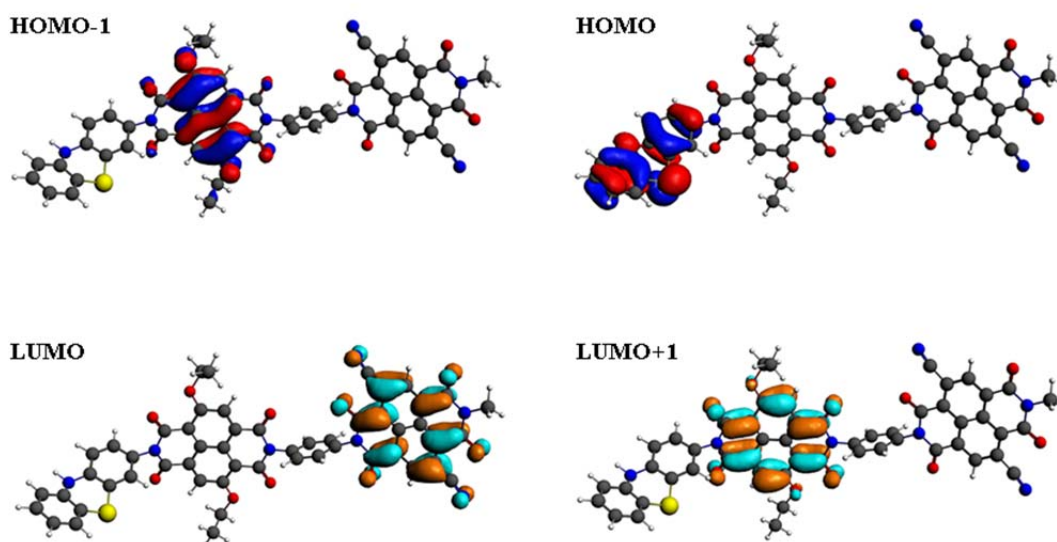


**Figure 3.2.** Frontier molecular orbitals of triad **0** obtained at the B3LYP/TZP level of theory in DCM solvent.

As expected from the ground and excited state oxidation potential calculations, the HOMO and the LUMO are highly localized on the donor and the acceptor respectively, while the HOMO-1 and the LUMO+1 reside on the antenna. Each of these four orbitals possesses the same symmetry of those involved in the main excitation of the subunits calculated separately. The absorption spectrum calculated for system **0** (**Figure 3.3**, black line) shows a dominant peak around 500 nm, corresponding to the photoinitiated HOMO-1 to LUMO+1 transition. **Figure 3.3** shows for comparison also the spectra computed for the monomers NDI<sub>1</sub> and NDI<sub>2</sub>, respectively in blue and red dotted lines. The most noticeable difference between these spectra is represented by a 18 nm (0.04 eV) red shift of the first absorption peak of triad **0** with respect to that of the isolated NDI<sub>1</sub>. Similar shifts are observed for the absorption spectra estimated using the *xc*-functionals OPBE0 (0.08 eV) and OPBE (0.07 eV). This red-shift reveals the influence of the substituents coupled to the imide groups on the transition energy of the antenna.

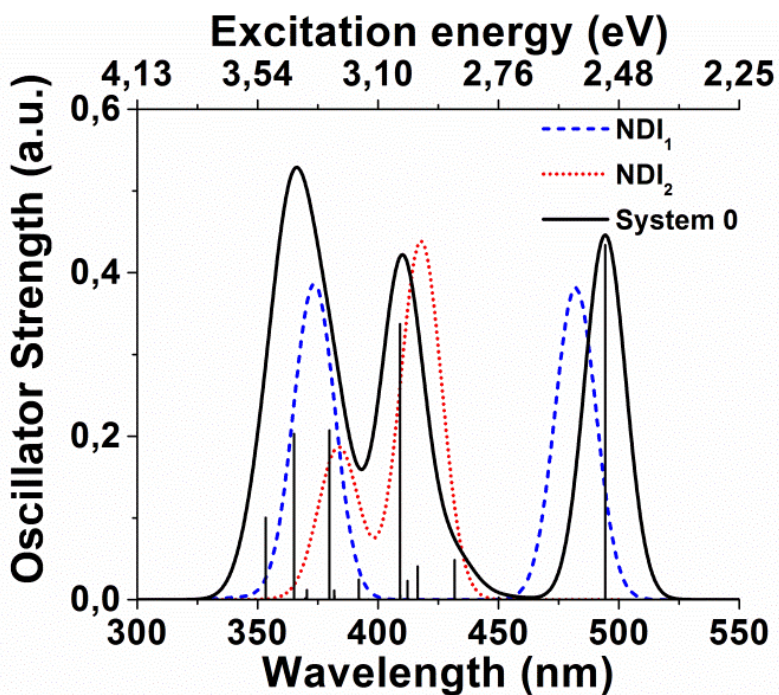


**Figure 3.3.** Optical absorption spectra computed with TD-DFT/B3LYP for NDI<sub>1</sub> (blue dashes), NDI<sub>2</sub> (red dots), and for the whole triad system **0** (black curve). The black solid lines represent the calculated excitations contributing to the absorption spectra of system **0**. TD-DFT calculations are performed in DCM (COSMO) using the TZP basis set, within ADF.

The differences between the excited states oxidation potentials of NDI<sub>1</sub> and NDI<sub>2</sub>, as well as between the ground states potentials of PTZ and NDI<sub>1</sub> (**Table 3.2**), imply the presence of driving forces across the linking motifs that represent tunneling barriers separating the components of the triad. Consequently, photoexcitation of the antenna creates the conditions for the exothermic formation of a full charge separated state where the photogenerated positive hole and the excited electron are localized respectively on the donor and the acceptor.

To investigate how structural changes can influence the probability of formation of different excited states after photoabsorption, we performed TD-DFT geometry optimizations in the electronic states S<sub>0</sub>, S<sub>1</sub> and S<sub>2</sub>, for each of the aforementioned systems. The geometrical parameters of the systems optimized for different excited states are summarized in **Table A3.1** in the appendix. For all the investigated cases we observe that in its neutral state, the phenothiazine is bent around the N-S axis with an angle of  $\sim 146.8^\circ$  while, after oxidation (excited states S<sub>1</sub> and S<sub>2</sub>), the molecule assumes a fully planar configuration. This indicates that this particular degree of freedom can be associated with the process of charge transfer between donor and antenna. Moreover, we observe that the dihedral angle between the PTZ and the directly bound phenyl bridge assumes different values depending on the

configuration of PTZ. When the PTZ is in a perpendicular configuration (see **Figure 3.1**) this angle is close to  $90^\circ$ , while for PTZ in the linear configuration it is found to be  $\sim 36^\circ$ , which is consistent with previously studied systems containing phenyl bridges<sup>58</sup>. The variation of this torsional angle has an important effect on the conjugation of donor and bridge units, and thus on the relative stability of different excited states.

We also observe that optimization in  $S_0$  does not lead to any major geometrical change compared to the ground state, independently of the rectifier considered. The maximum energy difference evaluated at the ground state PES between the geometries optimized in the ground and the excitonic states is  $\sim 0.01$  eV. This is at least one order of magnitude smaller than the difference calculated for the geometries optimized in any other excited state. The energy minimum of  $S_0$  is used as reference point to appreciate how the energies of  $S_1$  and  $S_2$  are affected by structural modifications.

In the context of the Marcus theory of electron transfer, the excitonic state  $S_0$ , populated upon photoexcitation, is considered as the reactant state and the fully charge separated state  $S_1$  as the product state. In contrast, the intermediate state  $S_2$  represents an unwanted product state and its formation has to be avoided (see **Scheme 3.2**). Within this framework, the energy difference between the minima of the reactant and each of the product states ( $\Delta E$ ), is considered the driving force for the corresponding electron transfer reactions.

To calculate the exact thermodynamic driving force, the energies of the system optimized in  $S_0$ ,  $S_1$  and  $S_2$ , should be corrected for the entropic term. An explicit calculation of this term, however, becomes computationally too demanding for such extended systems.

For large molecular triads similar to the ones investigated here, it has been argued that the entropic term  $T\Delta S$  represents a minor correction to the free energy difference, compared to  $\Delta E$  between optimized excited states<sup>33,59</sup>. Thus, in the following analysis the entropic contributions are neglected, leading to the approximation  $\Delta E \approx \Delta G$ . Hence, the term  $\Delta G$  is used to indicate the energy difference (or driving force) between the minima of the optimized excited states.

**Figure 3.4** and **Table 3.3** show the comparison between the PESs obtained through excited states geometry optimizations of the different charge separators.

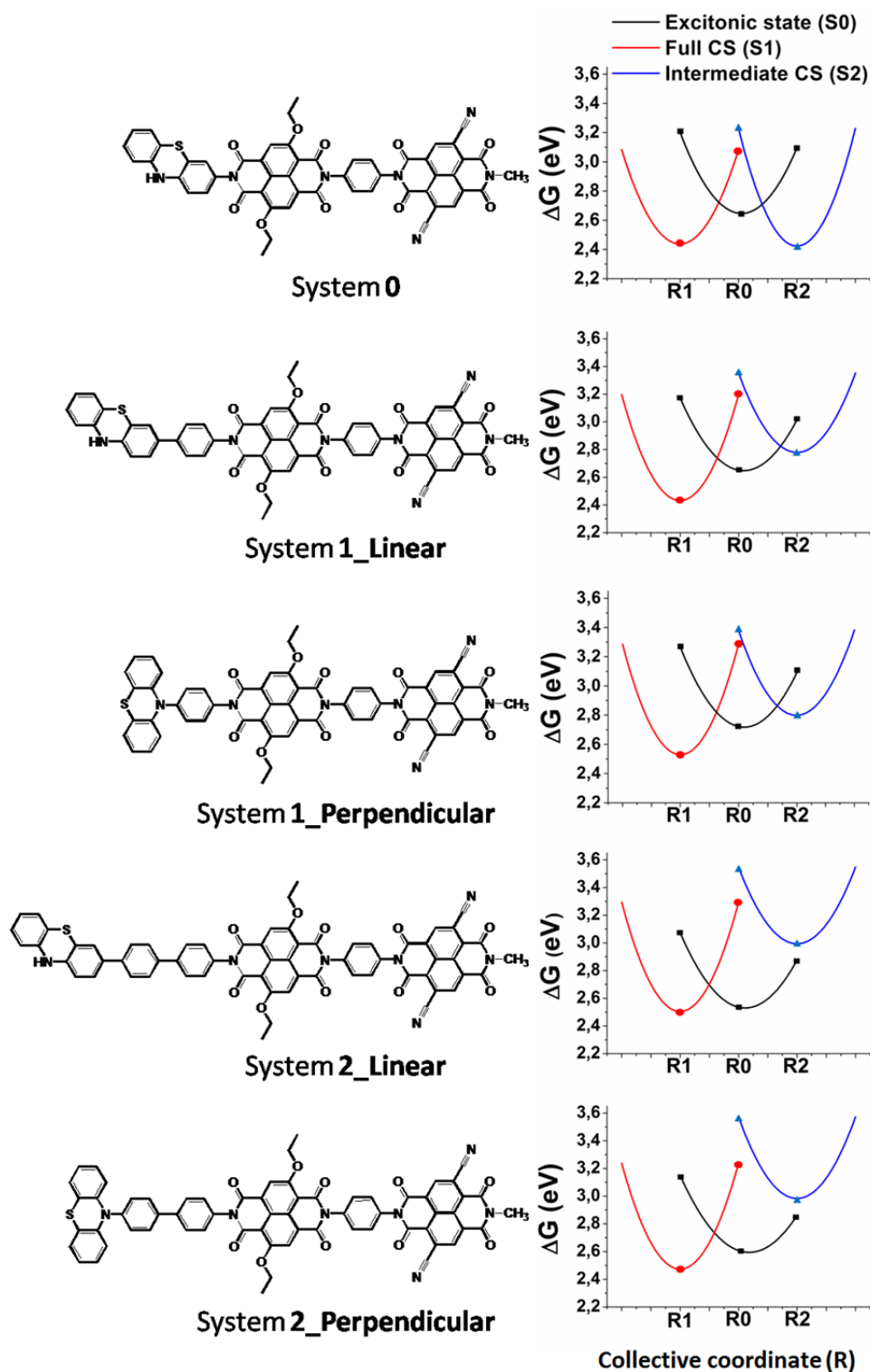


**Figure 3.4.** Potential energy surfaces for the antenna-localized exciton state S0 (black), the fully charge separated state S1 (red), and the intermediate charge separated state S2, representing the hole displacement from An to D (blue). The energies are obtained with TD-DFT geometry optimizations at the CAM-B3LYP/cc-pVDZ level and reported relative to the minimal energy of the ground state along a nuclear collective coordinate R. R0, R1 and R2 represent the geometries optimized for each excited state (**Table A3.1** in the appendix). The symbols along the curves represent the energy values used to construct the parabolas and calculate the reorganization energies  $\lambda$  and the energy differences between the excited states S0, S1 and S2 reported in **Table 3.3**.

**Table 3.3.** Minimal energy differences  $\Delta G$  between excited state PES and reorganization energies  $\lambda$  calculated for the investigated systems.

	<b>S1-S0</b>		<b>S2-S0</b>		<b>S1-S2</b>	
	$\Delta G$ (eV)	$\lambda$ (eV)	$\Delta G$ (eV)	$\lambda$ (eV)	$\Delta G$ (eV)	$\lambda$ (eV)
System <b>0</b>	-0.21	0.65	-0.22	0.80	0.014	0.41
System <b>1 Linear</b>	-0.22	0.76	0.13	0.57	-0.35	0.40
System <b>1 Perpendicular</b>	-0.19	0.75	0.08	0.58	-0.27	0.38
System <b>2 Linear</b>	-0.031	0.79	0.46	0.55	-0.49	0.39
System <b>2 Perpendicular</b>	-0.13	0.76	0.38	0.59	-0.51	0.50

$\Delta G$  values are calculated as the energy difference between the minima of the different excited state PESs ( $S_n-S_m$ ) obtained through TD-DFT geometry optimization at the CAM-B3LYP/cc-pVDZ level of theory.  $\lambda$  is the reorganization energy calculated along the potential energy surfaces.

The first thing to notice in **Table 3.3** and **Figure 3.4** is that for system **0** the reactant state  $S_0$  is energetically higher than the two nearly degenerate product states  $S_1$  and  $S_2$ . This implies that both states can be energetically accessed from  $S_0$ , and that the driving forces are equal for the formation of either one of them.

The insertion of a phenyl bridge between PTZ and  $\text{NDI}_1$  has a destabilizing effect for the intermediate state  $S_2$ , both in the linear and perpendicular triads (system **1\_Linear** and system **1\_Perpendicular** in **Figure 3.4**). This effect is further enhanced by adding a second phenyl bridge (see system **2\_Linear** and system **2\_Perpendicular** in **Figure 3.4**). The results summarized in **Table 3.3** show a linear dependence of  $\Delta G$  ( $S_2-S_0$ ) on the donor-antenna distance ( $R_{D-An}$ ). In particular, it is found that the destabilization of  $S_2$  is linearly dependent on the number of bridge units introduced, with each ring corresponding to  $R_{D-An}$  increasing by  $\approx 4.3$  Å. The destabilization per ring is equivalent to 0.35 eV for the linear systems, and to 0.30 eV for the perpendicular ones. This observation is relevant to design a system in which the formation of the unwanted product state  $S_2$  can be avoided in favor of  $S_1$ .

The energy of the  $S_1$  minimum does not significantly change for systems with different bridge lengths (**Figure 3.4**). However, **Table 3.3** shows that the insertion of a first phenyl ring between donor and antenna only marginally affects  $\Delta G$  ( $S_1-S_0$ ), while the insertion of a second ring significantly reduces the thermodynamic force with respect to the excitonic state, especially for the linear case. This effect appears to be induced mostly by a shift of the energy minimum of  $S_0$ .

Overall, these results indicate system **1** as the best design choice for the optimization of the driving force towards the full charge separated state. The use of a phenyl bridge to separate the antenna from both the donor and the acceptor, favors the transition between the reactant state  $S_0$  to the product state  $S_1$ . At the same time, it destabilizes the intermediate state  $S_2$  with respect to  $S_0$ , in such a way that

a spontaneous transition between them is impossible.

Thus, the S1 state is expected to be formed by a concerted transfer of an hole from the antenna to the donor and an electron from the antenna towards the acceptor (see **Scheme 3.2**). In the following section 3.3.4 the reasons for a preference between the perpendicular or the linear geometry for system **1** are discussed.

### 3.3.4. Charge transfer integrals and charge separation rates

So far our analysis has been focused on the effects that structural changes have on the energy gradients between different excited states. However, in order to assess the charge separation efficiency of a particular triad we cannot limit our analysis solely to the system's thermodynamics. Indeed, although Marcus<sup>60</sup> theory (see section 1.4) defines the electron-transfer rate constant ( $k_{ET}$ , equation 3.5) between two electronic states as directly dependent on their energy difference ( $\Delta G$ ) and the reorganization energy ( $\lambda$ ),

$$k_{ET} = \frac{2\pi}{\hbar} \frac{2}{\sqrt{4\pi\lambda k_B T}} |H_{DA}|^2 \exp\left(-\frac{(\Delta G + \lambda)^2}{4\lambda k_B T}\right) \quad (3.5)$$

the probability of this process to occur is strictly correlated also to the electron coupling term ( $H_{DA}$ ), which relates to the degree of mixing between those two electronic states.

As it will be shown in chapter 4, coherent electron-nuclear motion can have crucial effects on electron tunneling processes since it can drive the system towards the crossing point of the initial and final states, where the electron transfer takes place.

**Table 3.4** summarizes the electronic coupling between the different subunits calculated for both the linear and perpendicular system **1** using both the CTI and CDFT methods.

The orbital analysis of system **1** in its linear and perpendicular geometries show highly localized frontier molecular orbitals that strongly resemble those already discussed for system **0**. The only difference is represented by the HOMO of system **1\_Linear**, which appears to be delocalized over both the PTZ and the phenyl bridge. This indicates that the bridge does no longer constitute a barrier in the process of hole-transfer between the antenna and the electron donor, but instead it is a part of the donor group.

This delocalization is no longer observed in system **1\_perpendicular**, where the phenyl bridge acts as barrier for the transfer. The energy difference between the



HOMO of the antenna and the first occupied orbital localized on the bridge, is much smaller than the energy difference between the HOMO of the donor and LUMO of the bridge. The charge transfer between donor and antenna is therefore expected to occur primarily as a hole rather than as an electron transfer process, since the tunneling barrier imposed by the bridge is considerably smaller for the first process<sup>61</sup>.

The delocalization of the LUMO or the LUMO+1 over the bridge in between the antenna and the acceptor is never observed for any of the investigated systems. The electron transfer between antenna and acceptor thus proceeds via electron tunneling through the bridge.

To calculate the coupling between the electronic states involved in the formation of the charge separated state S1, the donor-bridge-antenna and antenna-bridge-acceptor subsystems, listed in **Table 3.4** (first column), are studied separately. The analysis of the first group of systems gives the coupling for the hole transfer process between antenna and donor, while the second group of compounds allows for the estimation of the coupling values associated to the electron transfer between antenna and acceptor. NDI<sub>1</sub>-C≡C-NDI<sub>2</sub> is added to the list to decrease the electron tunneling energy barrier height imposed by the phenyl bridge and allow for rotation between the two naphthalene diimides.

To clarify **Table 3.4**, it is worth pointing out the following:

- (i)  $H_{DA}$  values reported (CTI or CDFT) represent the coupling between the electron or the hole donor and acceptor units, depending on the investigated system.
- (ii) In system PTZ-Ph-NDI<sub>1</sub> (L) the HOMO is delocalized over both the PTZ and the phenyl unit. Thus, the latter does no longer constitute a barrier and the McConnell equation can no longer be applied. The  $H_{DA}^{CTI}$  value is therefore obtained by applying the CTI method, defining PTZ-Ph as the hole acceptor unit, and NDI<sub>1</sub> as the hole donor.
- (iii) For all the other cases, no delocalization is observed over the bridge units, that therefore do constitute energy barriers for either hole or electron transfer. The  $H_{DA}^{CTI}$  values reported in the table are thus obtained by solving equation 3.4 for the  $\Delta\varepsilon$  values reported in the table, and the donor-bridge and acceptor-bridge coupling values calculated with the CTI method (not shown).

The CTI and CDFT formalisms give comparable results, despite a different level of theory and environmental constraints applied. Hence the procedure to estimate the tunneling barrier is relatively robust.

**Table 3.4.** Comparison between the coupling values for hole- and electron-transfer, estimated via CTI and Constrained DFT methods.

	$H_{DA}^{CTI}$ (meV)	$\Delta\epsilon_{hl}$ (meV)	$H_{DA}^{CDFT}$ (meV)
<b>Hole transfer</b> Antenna $\rightarrow$ Donor			
<b>PTZ-Ph-NDI<sub>1</sub> (L)</b>	8	-	3
<b>PTZ-Ph-NDI<sub>1</sub> (P)</b>	0.3	1000	-
	$H_{DA}^{CTI}$ (meV)	$\Delta\epsilon_{el}$ (meV)	$H_{DA}^{CDFT}$ (meV)
<b>Electron Transfer</b> Antenna $\rightarrow$ Acceptor			
<b>NDI<sub>1</sub>-Ph-NDI<sub>2</sub></b>	0.04	2400	0.05
<b>NDI<sub>1</sub>-C<math>\equiv</math>C-NDI<sub>2</sub></b>	23	820	43.5

Electron/hole coupling values  $H_{DA}$  and tunneling barriers  $\Delta\epsilon_{hl/el}$  calculated for the subsystems listed in the first column. (L) and (P) indicate the linear or perpendicular configuration of phenothiazine with respect to the phenyl bridge (Ph). CTI Calculations are performed with ADF at the B3LYP/TZP level of theory in DCM (COSMO). The same computational set-up is used to calculate the tunneling-energy gap<sup>62</sup>,  $\Delta\epsilon_{hl/el}$ .  $H_{DA}^{CTI}$  values represent the electron coupling between donor-antenna or antenna-acceptor. The McConnell formalism has been used to calculate the coupling only of those systems for which  $\Delta\epsilon_{hl/el}$  values are reported. Similar hole/electron transfer energy barrier values are obtained using the CDFT approach (not shown).  $H_{DA}^{CDFT}$ : coupling values obtained employing the Constrained DFT method implemented in the CPMD package; the CDFT calculations are performed in vacuum, using the BLYP functional and a plane wave cut-off of 70 Ry.

The results shown in **Table 3.4** highlight the large effect of having PTZ linked to the phenyl-bridge in a linear or a perpendicular configuration. The electronic coupling between the hole donor (NDI<sub>1</sub>) and the acceptor (PTZ) is reduced by more than one order of magnitude for the perpendicular system.

Binding the PTZ to the phenyl bridge through the amine group of the electron donor, results in loss of conjugation between the two groups. This prevents a strong mixing of the electronic states of the two groups, reduces the electronic coupling and promotes the separation of their energy levels. This results in the bridge imposing a large barrier (1 eV) for the hole-transferring process. On the contrary, conjugation between the PTZ and the bridge is achieved by binding the two in a linear configuration. This allows for strong overlap between the orbitals of the two subunits, resulting into the delocalization, and stabilization, of the supramolecular complex HOMO over both the PTZ and the bridge. Thus, Ph does no longer constitute a barrier for hole transfer; instead it becomes a part of the electron donor. The distance between the hole donor and acceptor is thus reduced, while their electronic coupling is increased.

The use of Ph as bridge unit between NDI<sub>1</sub> and NDI<sub>2</sub> induces a large electron

tunneling barrier (2.4 eV), and reduces the electronic coupling between the two practically to zero. The substitution of the Ph bridge with an acetylene group leads to an increase of the antenna-acceptor electron coupling of four orders of magnitude (**Table 3.4**). This can be explained in terms of the reduced electron donor-acceptor distance imposed by the new bridge, and with the fact that the LUMO of the acetylene is energetically much lower compared to the LUMO of Ph.

By applying this latter change to the structure of system **1\_Linear**, we obtain system **1-b\_Linear** shown in **Figure 3.5**.

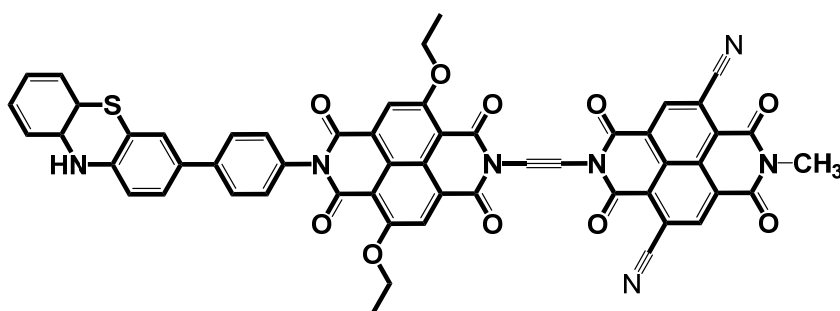


**Figure 3.5.** Schematic representation of the molecular rectifier **1-b\_Linear** optimized for ultrafast formation of the charge separated state S1.

The driving force computed for this triad between S0 and S1, gives  $\Delta G = -0.26$  eV, with a reorganization energy  $\lambda = 0.7$  eV. Instead, the formation of S2 is found to be energetically unfavorable with  $\Delta G = 0.1$  eV, and  $\lambda = 0.9$  eV.

Since the formation of the product state S1 takes place as a concerted hole and electron displacement (see **Scheme 3.2**, left panel), we can reasonably assume that the kinetic bottleneck for this process is represented by the hole transfer from the antenna to the donor. In fact, the electronic coupling calculated between the donor and the antenna in the linear configuration (8 meV, in **Table 3.4**) is weaker than the one between the antenna and the acceptor when connected through an ethyne linker ( $\text{NDI}_1\text{-C}\equiv\text{C-NDI}_2$ , 23 meV in **Table 3.4**). Under this assumption, we can employ equation 3.5 to estimate the rate of formation for S1. By using the values  $H_{DA} = 0.008$  eV,  $\Delta G = -0.26$  eV and  $\lambda = 0.7$  eV, a rate constant  $k_{ET} = 1.24 \cdot 10^{12} \text{ s}^{-1}$  is obtained, which is similar to the rate of  $5 \cdot 10^{12} \text{ s}^{-1}$  experimentally observed for the process of hole transfer between a perylene and a phenothiazine linked through a *p*-phenylene oligomer.

### **3.4.CONCLUSIONS**

With the goal of engineering a molecular triad able to induce a stable charge separated state upon visible light absorption, we design several complexes employing PTZ, NDI<sub>1</sub>, and NDI<sub>2</sub> respectively as electron donor, antenna and electron acceptor, using different linkages between these subunits. The investigation of the optical properties performed for each triad reveals a predominant  $\pi-\pi^*$  excitation around 500 nm associated with the antenna-localized excited state S<sub>0</sub>. The relative energetic stability of this initial excited state with respect to the excited states with charge transfer character is found to be dependent on the donor-antenna distance. The separation of these two moieties by means of one phenyl ring appears to be the optimal compromise to ensure a strong driving force for the formation of the fully charge separated state S<sub>1</sub> starting from S<sub>0</sub> and prevent the occurrence of competing quenching paths for the excitonic state.

It is found that a strong coupling between the donor and antenna is achieved when the PTZ is linked to the phenyl bridge through one of its peripheral aromatic rings. At the same time the ethyne group is shown to provide a strong electronic coupling between the antenna and the acceptor moieties.

Based on these findings, we propose the molecular rectifier PTZ-Ph-NDI<sub>1</sub>-C≡C-NDI<sub>2</sub>, as a promising triad for photoinduced direct ultrafast charge separation. Recombination of the photoinduced CS state to the ground state is expected to be strongly delayed due to the long distance and large energy barrier between donor and acceptor imposed by the other molecular components. Additionally, in an ensemble where multiple rectifiers are stacked through  $\pi-\pi$  interactions, the n-type semiconductor behavior of NDI<sub>2</sub> will have two major advantages: it will further delay charge recombination by delocalizing the electron in the bulk and allow the creation of a p-n junction with a suitable electrode such as silicon. The next steps currently under investigation are a more comprehensive description of the dynamics associated with the ET process and the substitution of the electron donor with a water oxidation catalyst to develop a genuine artificial photosynthesis device<sup>58</sup>.

### 3.5. REFERENCES

- (1) Young, K. J.; Martini, L. A.; Milot, R. L.; Snoeberger III, R. C.; Batista, V. S.; Schmuttenmaer, C. A.; Crabtree, R. H.; Brudvig, G. W. Light-Driven Water Oxidation for Solar Fuels. *Coordination Chemistry Reviews* **2012**, *256* (21–22), 2503–2520.
- (2) Xiao, D.; Martini, L. A.; Snoeberger, R. C.; Crabtree, R. H.; Batista, V. S. Inverse Design and Synthesis of Acac-Coumarin Anchors for Robust TiO<sub>2</sub> Sensitization. *J. Am. Chem. Soc.* **2011**, *133* (23), 9014–9022.
- (3) Negre, C. F. A.; Milot, R. L.; Martini, L. A.; Ding, W.; Crabtree, R. H.; Schmuttenmaer, C. A.; Batista, V. S. Efficiency of Interfacial Electron Transfer from Zn-Porphyrin Dyes into TiO<sub>2</sub> Correlated to the Linker Single Molecule Conductance. *J. Phys. Chem. C* **2013**, *117* (46), 24462–24470.
- (4) Martini, L. A.; Moore, G. F.; Milot, R. L.; Cai, L. Z.; Sheehan, S. W.; Schmuttenmaer, C. A.; Brudvig, G. W.; Crabtree, R. H. Modular Assembly of High-Potential Zinc Porphyrin Photosensitizers Attached to TiO<sub>2</sub> with a Series of Anchoring Groups. *J. Phys. Chem. C* **2013**, *117* (28), 14526–14533.
- (5) Akimov, A. V.; Neukirch, A. J.; Prezhdo, O. V. Theoretical Insights into Photoinduced Charge Transfer and Catalysis at Oxide Interfaces. *Chem. Rev.* **2013**, *113* (6), 4496–4565.
- (6) Yang, W. S.; Noh, J. H.; Jeon, N. J.; Kim, Y. C.; Ryu, S.; Seo, J.; Seok, S. I. SOLAR CELLS. High-Performance Photovoltaic Perovskite Layers Fabricated through Intramolecular Exchange. *Science* **2015**, *348* (6240), 1234–1237.
- (7) Jeon, N. J.; Noh, J. H.; Yang, W. S.; Kim, Y. C.; Ryu, S.; Seo, J.; Seok, S. I. Compositional Engineering of Perovskite Materials for High-Performance Solar Cells. *Nature* **2015**, *517* (7535), 476–480.
- (8) Moser, C. C.; Keske, J. M.; Warncke, K.; Farid, R. S.; Dutton, P. L. Nature of Biological Electron Transfer. *Nature* **1992**, *355* (6363), 796–802.
- (9) Noy, D.; Moser, C. C.; Dutton, P. L. Design and Engineering of Photosynthetic Light-Harvesting and Electron Transfer Using Length, Time, and Energy Scales. *Biochimica et Biophysica Acta (BBA) - Bioenergetics* **2006**, *1757* (2), 90–105.
- (10) Allen, J. F. Photosynthesis of ATP—electrons, Proton Pumps, Rotors, and Poise. *Cell* **2002**, *110* (3), 273–276.
- (11) Golbeck, J. H. Structure, Function and Organization of the Photosystem I Reaction Center Complex. *Biochimica et Biophysica Acta (BBA) - Reviews on Bioenergetics* **1987**, *895* (3), 167–204.
- (12) Gust, D.; Moore, T. A.; Moore, A. L. Solar Fuels via Artificial Photosynthesis. *Acc. Chem. Res.* **2009**, *42* (12), 1890–1898.
- (13) Andrea Rozzi, C.; Maria Falke, S.; Spallanzani, N.; Rubio, A.; Molinari, E.; Brida, D.; Maiuri, M.; Cerullo, G.; Schramm, H.; Christoffers, J.; et al. Quantum Coherence Controls the Charge Separation in a Prototypical Artificial Light-Harvesting System. *Nat Commun* **2013**, *4*, 1602.
- (14) Yella, A.; Lee, H.-W.; Tsao, H. N.; Yi, C.; Chandiran, A. K.; Nazeeruddin, M. K.; Diau, E. W.-G.; Yeh, C.-Y.; Zakeeruddin, S. M.; Grätzel, M. Porphyrin-Sensitized Solar Cells with Cobalt (II/III)-Based Redox Electrolyte Exceed 12 Percent Efficiency. *Science* **2011**, *334* (6056), 629–634.
- (15) Megiatto Jr, J. D.; Méndez-Hernández, D. D.; Tejeda-Ferrari, M. E.; Teillout, A.-L.; Llansola-Portolés, M. J.; Kodis, G.; Poluektov, O. G.; Rajh, T.; Mujica, V.; Groy, T. L.; et al. A Bioinspired Redox Relay That Mimics Radical Interactions of the Tyr-His Pairs of Photosystem II. *Nat Chem* **2014**, *6* (5), 423–428.
- (16) Nattestad, A.; Mozer, A. J.; Fischer, M. K. R.; Cheng, Y.-B.; Mishra, A.; Bäuerle, P.; Bach, U. Highly Efficient Photocathodes for Dye-Sensitized Tandem Solar Cells. *Nat Mater* **2010**, *9* (1), 31–35.
- (17) Listorti, A.; O'Regan, B.; Durrant, J. R. Electron Transfer Dynamics in Dye-Sensitized Solar Cells. *Chem. Mater.* **2011**, *23* (15), 3381–3399.

- (18) Suraru, S.-L.; Würthner, F. Core-Tetrasubstituted Naphthalene Diimides by Stille Cross-Coupling Reactions and Characterization of Their Optical and Redox Properties. *Synthesis* **2009**, 2009 (11), 1841–1845.
- (19) Supur, M.; El-Khouly, M. E.; Seok, J. H.; Kay, K.-Y.; Fukuzumi, S. Elongation of Lifetime of the Charge-Separated State of Ferrocene–Naphthalenediimide–[60]Fullerene Triad via Stepwise Electron Transfer. *J. Phys. Chem. A* **2011**, 115 (50), 14430–14437.
- (20) Wenger, O. S. Long-Range Electron Transfer in Artificial Systems with d6 and d8 Metal Photosensitizers. *Coordination Chemistry Reviews* **2009**, 253 (9–10), 1439–1457.
- (21) Steyrlleuthner, R.; Schubert, M.; Howard, I.; Klaumünzer, B.; Schilling, K.; Chen, Z.; Saalfrank, P.; Laquai, F.; Facchetti, A.; Neher, D. Aggregation in a High-Mobility N-Type Low-Bandgap Copolymer with Implications on Semicrystalline Morphology. *J. Am. Chem. Soc.* **2012**, 134 (44), 18303–18317.
- (22) Kishore, R. S. K.; Kel, O.; Banerji, N.; Emery, D.; Bollot, G.; Mareda, J.; Gomez-Casado, A.; Jonkheijm, P.; Huskens, J.; Maroni, P.; et al. Ordered and Oriented Supramolecular N/p-Heterojunction Surface Architectures: Completion of the Primary Color Collection. *J. Am. Chem. Soc.* **2009**, 131 (31), 11106–11116.
- (23) Sakai, N.; Mareda, J.; Vauthey, E.; Matile, S. Core-Substituted Naphthalenediimides. *Chem. Commun.* **2010**, 46 (24), 4225–4237.
- (24) Bhosale, S. V.; Jani, C. H.; Langford, S. J. Chemistry of Naphthalene Diimides. *Chemical Society Reviews* **2008**, 37 (2), 331.
- (25) Jones, B. A.; Facchetti, A.; Marks, T. J.; Wasielewski, M. R. Cyanonaphthalene Diimide Semiconductors for Air-Stable, Flexible, and Optically Transparent N-Channel Field-Effect Transistors. *Chem. Mater.* **2007**, 19 (11), 2703–2705.
- (26) Gomurashvili, Z.; Crivello, J. V. Phenothiazine Photosensitizers for Onium Salt Photoinitiated Cationic Polymerization. *Journal of Polymer Science Part A: Polymer Chemistry* **2001**, 39 (8), 1187–1197.
- (27) Jones, B. A.; Facchetti, A.; Wasielewski, M. R.; Marks, T. J. Tuning Orbital Energetics in Arylene Diimide Semiconductors. Materials Design for Ambient Stability of N-Type Charge Transport. *J. Am. Chem. Soc.* **2007**, 129 (49), 15259–15278.
- (28) Guerra, C. F.; Snijders, J. G.; Velde, G. te; Baerends, E. J. Towards an Order-N DFT Method. *Theor Chem Acc* **1998**, 99 (6), 391–403.
- (29) Te Velde, G.; Bickelhaupt, F. M.; Baerends, E. J.; Fonseca Guerra, C.; van Gisbergen, S. J. A.; Snijders, J. G.; Ziegler, T. Chemistry with ADF. *Journal of Computational Chemistry* **2001**, 22 (9), 931–967.
- (30) Te Velde, G.; Bickelhaupt, F. M.; Baerends, E. J.; Fonseca Guerra, C.; van Gisbergen, S. J. A.; Snijders, J. G.; Ziegler, T. Chemistry with ADF. *J. Comput. Chem.* **2001**, 22 (9), 931–967.
- (31) Pye, C. C.; Ziegler, T. An Implementation of the Conductor-like Screening Model of Solvation within the Amsterdam Density Functional Package. *Theor Chem Acc* **1999**, 101 (6), 396–408.
- (32) Grimme, S.; Antony, J.; Ehrlich, S.; Krieg, H. A Consistent and Accurate Ab Initio Parametrization of Density Functional Dispersion Correction (DFT-D) for the 94 Elements H-Pu. *The Journal of Chemical Physics* **2010**, 132 (15), 154104–154104 – 19.
- (33) Pastore, M.; Fantacci, S.; De Angelis, F. Ab Initio Determination of Ground and Excited State Oxidation Potentials of Organic Chromophores for Dye-Sensitized Solar Cells. *J. Phys. Chem. C* **2010**, 114 (51), 22742–22750.
- (34) Wang, T.; Brudvig, G. W.; Batista, V. S. Study of Proton Coupled Electron Transfer in a Biomimetic Dimanganese Water Oxidation Catalyst with Terminal Water Ligands. *J. Chem. Theory Comput.* **2010**, 6 (8), 2395–2401.
- (35) Gritsenko, O.; Baerends, E. J. Asymptotic Correction of the Exchange–correlation Kernel of Time-Dependent Density Functional Theory for Long-

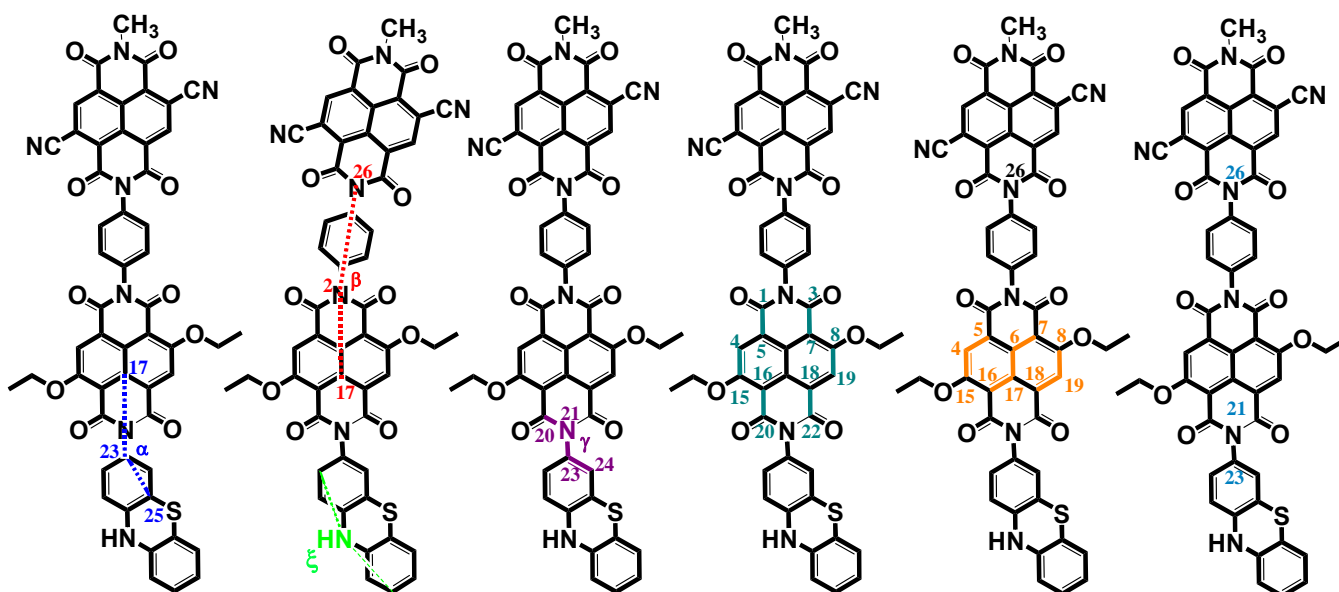
- Range Charge-Transfer Excitations. *The Journal of Chemical Physics* **2004**, *121* (2), 655–660.
- (36) Yanai, T.; Tew, D. P.; Handy, N. C. A New Hybrid Exchange–correlation Functional Using the Coulomb-Attenuating Method (CAM-B3LYP). *Chemical Physics Letters* **2004**, *393* (1–3), 51–57.
- (37) Jacquemin, D.; Planchat, A.; Adamo, C.; Mennucci, B. TD-DFT Assessment of Functionals for Optical 0–0 Transitions in Solvated Dyes. *J. Chem. Theory Comput.* **2012**, *8* (7), 2359–2372.
- (38) Tawada, Y.; Tsuneda, T.; Yanagisawa, S.; Yanai, T.; Hirao, K. A Long-Range-Corrected Time-Dependent Density Functional Theory. *The Journal of Chemical Physics* **2004**, *120* (18), 8425–8433.
- (39) M. J. Frisch, G. W. Trucks, H. B. Schlegel, G. E. Scuseria, M. A. Robb, J. R. Cheeseman, G. Scalmani, V. Barone, B. Mennucci, G. A. Petersson, et al. *Gaussian 09, Revision D.01*; Gaussian, Inc.: Wallingford CT, 2009.
- (40) Tomasi, J.; Mennucci, B.; Cammi, R. Quantum Mechanical Continuum Solvation Models. *Chem. Rev.* **2005**, *105* (8), 2999–3093.
- (41) Newton, M. D. Quantum Chemical Probes of Electron-Transfer Kinetics: The Nature of Donor-Acceptor Interactions. *Chem. Rev.* **1991**, *91* (5), 767–792.
- (42) Senthilkumar, K.; Grozema, F. C.; Bickelhaupt, F. M.; Siebbeles, L. D. A. Charge Transport in Columnar Stacked Triphenylenes: Effects of Conformational Fluctuations on Charge Transfer Integrals and Site Energies. *The Journal of Chemical Physics* **2003**, *119* (18), 9809–9817.
- (43) Senthilkumar, K.; Grozema, F. C.; Guerra, C. F.; Bickelhaupt, F. M.; Lewis, F. D.; Berlin, Y. A.; Ratner, M. A.; Siebbeles, L. D. A. Absolute Rates of Hole Transfer in DNA. *J. Am. Chem. Soc.* **2005**, *127* (42), 14894–14903.
- (44) Oberhofer, H.; Blumberger, J. Electronic Coupling Matrix Elements from Charge Constrained Density Functional Theory Calculations Using a Plane Wave Basis Set. *The Journal of Chemical Physics* **2010**, *133* (24), 244105–244105 – 10.
- (45) Oberhofer, H.; Blumberger, J. Charge Constrained Density Functional Molecular Dynamics for Simulation of Condensed Phase Electron Transfer Reactions. *The Journal of Chemical Physics* **2009**, *131* (6), 064101–064101 – 11.
- (46) Wu, Q.; Voorhis, T. V. Extracting Electron Transfer Coupling Elements from Constrained Density Functional Theory. *The Journal of Chemical Physics* **2006**, *125* (16), 164105.
- (47) CPMD, <http://www.cpmc.org/>, Copyright IBM Corp 1990-2008, Copyright MPI für Festkörperforschung Stuttgart 1997-2001.
- (48) Goedecker, S.; Teter, M.; Hutter, J. Separable Dual-Space Gaussian Pseudopotentials. *Phys. Rev. B* **1996**, *54* (3), 1703–1710.
- (49) McConnell, H. M. Intramolecular Charge Transfer in Aromatic Free Radicals. *The Journal of Chemical Physics* **1961**, *35* (2), 508–515.
- (50) Kishore, R. S. K.; Kel, O.; Banerji, N.; Emery, D.; Bollot, G.; Mareda, J.; Gomez-Casado, A.; Jonkheijm, P.; Huskens, J.; Maroni, P.; et al. Ordered and Oriented Supramolecular N/p-Heterojunction Surface Architectures: Completion of the Primary Color Collection. *J. Am. Chem. Soc.* **2009**, *131* (31), 11106–11116.
- (51) Perdew, J. P.; Burke, K.; Ernzerhof, M. Generalized Gradient Approximation Made Simple. *Phys. Rev. Lett.* **1996**, *77* (18), 3865–3868.
- (52) Gritsenko, O. V.; Schipper, P. R. T.; Baerends, E. J. Approximation of the Exchange-Correlation Kohn–Sham Potential with a Statistical Average of Different Orbital Model Potentials. *Chemical Physics Letters* **1999**, *302* (3–4), 199–207.
- (53) Schipper, P. R. T.; Gritsenko, O. V.; van Gisbergen, S. J. A.; Baerends, E. J. Molecular Calculations of Excitation Energies and (hyper)polarizabilities with a Statistical Average of Orbital Model Exchange-Correlation Potentials. *The Journal of Chemical Physics* **2000**, *112* (3), 1344–1352.
- (54) Swart, M.; Ehlers, A. W.; Lammertsma, K. Performance of the OPBE Exchange-Correlation Functional. *Molecular Physics* **2004**, *102* (23–24), 2467–2474.

- 
- (55) Reiher, M.; Salomon, O.; Hess, B. A. Reparameterization of Hybrid Functionals Based on Energy Differences of States of Different Multiplicity. *Theor Chem Acc* **2001**, *107* (1), 48–55.
- (56) Zhao, Y.; Truhlar, D. The M06 Suite of Density Functionals for Main Group Thermochemistry, Thermochemical Kinetics, Noncovalent Interactions, Excited States, and Transition Elements: Two New Functionals and Systematic Testing of Four M06-Class Functionals and 12 Other Functionals. *Theoretical Chemistry Accounts: Theory, Computation, and Modeling (Theoretica Chimica Acta)* **2008**, *120* (1), 215–241.
- (57) Zhao, Y.; Truhlar, D. G. A New Local Density Functional for Main-Group Thermochemistry, Transition Metal Bonding, Thermochemical Kinetics, and Noncovalent Interactions. *The Journal of Chemical Physics* **2006**, *125* (19), 194101–194101 – 18.
- (58) Weiss, E. A.; Ahrens, M. J.; Sinks, L. E.; Gusev, A. V.; Ratner, M. A.; Wasielewski, M. R. Making a Molecular Wire: Charge and Spin Transport through Para-Phenylene Oligomers. *J. Am. Chem. Soc.* **2004**, *126* (17), 5577–5584.
- (59) Pratik, S. M.; Datta, A. Computational Design of Concomitant Type-I and Type-II Porphyrin Sensitized Solar Cells. *Phys. Chem. Chem. Phys.* **2013**, *15* (42), 18471–18481.
- (60) Marcus, R. A. On the Theory of Oxidation-Reduction Reactions Involving Electron Transfer. I. *The Journal of Chemical Physics* **1956**, *24* (5), 966–978.
- (61) Hanss, D.; Wenger, O. S. Tunneling Barrier Effects on Photoinduced Charge Transfer through Covalent Rigid Rod-Like Bridges. *Inorg. Chem.* **2009**, *48* (2), 671–680.
- (62) Wenger, O. S. How Donor–Bridge–Acceptor Energetics Influence Electron Tunneling Dynamics and Their Distance Dependences. *Acc. Chem. Res.* **2011**, *44* (1), 25–35.



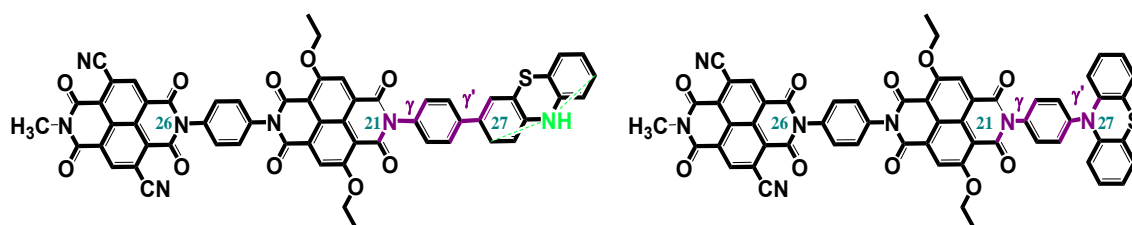
## 3.6. APPENDIX

**Table A3.1.** Geometrical parameters of the studied systems optimized in the ground state (B3LYP) and for the excited states of interest (CAM-B3LYP). For system 0 we compare the B3LYP and CAM-B3LYP results for the excited state S0. The geometrical parameters and the atomic labeling used in the table are explained in the schematic representation of the model systems.

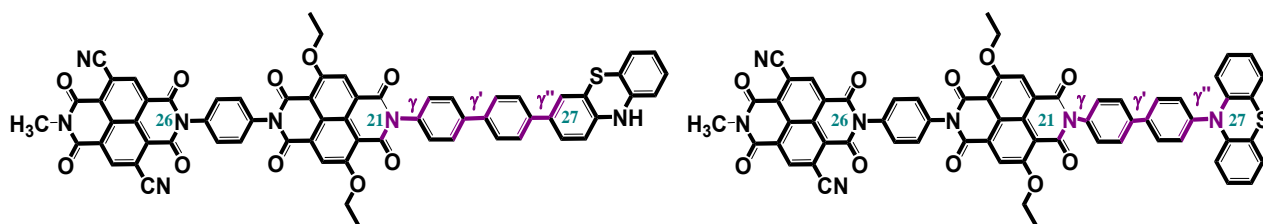


System 0	B3LYP (optimized GS)	B3LYP (optimized S0)	CAM-B3LYP (optimized S0)	CAM-B3LYP (optimized S1)	CAM-B3LYP (optimized S2)
$\alpha$ (degrees)	149.0	148.3	149.7	150.1	150.7
$\beta$ (degrees)	179.2	179.4	179.6	179.2	178.6
$\gamma$ (degrees)	-92.1	-90.4	-97.9	-114.3	-127.0
$\xi$ (degrees)	149.0	146.8	146.8	180.0	180.0
$\delta$ 21-23 (Angstrom)	1.47	1.45	1.44	1.43	1.42
$\delta'$ 23-26 (Angstrom)	14.19	14.19	14.13	14.12	14.06
1-5	1.48	1.47	1.46	1.48	1.46
3-7	1.48	1.48	1.48	1.48	1.46
4-15	1.42	1.40	1.40	1.42	1.38
8-9	1.42	1.40	1.40	1.42	1.39
15-20	1.48	1.48	1.47	1.47	1.45
18-22	1.49	1.47	1.46	1.48	1.45
SUM (A)	8.77	8.70	8.68	8.75	8.58
AVERAGE (A)	1.46	1.45	1.45	1.46	1.43

System 0	B3LYP (optimized GS)	B3LYP (optimized S0)	CAM-B3LYP (optimized S0)	CAM-B3LYP (optimized S1)	CAM-B3LYP (optimized S2)
4-5	1.38	1.40	1.39	1.37	1.40
4-15	1.42	1.40	1.40	1.42	1.38
6-7	1.43	1.41	1.40	1.42	1.43
6-17	1.43	1.45	1.45	1.41	1.43
16-17	1.42	1.41	1.40	1.42	1.43
8-19	1.42	1.40	1.40	1.42	1.39
18-19	1.38	1.40	1.39	1.37	1.41
SUM (A)	9.87	9.87	9.82	9.83	9.87
AVERAGE (A)	1.41	1.41	1.40	1.40	1.41



System 1 LINEAR	B3LYP (optimized GS)	CAM-B3LYP (optimized S0)	CAM-B3LYP (optimized S1)	CAM-B3LYP (optimized S2)
$\gamma$ (degrees)	-89.6	-88.6	-91.5	-98.4
$\gamma'$ (degrees)	34.0	36.4	32.5	26.7
$\xi$ (degrees)	148.9	146.8	177.5	180.0
$\delta$ 21-27 (Angstrom)	5.73	5.73	5.71	5.70
$\delta'$ 26-27 (Angstrom)	18.35	18.42	18.40	18.33
System 1 PERPENDICULAR	B3LYP (optimized GS)	CAM-B3LYP (optimized S0)	CAM-B3LYP (optimized S1)	CAM-B3LYP (optimized S2)
$\gamma$ (degrees)	-90.4	-90.1	-89.0	-90.5
$\gamma'$ (degrees)	97.8	99.1	89.8	89.8
$\xi$ (degrees)	151.1	149.7	174.0	174.2
$\delta$ 21-27 (Angstrom)	5.68	5.65	5.64	5.63
$\delta'$ 26-27 (Angstrom)	18.42	18.34	18.33	18.27



System 2 LINEAR	B3LYP (optimized GS)	CAM-B3LYP (optimized S0)	CAM-B3LYP (optimized S1)	CAM-B3LYP (optimized S2)
$\gamma$ (degrees)	-96.2	-90.9	-89.9	-89.1
$\gamma'$ (degrees)	35.0	36.7	37.0	36.1
$\gamma''$ (degrees)	32.1	37.0	33.4	31.5
$\xi$ (degrees)	154.0	148.1	177.6	177.6
$\delta$ 21-27 (Angstrom)	10.05	10.05	10.04	10.03
$\delta'$ 26-27 (Angstrom)	22.30	22.74	22.73	22.67
System 2 PERPENDICULAR	B3LYP (optimized GS)	CAM-B3LYP (optimized S0)	CAM-B3LYP (optimized S1)	CAM-B3LYP (optimized S2)
$\gamma$ (degrees)	-76.8	-94.5	-92.7	-101.3
$\gamma'$ (degrees)	45.9	37.6	39.6	40.5
$\gamma''$ (degrees)	-92.0	-98.5	-90.2	-90.5
$\xi$ (degrees)	149.4	149.0	174.0	174.1
$\delta$ 21-27 (Angstrom)	9.98	9.98	9.96	9.96
$\delta'$ 26-27 (Angstrom)	22.32	22.66	22.65	22.60

# Crucial Role of Nuclear Dynamics in Heterogeneous Electron Transfer

### **4.0.ABSTRACT**

---

*This chapter investigates the process of electron injection from a terrylene-based chromophore to a TiO<sub>2</sub> semiconductor bridged by a recently proposed phenyl-amide-phenyl molecular rectifier. The mechanism of electron transfer is studied by means of quantum electron dynamics simulations using an extended Hückel Hamiltonian. Prior to the quantum dynamics simulations, nuclear dynamics trajectories are calculated separately through ab initio Molecular Dynamics. It is found that the inclusion of the nuclear motion, in a coupled quantum-classical framework, opens a channel for coherent long range directional photoinduced electron transfer. This nonadiabatic process occurs between near-degenerate donor and acceptor states. In particular, the fluctuations of the dihedral angle between the terrylene and the phenyl ring modulate the localization and thus the electronic coupling between the donor and acceptor states. The electron propagation shows characteristic oscillatory features that correlate with interatomic distance fluctuations in the bridge. Hence the system acts as a "phonon antenna" to specific vibrational modes obtained in the ab initio molecular dynamics beforehand to drive the process. The understanding of coherent effects is important for the design of functional dyes with low-loss injection and rectification properties.*

---

**This chapter is based on the publication:**

Monti, A.; Negre, C.F.A.; Batista, V.S.; Rego, L.C.G.; de Groot, H.J.M.; Buda, F. Crucial Role of Nuclear Dynamics for Electron Injection in a Dye-Semiconductor Complex. *J. Phys. Chem. Lett.* **2015**, *6*, 2393-2398.

#### **4.1. INTRODUCTION**

Environmentally friendly and cost-effective dye-sensitized solar cells (DSSCs) are a potential alternative to silicon-based photovoltaics for solar energy conversion, can be equipped with molecular catalysts for direct conversion and storage of solar energy into fuel, and have been the subject of extensive research<sup>1-5</sup>. In DSSC devices a semiconductor electrode is functionalized with a (molecular) chromophore absorbing visible light. The photoexcitation induces heterogeneous electron transfer (ET) from the dye into the semiconductor conduction band (CB), while an electrolyte shuttles electrons from the counter electrode to regenerate the oxidized dye.

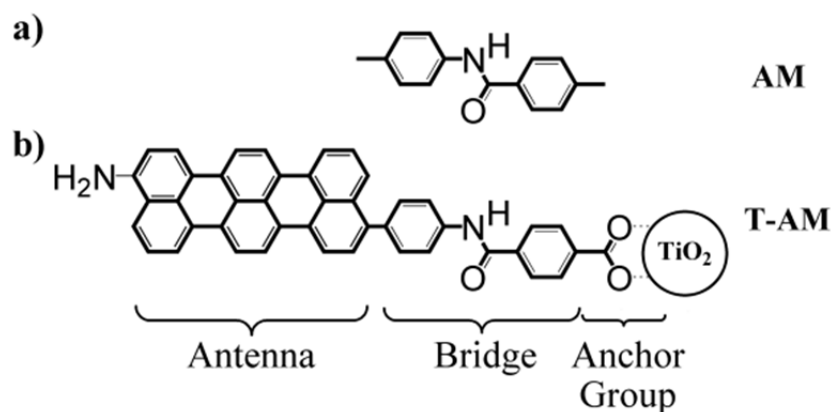
Despite considerable improvement achieved in recent years, DSSCs performances have not reached energy conversion yields and efficiency levels that are necessary to render them competitive with silicon-based solar cells. Higher efficiencies can be attained by increasing the light harvesting properties of the solar cell, by decreasing internal energy losses or by optimizing conditions for fast electron injection.

A major obstacle hampering the performance of DSSC devices is represented by the internal losses from recombination between the electron injected into the semiconductor and the hole on the oxidized dye<sup>6</sup>. In a converging approach to design more efficient devices, several groups have investigated the effect of specific cell parameters for enhancing electron injection and reducing recombination losses, such as length and nature of the bridges<sup>7-10</sup>, the chemical structure of the anchor groups<sup>11</sup> and the redox potential of the electrolyte<sup>12</sup>. In addition, detailed investigations of the molecular mechanisms at the dye/semiconductor interface<sup>13-18</sup> have revealed the importance of nonadiabatic dynamics for charge separation and recombination<sup>19-21</sup>.

Recently, Batista and coworkers proposed the use of a molecular rectifier<sup>22</sup> composed of two phenyl rings coupled through an amide bond to prevent back electron transfer (see AM molecule in **Scheme 4.1a**). This molecule acts as a rectifier when used as a molecular wire or as a linker-chromophore in a solar cell device<sup>23,24</sup>. In these previous works it has been shown that the rectifying properties of AM can be rationalized in terms of the asymmetric charge distribution of the frontier molecular orbitals. Used as a molecular bridge between a dye and a semiconductor, a rectifying AM linker could increase the DSSC efficiency by decreasing the electron-hole recombination rate.

To investigate the role of AM in the electron injection process, we use it to bridge an amine-functionalized terrylene antenna (T) and a titanium dioxide (TiO<sub>2</sub>) anatase surface (T-AM-TiO<sub>2</sub>, **Scheme 4.1b**). Terrylene is a well characterized molecule that absorbs within the visible spectrum (~580 nm) and has an excited state lifetime on

the ns time scale<sup>25,26</sup>. Recently this molecule has been also used as electron donor for TiO<sub>2</sub> based DSSC<sup>27</sup>. TiO<sub>2</sub>, in turn, is a semiconductor material widely used as an electron collector in DSSC. This oxide is known for its stability, its high surface area for dye loading, and its high electron collection efficiency; additionally, its bands allow efficient electron transfer from most of the commercially available dyes<sup>6</sup>. The anchoring of the dye onto TiO<sub>2</sub> is achieved through a carboxylic acid group in a bidentate bridging mode (**Scheme 4.1b**).



**Scheme 4.1.** Chemical structure of the molecular rectifier AM (a), and of the T-AM dye (b). The anchoring of the chromophore to the TiO<sub>2</sub> semiconductor through a carboxylic acid group (anchor group), leads to the formation of the T-AM-TiO<sub>2</sub> system.

To provide insight for the design of more efficient charge separators, I have investigated the quantum dynamics of electron injection coupled to thermal nuclear motion in a coupled quantum-classical framework where the nonadiabatic connection between successive molecular conformations is carried out through the diabatic atomic orbitals base. The semi-classical simulations show that the system is able to selectively couple to specific modes from a nuclear dynamics trajectory to open a rectifying electron injection channel in the T-AM-TiO<sub>2</sub> system by a coherent superposition of states. This mechanism is fundamentally different from a semiconductor junction, since the unidirectional conversion of the initial excited state on the chromophore is due to coherent mixing with a charge transfer state between the chromophore and the TiO<sub>2</sub>, which does not rely only on an energy gradient, but requires in addition strong electronic coupling from nearly degenerate exciton and charge transfer states. The vibronic coupling to normal modes localized at the interface between the antenna and the semiconductor drives the process. These results support recent findings on the importance of coherent vibronic coupling during photo-induced charge separation processes for both natural and artificial light-harvesting systems<sup>16,28-34</sup>.

## 4.2. METHODS AND COMPUTATIONAL DETAILS

The electronic properties of the systems are quantum mechanically described by means of a tight-binding Hamiltonian based on the extended Hückel (EH) theory<sup>35,36</sup> (see also chapter 2 of this thesis).

The EH method implementation used here, employs as basis set of  $K$  nonorthogonal Slater-type orbitals (STO) centered at the position of the respective atom in the system. A set of adiabatic molecular orbitals (MO) is constructed as linear combinations of the STO atomic orbitals (AO) according to  $\psi = \sum_{\nu=1}^K c_{\nu} \phi_{\nu}$ . It follows that the coefficients  $c_{\nu}$  are obtained by solving the generalized eigenvalue equations  $\sum_{\nu=1}^K c_{\nu} (H_{\nu\mu} - \varepsilon S_{\nu\mu}) = 0, \forall \mu = 1, K$ . Here  $H_{\nu\mu}$  and  $S_{\nu\mu}$  are respectively the electronic Hamiltonian and the overlap matrix elements in the AO basis representation, while  $\varepsilon$  is the corresponding eigenvalue. The diagonal elements  $H_{\nu\nu}$  are called Coulomb integrals. The value of each of them is assigned through parametrization and represents approximately the valence state oxidation potential of the atomic orbitals  $\nu$ . The off-diagonal elements  $H_{\nu\mu} = \frac{1}{2} k_{\nu\mu} (H_{\nu\nu} + H_{\mu\mu}) S_{\nu\mu}$  (or bond integrals) represent the energy of the electron in the region where the two atomic orbitals  $\nu$  and  $\mu$  overlap ( $S_{\nu\mu}$ ).  $k_{\nu\mu}$  are the modified empirical Wolfsberg-Helmholz parameters<sup>36,37</sup>. The matrix elements of the tight-binding EH Hamiltonian are therefore dependent on three semiempirical parameters:  $H_{\nu\nu}$ ,  $k_{\nu\mu}$  and the effective charge of the nucleus ( $\zeta$ ) embedded in the definition of the STOs.

In standard EH methods, these parameters are subject to the following approximations: i) the Coulomb integrals are approximated with the oxidation potential of the valence-shell atomic orbital; ii) no distinction based on the atom chemical environment is made for the parametrization of the AOs; iii)  $k_{\nu\mu}$  is assumed equal to 1.75. These approximations can strongly affect the outcome of the calculations, depending on the systems under investigation. To overcome these problems, for our investigation we use parameters previously optimized against experimental and DFT results. Additionally, the molecular environment is also considered during optimization through the enlargement of the AOs basis set. The optimization procedure is described in the next section 4.2.1.

### 4.2.1. Optimization of the Extended Hückel parameters

Initially, the density of states (DOS) for the (110) surface of anatase is obtained with the standard EH parameters<sup>38</sup> imposing periodic boundary conditions along the

[101] and the [010] directions. For the calculation of the isolated TiO<sub>2</sub> surface, as well as for the functionalized one, an orthorhombic supercell with lattice parameters  $a=10.239$  Å,  $b=15.137$  Å and  $c=40$  Å is used. The standard EH calculation estimates the lower edge of the TiO<sub>2</sub> conduction band (CB) at -10 eV.

At the same time, the T-AM chromophore geometry is optimized in its ground state at the DFT level, using the exchange correlation functional B3LYP<sup>39</sup> coupled with the Gaussian type basis set cc-pVDZ. The DFT calculations are performed with the Gaussian09 software package<sup>40</sup>. This computational set-up has already been proved accurate in describing the electronic properties of a similar terrylene/TiO<sub>2</sub> based DSSC device<sup>27</sup>.

Although it is experimentally difficult to obtain an accurate estimate for this parameter, -4.0 eV (vs. vacuum) is commonly accepted as an appropriate value for the edge of the TiO<sub>2</sub> CB<sup>27,41</sup>. Consequently, in order to obtain the energy gradient with respect to the semiconductor CB calculated with the EH method (-10 eV), the DFT frontier molecular orbital (FMO) energy values are down shifted by 6 eV. These corrected energies are used as target values for the optimization of the EH parameters. The optimization is performed by minimizing the cost function  $f$  of the form

$$f(\{\zeta\}, \{H_{vv}\}, \{k\}) = \sum_{j=1}^{M^{\text{CONSTR}}} \omega_j [p_j(\{\zeta\}, \{H_{vv}\}, \{k\}) - p_j^{\text{ref}}]^2 \quad (4.1)$$

where  $p_j(\{\zeta\}, \{H_{vv}\}, \{k\})$  is the system's property of interest,  $p_j^{\text{ref}}$  the target value for that property and  $\omega_j$  the relative weight of the  $j^{\text{th}}$  constraint. As shown in equation 4.1, the cost function  $f$  and the property  $p_j$  depend on the semiempirical parameters sets  $\{\zeta\}, \{H_{vv}\}, \{k\}$ . For each optimization run, it is possible to selectively optimize one or more of these parameters, for each atom in the molecule.

For the purpose of this work, the constraints are applied only to the energy values of the highest occupied molecular orbital (HOMO), the lowest and the second lowest unoccupied molecular orbital (LUMO and LUMO+1) of T-AM. The shifted DFT energies are used as target values. To evaluate the quality of the optimized EH parameters, the DFT/B3LYP and the EH orbitals are compared both in terms of their energy and their localization.

The optimization of the atomic parameters for amide and carboxylic groups is treated separately from the remaining C, N and O atoms in the molecule. In this way, specific sets of parameters are generated for those atoms, to account for



differences in chemical environments. Although this enlarges the basis set used for the calculations, it increases the accuracy of the results.

#### **4.2.2. Quantum-classical dynamics of hole/electron wavepackets**

In this chapter, the coherent mixing of the charge transfer state into the excitonic state is studied by combining quantum dynamics for the electrons, and classical molecular dynamics for the nuclei<sup>42-44</sup>.

The time evolution of the electronic wavepacket, under the influence of the underlying nuclear dynamics, is carried out through the combined AO/MO time-propagation method<sup>45</sup>. This propagation method is outlined in **Scheme 4.2**, and proceeds as follows.

The position dependent AOs used to write the initial wavepacket  $\Psi^{AO}(t)$ , for  $t = 0$

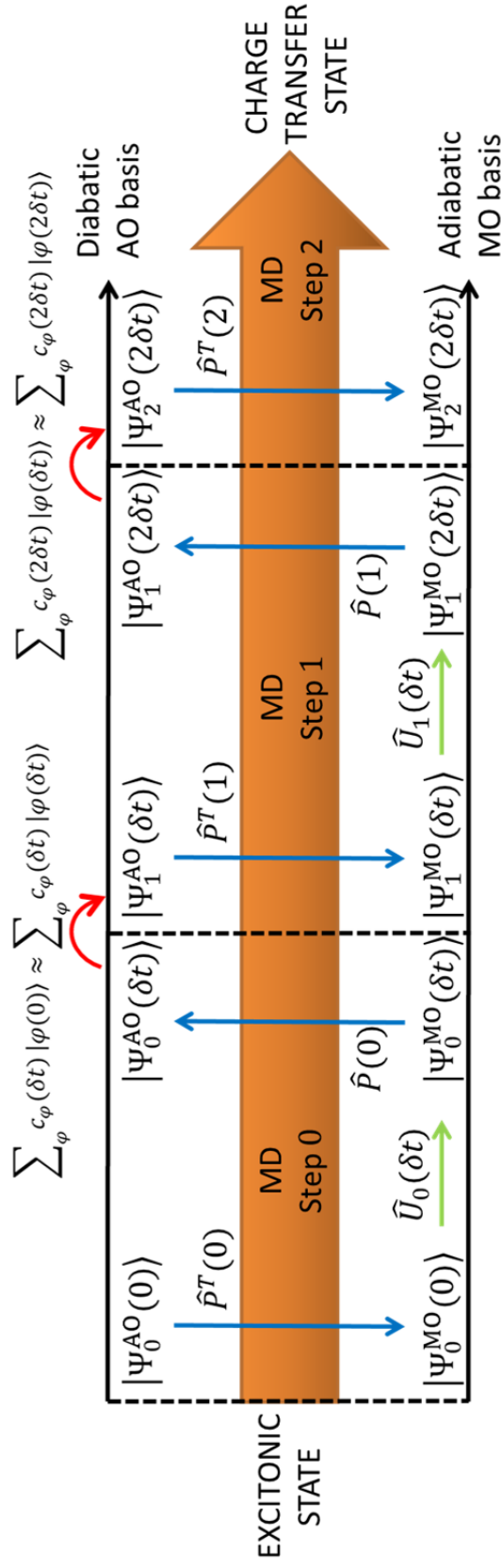
$$|\Psi^{AO}(0)\rangle = \sum_{\varphi}^{AO} c_{\varphi}(0) |\varphi(0)\rangle \quad (4.2)$$

yield the Hückel Hamiltonian matrix elements  $H_{\nu\mu}(0)$ . The Hamiltonian changes between consecutive nuclear configurations through the overlap matrix, due to the position-dependent nature of the atomic orbital basis.

Diagonalization of this Hamiltonian matrix by means of the transformation operator

$$\hat{P}^T = \sum_{\psi}^{MO} \sum_{\varphi,\chi}^{AO} |\psi\rangle\langle\psi|\varphi\rangle(S_{\varphi\chi}^{-1})\langle\varphi| \quad (4.3)$$

produces the adiabatic basis of delocalized molecular orbitals  $\{\psi(0)\}$  at  $t = 0$  (see **Scheme 4.2**, blue arrow  $\hat{P}^T(0)$ ).



**Scheme 4.2.** Schematic representation of the AO/MO time propagation method, readapted from Ref.<sup>49</sup>. The straight arrows represent the operators  $\hat{P}^T$ ,  $\hat{P}$  (blue), and  $\hat{U}$  the time propagator, green) acting on the wavepacket  $\Psi(t)$ . The wavepacket' apices AO and MO indicate whether the wavepacket is expressed in terms of atomic or molecular orbitals; the subscript numbers indicate the MD step (nuclear geometry) to which correspond the AOs used to write the wavefunction. The red arrows, connecting different MD steps, describe the transferring of the wavepacket coefficients between consecutive time slices.

The wavepacket is then expressed in the orthonormal MO basis set according to

$$|\Psi^{\text{MO}}(0)\rangle = \sum_{\psi}^{\text{MO}} c_{\psi}(0) |\psi(0)\rangle . \quad (4.4)$$

The advantage of using the molecular orbital representation is given by the simple form of the time-propagation equations, within a time slice  $\delta t$ .

In this basis, the time-propagation of the wavepacket is performed by solving the time-dependent Schrödinger equation

$$i\hbar \frac{d}{dt} |\Psi^{\text{MO}}(t)\rangle = \hat{H}(t) |\Psi^{\text{MO}}(t)\rangle . \quad (4.5)$$

Within the time slice  $\delta t$ , since the nuclear geometry is treated as static, the molecular orbitals are time-independent ( $\langle \psi | \dot{\psi}_i \rangle = 0$ ). It follows that the solution of equation 4.5, within a time slice  $\delta t$ , leads to the time evolution of the MO coefficients as

$$c_{\psi}(t) = c_{\psi}(0) \exp(-iE_{\psi} t/\hbar) . \quad (4.6)$$

In the MO basis the Hamiltonian is diagonal and  $E_{\psi}$  are its eigenvalues. From equation 4.6 it is clear that within the time slice, the time evolution is contained only in the phase factor. This time-propagation step is indicated in **Scheme 4.2** by the green arrow.

Once  $|\Psi^{\text{MO}}(\delta t)\rangle$  has been obtained, the wavepacket is transformed back to the AO basis by using the transformation operator

$$\hat{P} = \sum_{\psi}^{\text{MO}} \sum_{\varphi, \chi}^{\text{AO}} |\varphi\rangle (S_{\varphi\chi}^{-1}) \langle \chi | \psi \rangle \langle \psi | , \quad (4.7)$$

as indicated with the blue arrows  $\hat{P}(0)$  in **Scheme 4.2**.

This transformation is done since it is easier to transfer the wavepacket coefficients between time slices within the AO basis.

If  $\delta t$  is sufficiently small, we can reasonably assume that

$$\sum_{\varphi}^{AO} c_{\varphi}(\delta t) |\varphi(0)\rangle \approx \sum_{\varphi}^{AO} c_{\varphi}(\delta t) |\varphi(\delta t)\rangle, \quad (4.8)$$

which allows the transfer of  $\{c_{\varphi}(\delta t)\}$  to the next nuclear configuration, as indicated by the red arrow bridging step 0 and step 1 in **Scheme 4.2**. However, as an effect of the nuclear motion, the center of the AO basis will change between consecutive MD steps yielding  $H_{\nu\mu}(0) \neq H_{\nu\mu}(\delta t)$ .

The procedure explained for MD step 0, is reiterated along the whole trajectory.

In this investigation, to simulate the initial excitonic state induced in the terrylene dye by photo excitation ( $t=0$ ), the wavepackets for the hole and the electron are set to the HOMO and the LUMO of the adsorbate molecule, respectively. Consequently,  $\Psi(0)$  is the exciton reactant state localized on the donor. However, along the dynamics, the wavepacket evolves into the charge transfer product state by delocalizing between the donor and the acceptor.

The nuclear trajectory for the isolated molecule, used for the time-evolution of the wavepackets, is calculated beforehand through *ab initio* Molecular Dynamics using the Car-Parrinello MD (CPMD) code<sup>46</sup> (see section 2.4 of this thesis). The DFT/B3LYP optimized geometry is used as the starting point for the MD simulation, which is carried out in vacuum using the pseudopotentials of reference<sup>47</sup> with a plane wave cut-off of 70 Rydberg and the BLYP<sup>48,49</sup> exchange correlation functional. Applying the Nosé-Hoover thermostat, the T-AM molecule is brought to a temperature of 300 K and allowed to equilibrate for 2 ps using a time step of  $\delta t = 0.1$  fs. During the whole simulation, the atoms of the carboxylic acid anchoring group are constrained in their initial positions. At the end of the simulation the carboxylic acid is replaced with the previously optimized TiO<sub>2</sub> slab already functionalized with the anchoring unit.

Once the nuclear trajectory is obtained for the chromophore, the hole and the electron wavepackets are propagated along this trajectory following the combined AO/MO time-propagation method<sup>44,16</sup> described above, using the same time step of the MD simulation.

This methodology allows to treat the nonadiabatic transfer from an exciton reactant state to a charge transfer product state in the adiabatic MO representation through periodic projections onto the diabatic AO basis immediately followed by back transformation to the MO basis where the quantum electron dynamics is most conveniently performed. It has been already applied successfully for the description of heterogeneous electron transfer processes<sup>42,50,45</sup>.

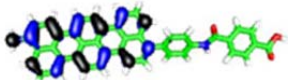
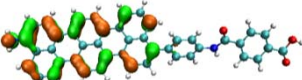
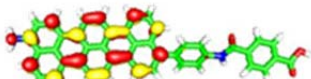
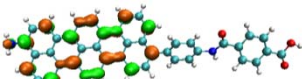
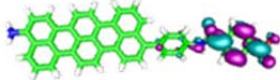
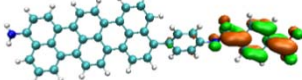
### 4.2.3. Normal mode analysis

The normal mode analysis for the isolated AM bridge unit is performed making use of the ADF software package<sup>51-53</sup>. The structure of the Phenyl-Amide-Phenyl molecule, initially optimized in vacuum at the DFT/B3LYP level, is subsequently used to numerically calculate the vibrational frequencies using the same computational set up.

## 4.3. RESULTS AND DISCUSSION

### 4.3.1. The optimized EH parameters

Following the procedure described in section 4.2.1, the DFT/B3LYP optimized structure and orbital energies of T-AM are used to carry on the optimization of the EH parameters. The results of the calculations performed with the semiempirical and the *ab initio* methods are compared in **Table 4.1**.

	DFT/B3LYP (eV)	Target values (eV)	Optimized EH (eV)
<b>HOMO</b>	<b>-4.7</b>	<b>-10.7</b>	<b>-10.7</b>
			
<b>LUMO</b>	<b>-2.6</b>	<b>-8.6</b>	<b>-8.6</b>
			
<b>LUMO+1</b>	<b>-2.4</b>	<b>-8.4</b>	<b>-8.3</b>
			

**Table 4.1.** Comparison between the frontier molecular orbital (FMO) energies obtained with the DFT/B3LYP method, the target values for the EH parameters optimizations, and the FMO energies calculated with the optimized EH parameters. The target values are estimated by applying a rigid 6 eV down shift to the DFT/B3LYP energy values. The images of the FMOs obtained for T-AM with DFT/B3LYP and the optimized EH parameters are shown for comparison.

The results clearly show that the generated set of optimized EH parameters are able to accurately reproduce the shape and the energy of the T-AM frontier molecular orbitals computed at the DFT/B3LYP level. This validates the use of this newly optimized basis set for the description of T-AM electronic properties and for studying the electron quantum dynamics processes.

### 4.3.2. Electron quantum dynamics simulations

The optimized EH parameters are used to perform a single point calculation of the entire chromophore/semiconductor system.

In **Figure 4.1a** the total density of the unoccupied states of T-AM-TiO<sub>2</sub> projected on the chromophore (Dye, in blue) and on the semiconductor (TiO<sub>2</sub>, in grey) are compared.

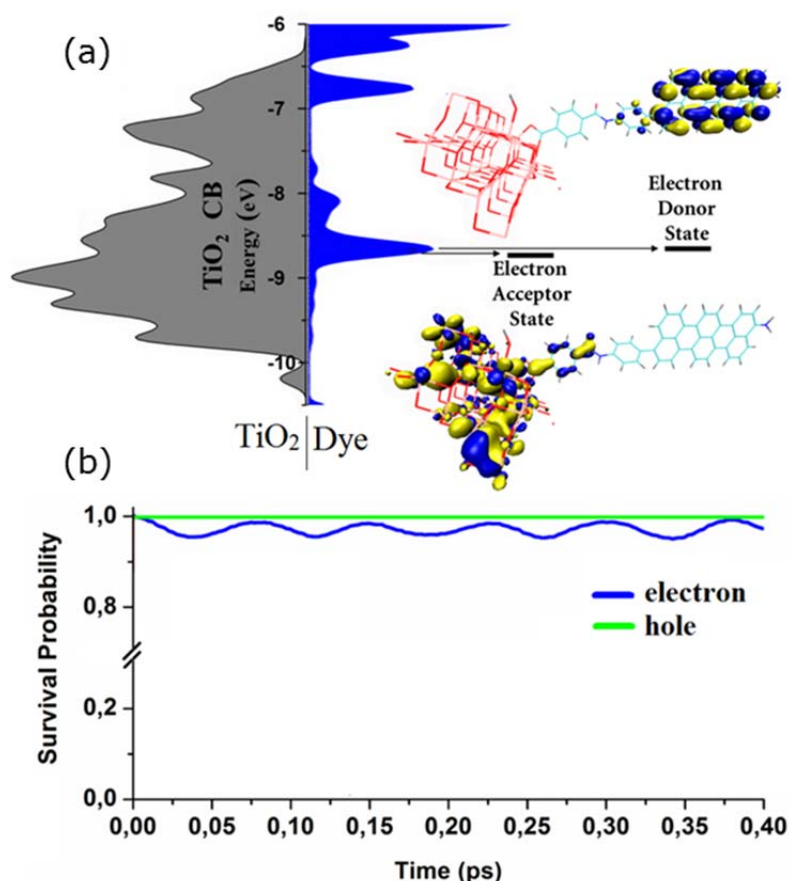


**Figure 4.1.** (a) Comparison between the density of the chromophore unoccupied states (Dye, in blue) and of the TiO<sub>2</sub> conduction band (TiO<sub>2</sub>, in grey). On the right hand side, the electron donor and acceptor states contributing to the peak around -8.7 eV are represented. (b) Electron and hole time-dependent SP profiles of system T-AM-TiO<sub>2</sub> in the absence of nuclear motion (blue and green line, respectively). The time step of the simulation is  $\delta\tau=0.1$  fs. Both calculations are performed for the entire T-AM-TiO<sub>2</sub> system on the fixed set of ground-state optimized molecular coordinates using the optimized EH parameters.

To prepare the system, the T-AM structure employed for the parametrization of the EH Hamiltonian is used. The projected density of states for T-AM (**Figure 4.1a**, Dye) presents a peak at -8.7 eV. This peak is associated with the two almost degenerate ( $\Delta\varepsilon = -0.05$  eV) unoccupied system orbitals shown in **Figure 4.1a**. These two orbitals, labeled Electron Donor (ED) and Electron Acceptor (EA) states,

correspond respectively to the LUMO and LUMO+1 of the isolated dye molecule (**Table 4.1**).

An electron quantum dynamics simulation (EQD) is performed for the T-AM-TiO<sub>2</sub> system over the same set of nuclear coordinates used for the DOS calculation, keeping the nuclear positions fixed. Since the photoexcitation of the dye populates the molecular orbital localized on the terrylene (ED), the photoexcited electron has to travel across the bridge through the EA state to reach the TiO<sub>2</sub> surface. Despite the proximity between the electron donor and acceptor states and the presence of a thermodynamic driving force, no ET from T-AM to TiO<sub>2</sub> is observed within the 2 ps EQD simulation in absence of nuclear motion (see **Figure 4.1b**).

To investigate the effect of the nuclear motion on the electron dynamics the hole/electron quantum dynamics calculations are repeated by evolving the wavepackets over a classical MD trajectory obtained beforehand (see section 4.2.2)<sup>54,55</sup>. Since we use a nuclear trajectory obtained in the ground state, the effect of the thermal relaxation of the photogenerated hot exciton is not included. However, since this effect is fast and highly localized on the antenna, it is not expected to significantly affect the dynamics of the ET on a longer time scale<sup>6</sup> (see section 4.6.1 in the Appendix). The results of the electron quantum dynamics performed along the MD trajectory are reported in **Figure 4.2** showing the survival probability (SP) of the electron wavepacket. The SP is defined as the time-dependent population of the wavepacket within the dye<sup>42</sup>. When the wavepacket is fully localized within the sensitizer SP=1, while SP=0 when it is fully transferred to TiO<sub>2</sub>.

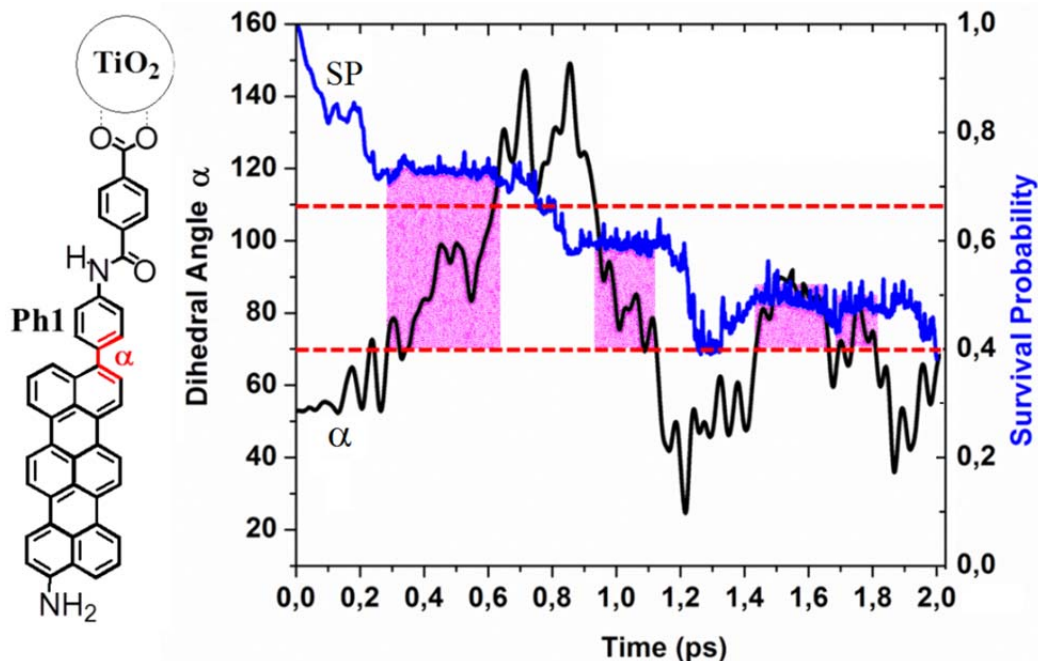


**Figure 4.2.** Electron quantum dynamics simulation of the T-AM-TiO<sub>2</sub> system (SP, blue) along a classic MD trajectory obtained with CPMD. The electron and nuclear dynamics both employ a time step  $\delta t=0.1$  fs. A schematic representation of the analyzed complex is presented on the left hand side of the figure, together with the identification of the dihedral angle  $\alpha$  (in red). The black line ( $\alpha$ ) represents the variation of this angle along the dynamics. The range of values identified as crucial for electron injection is delimited by the red dashed lines. The regions highlighted in pink correspond to time intervals in which the dihedral angle  $\alpha$  falls within this range.

The survival probability profile (**Figure 4.2**, SP) shows that the introduction of nuclear dynamics induces significant ET within the first few hundreds fs, in contrast to the results for T-AM-TiO<sub>2</sub> without nuclear dynamics (**Figure 4.1b**). This demonstrates the importance of the coupling between the electron dynamics and thermal motions in the description of ET processes.

Additionally, the SP profile is characterized by the presence of plateaus emerging periodically every  $\sim 250$  fs indicating that the electron injection is temporarily quenched. At the same time the SP evolution shows that back charge transfer from the semiconductor on the terrylene antenna does not occur, well in line with the rectifier property of the AM bridge (see section 4.6.2 in the Appendix). The analysis of the molecular dynamics trajectory reveals a correlation between the recurrence of these plateaus and the fluctuation of the dihedral angle  $\alpha$  (**Figure 4.2**, black line), defined between the terrylene and the phenyl ring Ph1 (see **Figure 4.2**, left). The electron injection occurs only when  $\alpha < 70^\circ$  or  $\alpha > 110^\circ$  (red dashed lines in **Figure 4.2**). On the contrary, if  $70^\circ < \alpha < 110^\circ$  the transfer is hindered (areas highlighted in



pink, **Figure 4.2**). The variation of the dihedral angle  $\alpha$  influences the delocalization of the electron donor state over the Ph1 ring, as shown in **Figure 4.3**.

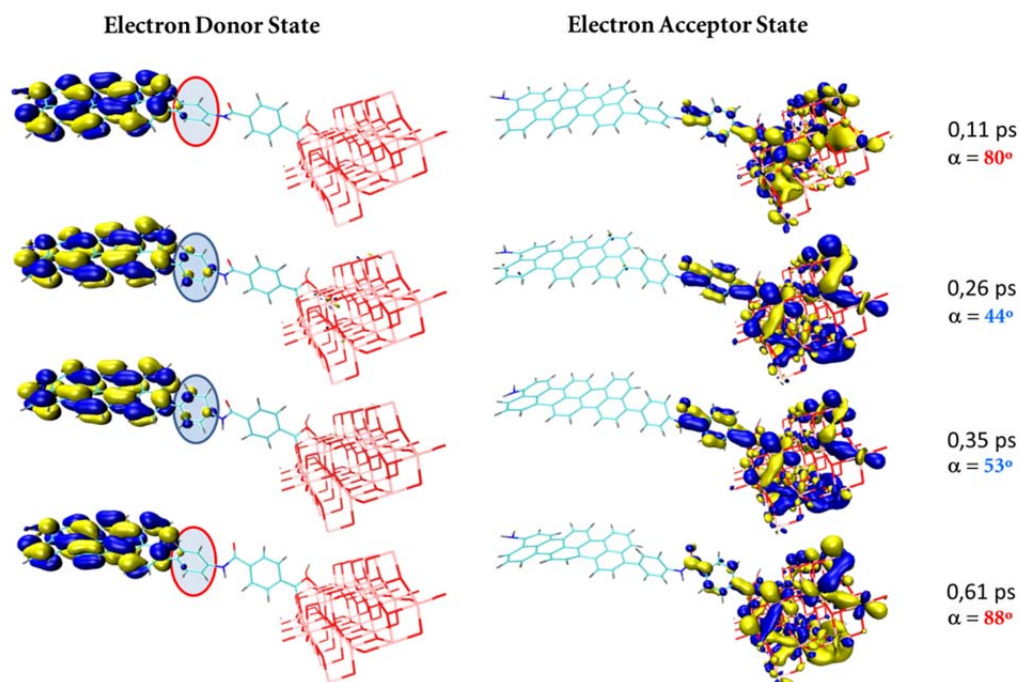


**Figure 4.3.** Localization of the Electron Donor and Electron Acceptor states along the T-AM-TiO<sub>2</sub> MD trajectory. On the right hand side are reported the MD time frames and the value of the dihedral angle  $\alpha$  corresponding to the two electronic states shown.

When  $70^\circ < \alpha < 110^\circ$  the ED state is confined on the antenna (T) and is separated from the electron acceptor orbital by the Ph1 ring (red circles in **Figure 4.3**). However, when  $\alpha$  is outside the aforementioned range the planarity and consequently the conjugation between Ph1 and the terrylene is increased. This induces the delocalization of the ED state over Ph1 (blue circles in **Figure 4.3**) and thus transiently enhances the coupling between the donor and acceptor states.

It is worth pointing out that performing the electron quantum dynamics while keeping the nuclei fixed, does not show electron injection on a timescale of a few ps, even when geometries with  $\alpha$  values outside the  $70^\circ$ - $110^\circ$  range extracted from the previous trajectory are used (as already shown in **Figure 4.1b** for the initial geometry,  $\alpha \approx 50^\circ$ ). This indicates that ET is not solely promoted by a proper value of  $\alpha$ , but instead requires the coupling with other specific vibrational modes<sup>56</sup>. To identify those we use the same nuclear trajectory to perform an EQD starting from the molecular configuration at 890 fs with  $\alpha = 123^\circ$  (**Figure 4.2**, just before the second shaded region). The results are presented in **Figure 4.4b**.

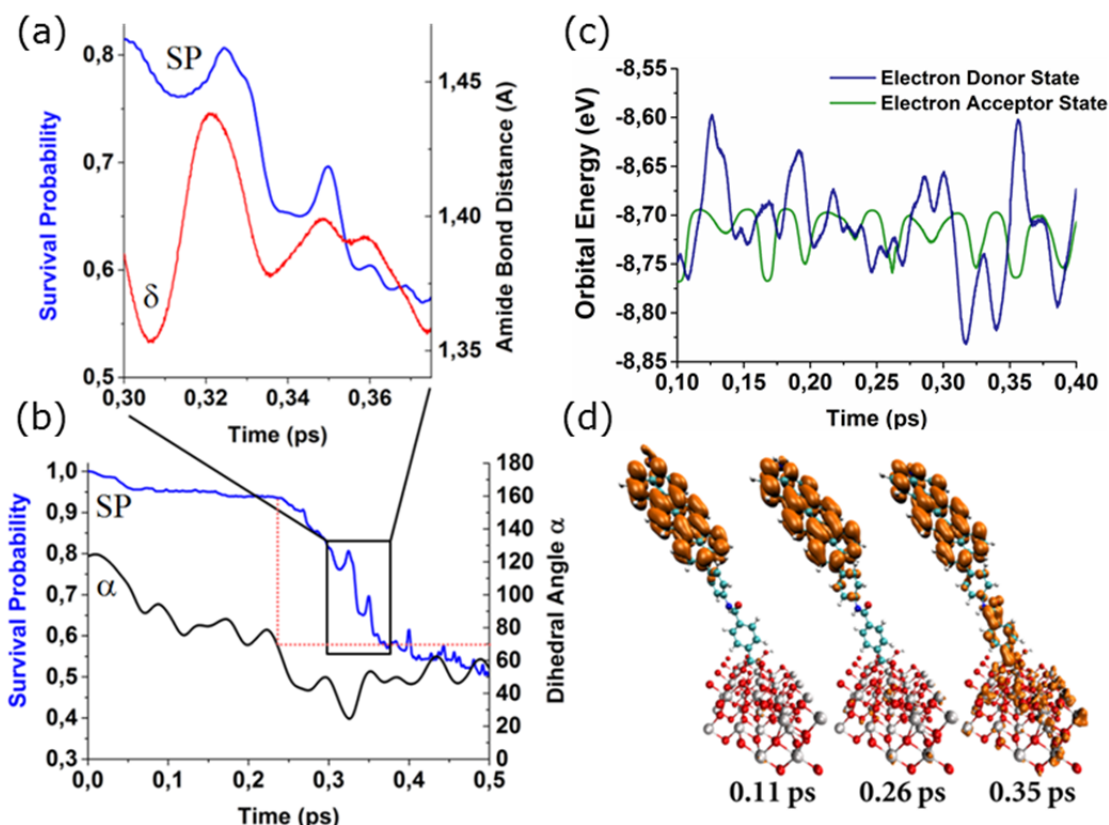


**Figure 4.4.** (a) Comparison between the survival probability (SP, blue line) oscillations and the amide bond (C-N) distance ( $\delta$ , red line) along the EQD. (b) Comparison between the electron injection profile (SP, blue line) and the variation of the dihedral angle ( $\alpha$ , black line) along the EQD simulation for the T-AM-TiO<sub>2</sub> system. The red dotted lines correlate the starting of the electron injection with the decrease of  $\alpha$  below 70°. (c) Energy values of the Electron Donor and the Electron Acceptor states along a portion of the EQD simulation. (d) Snapshots extracted along the EQD trajectory representing the electron wavepacket traveling through the bridge.

Initially, while  $\alpha > 110^\circ$ , a limited injection (5%) is observed within the first  $\sim 50$  fs. This transient is followed by a plateau up to about 230 fs, corresponding to the period during which  $70^\circ < \alpha < 110^\circ$ . Then ET towards the TiO<sub>2</sub> is resumed by the decrease of  $\alpha$  below the  $70^\circ$  threshold (red dotted lines in **Figure 4.4b**) and is characterized by electron density fluctuations with a period of  $\sim 30$  fs (**Figure 4.4b**, black rectangle). The Fourier analysis of these rapid fluctuations gives a broad peak centered at  $\sim 1250$  cm<sup>-1</sup> (see **Table 4.2a**).

In **Figure 4.4a** it is shown that the oscillations characteristic of the electron injection (SP, blue line) are highly correlated with the variation of the amide bond distance N-C ( $\delta$ , red line). A normal mode analysis of the AM bridge shows that the N-C bond length is modulated by the normal modes  $\omega_1$  (1090 cm<sup>-1</sup>) and  $\omega_2$  (1226

$\text{cm}^{-1}$ ) reported in **Table 4.2a**. In fact, as described in **Table 4.2b**, these modes involve mostly the variation of the  $\gamma$ ,  $\delta$  and  $\varepsilon$  bonds localized at the interface between the ED and EA orbitals (**Table 4.2**).

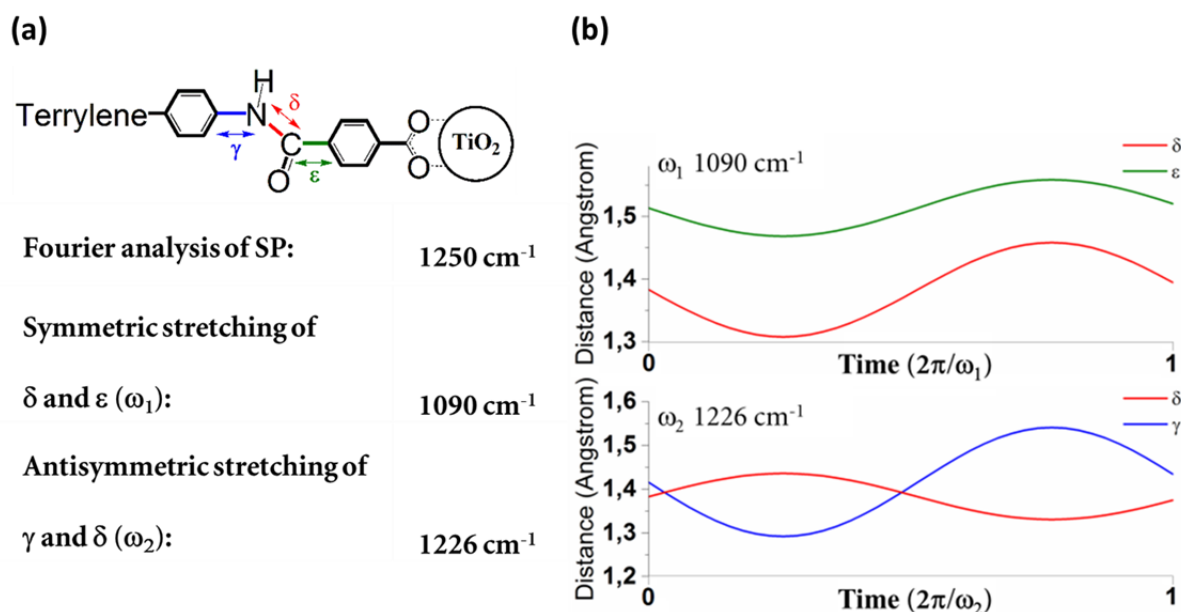


**Table 4.2.** (a) Frequencies of relevant normal modes of the AM bridge ( $\omega_1$  and  $\omega_2$ .) compared with the frequency obtained from the Fourier analysis of the electron injection oscillations along the EQD trajectory.  $\gamma$ ,  $\delta$  and  $\varepsilon$  are the three bonds showing a major contribution to the normal modes  $\omega_1$  and  $\omega_2$ . (b) Graphic representation of the  $\gamma$ ,  $\delta$  and  $\varepsilon$  bond distance variations associated to the normal modes  $\omega_1$  and  $\omega_2$ .

The energy fluctuations of these two orbitals are represented in **Figure 4.4c** for a segment of the MD trajectory (0.1-0.4 ps), characteristic of the whole simulation. The energies of EA and ED MO states constantly cross each other, which confirms the nonadiabatic character of the electron transfer process. The crossing also shows that the primary ET step and the rectification do not require a strong energy gradient to take place. The ED and EA states oscillate with distinctive frequencies of  $1100 \text{ cm}^{-1}$  and  $1235 \text{ cm}^{-1}$ , respectively. The remarkable similarity between these two values and the frequencies of the normal modes  $\omega_1$  ( $1090 \text{ cm}^{-1}$ ) and  $\omega_2$  ( $1226 \text{ cm}^{-1}$ ) strongly indicates the influence of these particular vibrations on the energies of the electron donor and acceptor states. Overall these results underline the importance of these specific nuclear vibrations in driving the electron injection. Similar evidence of vibronic coupling effects have been recently reported for different organic supramolecular complexes<sup>28,30,57</sup>.

Quantum coherent conversion from an excitonic state to a charge transfer state requires that the two states partially occupy the same volume, and that their energy

levels are close enough to be coherently coupled by vibrational modes<sup>31-33,58-60</sup>. In the system discussed here, the two states involved in the electron transfer are associated with orbitals that initially are sufficiently close in energy but spatially separated. Thermal motion brings a conformational change (variation of  $\alpha$ ) that makes them partially occupy the same molecular region. Under this condition the two states can be coherently coupled by the fast vibrational modes localized at their interface, thus allowing the propagation of the electronic wavepacket by a convergence of electronic and nuclear dynamics.

A visual representation of the electron wavepacket propagating across the system is reported in **Figure 4.4d**. These snapshots clearly show how the wavepacket propagates through a channel which is opened as a result of the Ph1 rotation. The snapshot at  $t=0.35$  ps shows clearly that the wavepacket can be described as a superposition of the corresponding ED and EA states shown in **Figure 4.3**. This demonstrates that the electron transfer is proceeding gradually from the ED state to the EA state, rather than through an instantaneous hopping. The MD trajectory is calculated separately and cannot change in response to the QED to produce electron-nuclear resonance<sup>57</sup>. Nevertheless, quantum dynamics always selects the fastest channel to the product making the electronic system acting as a phonon antenna. That is, it selects the vibrational mode that is "just right" to facilitate coherent transfer<sup>60</sup>. This validates the coupled quantum classical approach of treating the nonadiabatic transfer between two states through periodic instantaneous rearrangement of nuclear positions in the diabatic AO base, while performing the propagation in the adiabatic MO base.

#### **4.4. CONCLUSIONS**

In summary, efficient ET in T-AM-TiO<sub>2</sub> is driven by a strong coupling between the electron dynamics and specific nuclear vibrational modes. It has been shown that a slow rotation of the bridge with respect to the antenna opens a preferential channel for ET by changing the localization of the donor and acceptor states. When the channel is open, the charge can move across the bridge from the electron donor to the acceptor state driven by the bridge vibrational modes that induce periodic crossing of energy levels and nonadiabatic coupling of these two states.

These results underline the importance of including the nuclear dynamics for a proper description of the electron injection. In addition, I have verified the rectification properties of the AM bridge as part of a chromophore for a DSSC. The vibrational modes identified through the analysis of the correlation between nuclear and electron dynamics provide possible strategies for accelerating the electron injection process for high efficiency by *e.g.* structural modifications of the AM bridge to constrain rotations of the Ph1 ring.

#### 4.5. REFERENCES

- (1) O'Regan, B.; Grätzel, M. A Low-Cost, High-Efficiency Solar Cell Based on Dye-Sensitized Colloidal TiO<sub>2</sub> Films. *Nature* **1991**, *353* (6346), 737–740.
- (2) Duncan, W. R.; Craig, C. F.; Prezhdo, O. V. Time-Domain Ab Initio Study of Charge Relaxation and Recombination in Dye-Sensitized TiO<sub>2</sub>. *J. Am. Chem. Soc.* **2007**, *129* (27), 8528–8543.
- (3) Listorti, A.; O'Regan, B.; Durrant, J. R. Electron Transfer Dynamics in Dye-Sensitized Solar Cells. *Chem. Mater.* **2011**, *23* (15), 3381–3399.
- (4) Nattestad, A.; Mozer, A. J.; Fischer, M. K. R.; Cheng, Y.-B.; Mishra, A.; Bäuerle, P.; Bach, U. Highly Efficient Photocathodes for Dye-Sensitized Tandem Solar Cells. *Nat. Mater.* **2010**, *9* (1), 31–35.
- (5) Zhou, N.; Lin, H.; Lou, S. J.; Yu, X.; Guo, P.; Manley, E. F.; Loser, S.; Hartnett, P.; Huang, H.; Wasielewski, M. R.; et al. Morphology-Performance Relationships in High-Efficiency All-Polymer Solar Cells. *Adv. Energy Mater.* **2014**, *4* (3), n/a – n/a.
- (6) Hagfeldt, A.; Boschloo, G.; Sun, L.; Kloo, L.; Pettersson, H. Dye-Sensitized Solar Cells. *Chem. Rev.* **2010**, *110* (11), 6595–6663.
- (7) Monti, A.; de Groot, H. J. M.; Buda, F. In-Silico Design of a Donor–Antenna–Acceptor Supramolecular Complex for Photoinduced Charge Separation. *J. Phys. Chem. C* **2014**, *118* (29), 15600–15609.
- (8) Haid, S.; Marszalek, M.; Mishra, A.; Wielopolski, M.; Teuscher, J.; Moser, J.-E.; Humphry-Baker, R.; Zakeeruddin, S. M.; Grätzel, M.; Bäuerle, P. Significant Improvement of Dye-Sensitized Solar Cell Performance by Small Structural Modification in  $\Pi$ -Conjugated Donor–Acceptor Dyes. *Adv. Funct. Mater.* **2012**, *22* (6), 1291–1302.
- (9) Caprasecca, S.; Mennucci, B. Excitation Energy Transfer in Donor-Bridge-Acceptor Systems: A Combined Quantum-Mechanical/Classical Analysis of the Role of the Bridge and the Solvent. *J. Phys. Chem. A* **2014**, *118* (33), 6484–6491.
- (10) Ma, W.; Jiao, Y.; Meng, S. Modeling Charge Recombination in Dye-Sensitized Solar Cells Using First-Principles Electron Dynamics: Effects of Structural Modification. *Phys. Chem. Chem. Phys.* **2013**, *15* (40), 17187–17194.
- (11) Ambrosio, F.; Martsinovich, N.; Troisi, A. What Is the Best Anchoring Group for a Dye in a Dye-Sensitized Solar Cell? *J. Phys. Chem. Lett.* **2012**, *3* (11), 1531–1535.
- (12) Koops, S. E.; O'Regan, B. C.; Barnes, P. R. F.; Durrant, J. R. Parameters Influencing the Efficiency of Electron Injection in Dye-Sensitized Solar Cells. *J. Am. Chem. Soc.* **2009**, *131* (13), 4808–4818.
- (13) Meng, S.; Kaxiras, E. Electron and Hole Dynamics in Dye-Sensitized Solar Cells: Influencing Factors and Systematic Trends. *Nano Lett.* **2010**, *10* (4), 1238–1247.
- (14) De Angelis, F. Modeling Materials and Processes in Hybrid/Organic Photovoltaics: From Dye-Sensitized to Perovskite Solar Cells. *Acc. Chem. Res.* **2014**, *47* (11), 3349–3360.
- (15) De Angelis, F.; Fantacci, S.; Selloni, A.; Nazeeruddin, M. K.; Grätzel, M. Time-Dependent Density Functional Theory Investigations on the Excited States of Ru(II)-Dye-Sensitized TiO<sub>2</sub> Nanoparticles: The Role of Sensitizer Protonation. *J. Am. Chem. Soc.* **2007**, *129* (46), 14156–14157.
- (16) Nieto-Pescador, J.; Abraham, B.; Gundlach, L. Photoinduced Ultrafast Heterogeneous Electron Transfer at Molecule–Semiconductor Interfaces. *J. Phys. Chem. Lett.* **2014**, *5* (20), 3498–3507.
- (17) Zhu, H.; Yang, Y.; Hyeon-Deuk, K.; Califano, M.; Song, N.; Wang, Y.; Zhang, W.; Prezhdo, O. V.; Lian, T. Auger-Assisted Electron Transfer from Photoexcited Semiconductor Quantum Dots. *Nano Lett.* **2014**, *14* (3), 1263–1269.

- (18) Akimov, A. V.; Neukirch, A. J.; Prezhdo, O. V. Theoretical Insights into Photoinduced Charge Transfer and Catalysis at Oxide Interfaces. *Chem. Rev.* **2013**, *113* (6), 4496–4565.
- (19) Akimov, A. V.; Prezhdo, O. V. Nonadiabatic Dynamics of Charge Transfer and Singlet Fission at the Pentacene/C60 Interface. *J. Am. Chem. Soc.* **2014**.
- (20) Tafen, D. N.; Long, R.; Prezhdo, O. V. Dimensionality of Nanoscale TiO<sub>2</sub> Determines the Mechanism of Photoinduced Electron Injection from a CdSe Nanoparticle. *Nano Lett.* **2014**, *14* (4), 1790–1796.
- (21) Long, R.; English, N. J.; Prezhdo, O. V. Minimizing Electron–Hole Recombination on TiO<sub>2</sub> Sensitized with PbSe Quantum Dots: Time-Domain Ab Initio Analysis. *J. Phys. Chem. Lett.* **2014**, 2941–2946.
- (22) Aviram, A.; Ratner, M. A. Molecular Rectifiers. *Chem. Phys. Lett.* **1974**, *29* (2), 277–283.
- (23) Ding, W.; Negre, C. F. A.; Vogt, L.; Batista, V. S. Single Molecule Rectification Induced by the Asymmetry of a Single Frontier Orbital. *J. Chem. Theory Comput.* **2014**, *10* (8), 3393–3400.
- (24) Ding, W.; Negre, C. F. A.; Palma, J. L.; Durrell, A. C.; Allen, L. J.; Young, K. J.; Milot, R. L.; Schmuttenmaer, C. A.; Brudvig, G. W.; Crabtree, R. H.; et al. Linker Rectifiers for Covalent Attachment of Transition-Metal Catalysts to Metal-Oxide Surfaces. *ChemPhysChem* **2014**, *15* (6), 1138–1147.
- (25) Fleury, L.; Zumbusch, A.; Orrit, M.; Brown, R.; Bernard, J. Spectral Diffusion and Individual Two-Level Systems Probed by Fluorescence of Single Terrylene Molecules in a Polyethylene Matrix. *J. Lumin.* **1993**, *56* (1–6), 15–28.
- (26) Harms, G. S.; Irngartinger, T.; Reiss, D.; Renn, A.; Wild, U. P. Fluorescence Lifetimes of Terrylene in Solid Matrices. *Chem. Phys. Lett.* **1999**, *313* (3–4), 533–538.
- (27) Edvinsson, T.; Pschirer, N.; Schöneboom, J.; Eickemeyer, F.; Boschloo, G.; Hagfeldt, A. Photoinduced Electron Transfer from a Terrylene Dye to TiO<sub>2</sub>: Quantification of Band Edge Shift Effects. *Chem. Phys.* **2009**, *357* (1–3), 124–131.
- (28) Andrea Rozzi, C.; Maria Falke, S.; Spallanzani, N.; Rubio, A.; Molinari, E.; Brida, D.; Maiuri, M.; Cerullo, G.; Schramm, H.; Christoffers, J.; et al. Quantum Coherence Controls the Charge Separation in a Prototypical Artificial Light-Harvesting System. *Nat. Commun.* **2013**, *4*, 1602.
- (29) Chapman, C. T.; Liang, W.; Li, X. Ultrafast Coherent Electron–Hole Separation Dynamics in a Fullerene Derivative. *J. Phys. Chem. Lett.* **2011**, *2* (10), 1189–1192.
- (30) Falke, S. M.; Rozzi, C. A.; Brida, D.; Maiuri, M.; Amato, M.; Sommer, E.; Sio, A. D.; Rubio, A.; Cerullo, G.; Molinari, E.; et al. Coherent Ultrafast Charge Transfer in an Organic Photovoltaic Blend. *Science* **2014**, *344* (6187), 1001–1005.
- (31) Romero, E.; Augulis, R.; Novoderezhkin, V. I.; Ferretti, M.; Thieme, J.; Zigmantas, D.; van Grondelle, R. Quantum Coherence in Photosynthesis for Efficient Solar-Energy Conversion. *Nat. Phys.* **2014**, *10* (9), 676–682.
- (32) Chin, A. W.; Prior, J.; Rosenbach, R.; Caycedo-Soler, F.; Huelga, S. F.; Plenio, M. B. The Role of Non-Equilibrium Vibrational Structures in Electronic Coherence and Recoherence in Pigment-Protein Complexes. *Nat. Phys.* **2013**, *9* (2), 113–118.
- (33) Fuller, F. D.; Pan, J.; Gelzinis, A.; Butkus, V.; Senlik, S. S.; Wilcox, D. E.; Yocum, C. F.; Valkunas, L.; Abramavicius, D.; Ogilvie, J. P. Vibronic Coherence in Oxygenic Photosynthesis. *Nat. Chem.* **2014**, *6* (8), 706–711.
- (34) Hayes, D.; Griffin, G. B.; Engel, G. S. Engineering Coherence among Excited States in Synthetic Heterodimer Systems. *Science* **2013**, *340* (6139), 1431–1434.
- (35) Hoffmann, R. An Extended Hückel Theory. I. Hydrocarbons. *J. Chem. Phys.* **1963**, *39* (6), 1397–1412.

- (36) Ammeter, J. H.; Buergi, H. B.; Thibeault, J. C.; Hoffmann, R. Counterintuitive Orbital Mixing in Semiempirical and Ab Initio Molecular Orbital Calculations. *J. Am. Chem. Soc.* **1978**, *100* (12), 3686–3692.
- (37) Wolfsberg, M.; Helmholz, L. The Spectra and Electronic Structure of the Tetrahedral Ions  $\text{MnO}_4^-$ ,  $\text{CrO}_4^{2-}$ , and  $\text{ClO}_4^-$ . *J. Chem. Phys.* **1952**, *20* (5), 837–843.
- (38) Santiago Alvarez. Table of Parameters for Extended Huckel Calculations, Collected by Santiago Alvarez, Universitat de Barcelona (1995). **1995**.
- (39) Becke, A. D. Density-functional Thermochemistry. III. The Role of Exact Exchange. *J. Chem. Phys.* **1993**, *98* (7), 5648–5652.
- (40) M. J. Frisch, G. W. Trucks, H. B. Schlegel, G. E. Scuseria, M. A. Robb, J. R. Cheeseman, G. Scalmani, V. Barone, B. Mennucci, G. A. Petersson, et al. *Gaussian 09, Revision D.01*; Gaussian, Inc.: Wallingford CT, 2009.
- (41) Ding, W.-L.; Wang, D.-M.; Geng, Z.-Y.; Zhao, X.-L.; Yan, Y.-F. Molecular Engineering of Indoline-Based D–A– $\pi$ –A Organic Sensitizers toward High Efficiency Performance from First-Principles Calculations. *J. Phys. Chem. C* **2013**, *117* (34), 17382–17398.
- (42) Hoff, D. A.; da Silva, R.; Rego, L. G. C. Coupled Electron–Hole Quantum Dynamics on D– $\pi$ –A Dye-Sensitized  $\text{TiO}_2$  Semiconductors. *J. Phys. Chem. C* **2012**, *116* (40), 21169–21178.
- (43) Rego, L. G. C.; Hames, B. C.; Mazon, K. T.; Joswig, J.-O. Intramolecular Polarization Induces Electron–Hole Charge Separation in Light-Harvesting Molecular Triads. *J. Phys. Chem. C* **2014**, *118* (1), 126–134.
- (44) Hoff, D. A.; Silva, R.; Rego, L. G. C. Subpicosecond Dynamics of Metal-to-Ligand Charge-Transfer Excited States in Solvated  $[\text{Ru}(\text{bpy})_3]^{2+}$  Complexes. *J. Phys. Chem. C* **2011**, *115* (31), 15617–15626.
- (45) Da Silva, R.; Hoff, D. A.; Rego, L. G. C. Coupled Quantum-Classical Method for Long Range Charge Transfer: Relevance of the Nuclear Motion to the Quantum Electron Dynamics. *J. Phys. Condens. Matter* **2015**, *27* (13), 134206.
- (46) CPMD, [Http://www.cpmc.org/](http://www.cpmc.org/), Copyright IBM Corp 1990-2008, Copyright MPI für Festkörperforschung Stuttgart 1997-2001.
- (47) Lin, I.-C.; Coutinho-Neto, M. D.; Felsenheimer, C.; von Lilienfeld, O. A.; Tavernelli, I.; Rothlisberger, U. Library of Dispersion-Corrected Atom-Centered Potentials for Generalized Gradient Approximation Functionals: Elements H, C, N, O, He, Ne, Ar, and Kr. *Phys. Rev. B* **2007**, *75* (20), 205131.
- (48) Becke, A. D. Density-Functional Exchange-Energy Approximation with Correct Asymptotic Behavior. *Phys. Rev. A* **1988**, *38* (6), 3098–3100.
- (49) Lee, C.; Yang, W.; Parr, R. G. Development of the Colle-Salvetti Correlation-Energy Formula into a Functional of the Electron Density. *Phys. Rev. B* **1988**, *37* (2), 785–789.
- (50) Abuabara, S. G.; Rego, L. G. C.; Batista, V. S. Influence of Thermal Fluctuations on Interfacial Electron Transfer in Functionalized  $\text{TiO}_2$  Semiconductors. *J. Am. Chem. Soc.* **2005**, *127* (51), 18234–18242.
- (51) Te Velde, G.; Bickelhaupt, F. M.; Baerends, E. J.; Fonseca Guerra, C.; van Gisbergen, S. J. A.; Snijders, J. G.; Ziegler, T. Chemistry with ADF. *J. Comput. Chem.* **2001**, *22* (9), 931–967.
- (52) Fan, L.; Ziegler, T. Application of Density Functional Theory to Infrared Absorption Intensity Calculations on Main Group Molecules. *J. Chem. Phys.* **1992**, *96* (12), 9005–9012.
- (53) Fan, L.; Ziegler, T. Nonlocal Density Functional Theory as a Practical Tool in Calculations on Transition States and Activation Energies. Applications to Elementary Reaction Steps in Organic Chemistry. *J. Am. Chem. Soc.* **1992**, *114* (27), 10890–10897.
- (54) Olbrich, C.; Strümpfer, J.; Schulten, K.; Kleinekathöfer, U. Theory and Simulation of the Environmental Effects on FMO Electronic Transitions. *J. Phys. Chem. Lett.* **2011**, *2* (14), 1771–1776.



- (55) Akimov, A. V.; Prezhdo, O. V. Persistent Electronic Coherence Despite Rapid Loss of Electron–Nuclear Correlation. *J. Phys. Chem. Lett.* **2013**, *4* (22), 3857–3864.
- (56) Jiao, Y.; Ding, Z.; Meng, S. Atomistic Mechanism of Charge Separation upon Photoexcitation at the Dye–semiconductor Interface for Photovoltaic Applications. *Phys. Chem. Chem. Phys.* **2011**, *13* (29), 13196–13201.
- (57) Eisenmayer, T. J.; Buda, F. Real-Time Simulations of Photoinduced Coherent Charge Transfer and Proton-Coupled Electron Transfer. *ChemPhysChem* **2014**, *15* (15), 3258–3263.
- (58) Eisenmayer, T. J.; Lasave, J. A.; Monti, A.; de Groot, H. J. M.; Buda, F. Proton Displacements Coupled to Primary Electron Transfer in the Rhodobacter Sphaeroides Reaction Center. *J. Phys. Chem. B* **2013**, *117* (38), 11162–11168.
- (59) Eisenmayer, T. J.; de Groot, H. J. M.; van de Wetering, E.; Neugebauer, J.; Buda, F. Mechanism and Reaction Coordinate of Directional Charge Separation in Bacterial Reaction Centers. *J. Phys. Chem. Lett.* **2012**, *3* (6), 694–697.
- (60) Purchase, R.L.; de Groot, H.J.M. Biosolar Cells: Global Artificial Photosynthesis Needs Responsive Matrices with Quantum Coherent Kinetic Control for High Yield. *Interface Focus* **2015**, *5*.

## 4.6. APPENDIX

### 4.6.1. Test on geometrical relaxation in the excited state

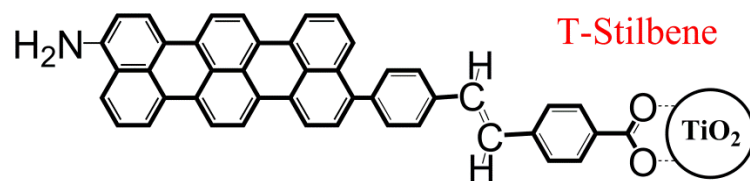
An additional test has been performed to check the effects of the photo-excitation on the T-AM chromophore. Using the Gaussian 09 software package<sup>40</sup>, together with the CAM-B3LYP exchange-correlation functional and the cc-pVDZ basis set, we have optimized the geometry of the T-AM dye in the first excited state, which has predominant HOMO-LUMO character. The optimized geometry in the excited state shows only small changes in the C-C bond lengths of the terrylene antenna with maximum displacements of  $\sim 0.03$  Å. Given that the LUMO is highly localized on the terrylene, it is not surprising that these geometrical changes are only observed in the terrylene molecule and do not propagate on the AM bridge whose geometry is essentially not modified by the excitation. These results strongly suggest that the dynamics of the AM bridge will be hardly affected by the excitation localized on the terrylene antenna, giving further justification to the use of a ground state dynamics for the study of the electron injection.

### 4.6.2. Test on T-Stilbene-TiO<sub>2</sub>

The survival probability reported in **Figure 4.2** and **Figure 4.4** shows a constant decrease of the electron wavepacket localized on T-AM. This indicates the absence of large charge fluctuations from the semiconductor back onto the donor state of the dye. To verify that this is due to the AM bridge rectification properties, following the same computational procedure used for T-AM-TiO<sub>2</sub>, we perform an EQD simulation for a system in which we substitute the AM bridge with the fully conjugated (E)-stilbene molecule (**Figure A4.1a**). Due to its conjugation this system is not expected to show rectification<sup>23</sup>.

The results for T-Stilbene-TiO<sub>2</sub> are reported in **Figure A4.1b**. Due to the fully conjugated nature of (E)-stilbene, the initial wavepacket is localized not only on the terrylene but on the entire dye. In this case the electron injection is extremely fast, due to the strong coupling with the semiconductor conduction band states (see **Figure A4.1b**, first 20 fs). However, along the dynamics the survival probability for T-Stilbene-TiO<sub>2</sub> shows strong fluctuations associated with electron density fluctuation between the antenna and the semiconductor (see insets in **Figure A4.1b**). This is a strong indication that the T-Stilbene-TiO<sub>2</sub> system does not show rectification capability in contrast to the results shown for T-AM-TiO<sub>2</sub>.

(a)



(b)

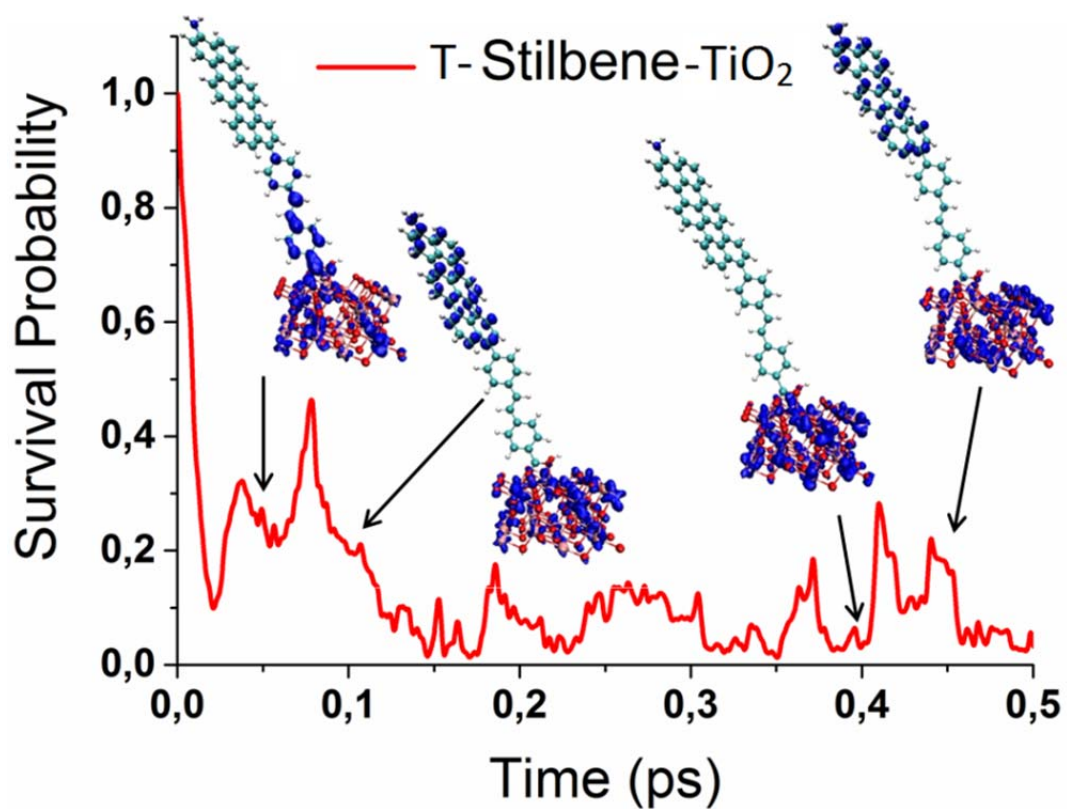


**Figure A4.1.** (a) Schematic representation of the T-Stilbene dye. (b) SP profile of the EQD simulation of T-Stilbene-TiO<sub>2</sub> along an MD trajectory. The insets show the wavepacket localization at different snapshots along the EQD.

# Fully Atomistic Simulation of Solvent Mediated Proton-Coupled Electron Transfer Assisting Photodriven Catalytic Water Oxidation

### **5.0. ABSTRACT**

---

*Solar-driven water splitting is a key reaction step in a photoelectrochemical cell for solar to fuel conversion. By means of quantum-classical dynamics simulations, we investigate a photoanode consisting of a  $\text{TiO}_2$  substrate functionalized with a supramolecular complex combining the visible light absorption and catalytic functions. This complex consists of a fully organic naphthalene-diimide (NDI) derivative chromophore covalently bound to a mononuclear Ru-based water oxidation catalyst. Photo-excitation induces electron injection from the NDI to the semiconductor substrate in a sub-picosecond time scale. Following the electron injection, proton-coupled electron transfer is observed to lead to the formation of the first catalytic intermediate in the water oxidation cycle. The analysis of the free-energy profile shows that this process is thermodynamically favorable and has a very small activation barrier. The inclusion of an explicit water environment in the simulations is crucial to provide the hydrogen bond network for the proton transfer as well as the necessary thermal fluctuations that stabilize the final state.*

---

## 5.1. INTRODUCTION

Direct conversion of solar energy into storable chemical fuel is a promising strategy in the path towards sustainable energy sources<sup>1,2</sup>. As explained in chapter 1, natural systems perform this task by converting water molecules into O<sub>2</sub> and high-energy-density molecular compounds. They apply molecular machineries, which are complex, but without redundancy in the biological context of the membrane and the cell. The design of artificial solar energy conversion devices therefore aims at applying essential fundamental principles governing natural photosynthesis, while aiming for dedicated solar to fuel conversions, which allows using a much simpler structure.

A prototypical artificial photosynthesis device combines the functions of light harvesting, charge separation and catalysis, and it is able to produce high-energy-density fuel using sunlight and water as power source and feedstock.

Its structure comprises subunits dedicated to each function. Light harvesting is achieved through one or more chromophores able to absorb light within the visible range. Charge separation is induced by donor and acceptor molecules coupled to the dye. Catalytic water oxidation and hydrogen evolution are performed respectively at the anode and cathode by the specialized WOC and HEC.

These units should be combined in such a way that, upon photoexcitation of the chromophore, a stable charge separated state is obtained by transferring the photoinduced hole and the excited electron to the WOC and the HEC respectively, thereby driving the two catalysts. This spatial separation is essential to reduce the recombination rate between the two charges, which allows the catalysis to take place at the two electrodes.

The overall efficiency of the cell depends on the balance between the kinetics and the thermodynamics of these processes. Therefore, acquiring a fundamental understanding of the individual electron transfer processes ultimately driving the activation of the catalytic centers is essential for the design and the optimization of solar fuel cells.

In chapter 3 and chapter 4 of this thesis it has been investigated how to control through design principles the processes of photoinduced charge separation and electron injection, while avoiding charge recombination.

In this chapter we intend to investigate the cooperation between the formation of a photoinduced charge separated state and the process of catalytic water oxidation, which takes place at the photoanode of a solar fuel cell.

The first example of a photoanode for water oxidation was presented by Mallouk and coworkers who functionalized a TiO<sub>2</sub> semiconductor with catalytic IrO<sub>2</sub> nanoparticle through a Ru-based dye<sup>3</sup>. After this work, several systems have been

proposed employing metal oxide nanoparticles as water oxidation catalysts. Less common are paradigms of photoanodes functionalized with molecular catalysts<sup>4</sup>.

Two main strategies exist for coupling the WOC, the chromophore and the electron accepting semiconductor into a photoanode<sup>1,2,4-6</sup>. The first is the so called co-absorption strategy, in which both the catalyst and the chromophore functionalize the surface of the semiconductor<sup>7-9</sup>. This method allows to change the chromophore to catalyst ratio and broaden the absorption range by employing different molecular dyes. However, it has been suggested that this strategy may be affected by low electron injection yield due to interferences between the catalyst and the sensitizer<sup>5,10</sup>.

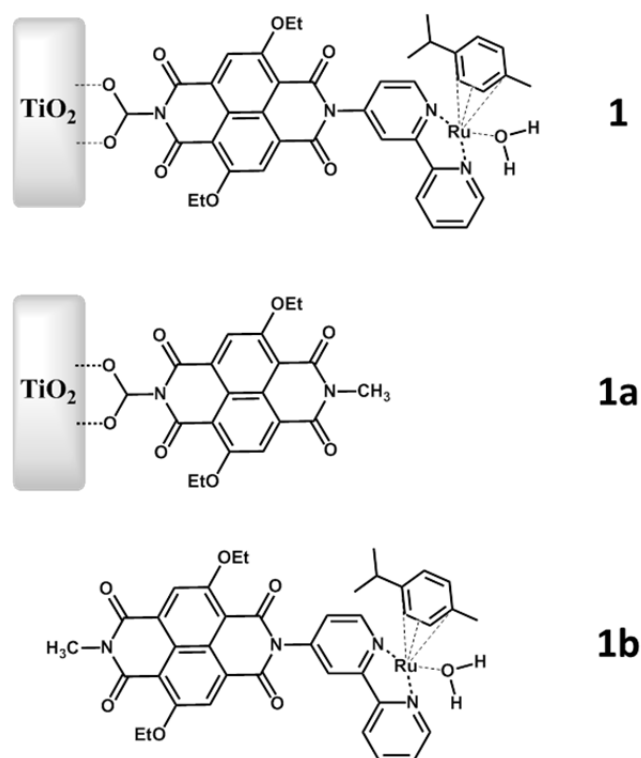
The second approach<sup>11-13</sup>, which is followed also in this chapter, is to covalently bind the chromophore to both a semiconductor surface acting as electron acceptor on one side, and to a WOC acting as electron donor on the other. The advantage of this type of design is that it increases the control over the directionality of the charge transfer. In addition, a chromophore bridge between the WOC and the semiconductor should reduce the probability of charge recombination upon formation of the charge separated state by increasing the distance between positive and negative charges.

The structure of the photoanode **1** investigated here is presented in **Scheme 5.1**.

TiO<sub>2</sub> is by far the most common choice for the semiconductor to be used in a photosynthesis device, due to its excellent stability in combination with a high density of states of its conduction band, which allows for rapid electron injection rates<sup>14</sup>. Therefore, it appears a valid choice for the electron acceptor unit in system **1**.

The WOC considered in this system is the mono Ru-complex [(cy)Ru<sup>II</sup>bpy(H<sub>2</sub>O)]<sup>2+</sup>. This catalyst has been already theoretically and experimentally investigated in the literature, and its catalytic cycle has been suggested to proceed through four consecutive proton-coupled electron transfer (PCET) steps<sup>15,16</sup>.

The chromophore molecule NDI<sub>1</sub> is used to bridge the catalyst and the semiconductor. This is the same chromophore already applied as antenna module in the systems proposed in chapter 3.



**Scheme 5.1.** Schematic representation of the proposed photoanode (**1**) including the acceptor-semiconductor (TiO<sub>2</sub>), the molecular chromophore NDI<sub>1</sub>, and the Ru-based water oxidation catalyst; (**1a**) chromophore-semiconductor subsystem employed for the photoinduced electron injection simulation; (**1b**) chromophore-catalyst subsystem used in the simulation of the first water oxidation catalytic step.

This choice is based on several considerations regarding system **1**:

- As explained in chapter 3, this antenna strongly absorbs within the visible light range at  $\sim 500$  nm promoting a unique HOMO $\rightarrow$ LUMO transition well localized on the molecule naphthalene core.
- The LUMO energy level reported for this molecule is  $\sim -3.8$  eV<sup>17</sup> (*vs.* vacuum). This feature allows for the formation of a charge separated state through the electron injection into the TiO<sub>2</sub> conduction band ( $\sim -4$  eV *vs.* vacuum), with marginal energy losses due to thermal relaxation.
- The experimental value of the ground state oxidation potential for NDI<sub>1</sub><sup>17</sup> is comparable to that reported for the [(cy)Ru<sup>II</sup>bpy(H<sub>2</sub>O)]<sup>2+</sup> water oxidation catalyst of  $\sim -6.2$  eV (*vs.* vacuum)<sup>16</sup>.

Due to the characteristics of the semiconductor, the antenna, and the catalyst complex combined in the design of photoanode **1**, the photoexcitation of the chromophore is expected to promote the formation of a charge separated state able to initiate the catalytic oxidation of water at the WOC.

These processes are studied by combining quantum-classical dynamics and *ab*

*initio* molecular dynamics (MD) simulations. Quantum-classical dynamic simulations of model system **1a** show ultrafast electron injection from the chromophore into the semiconductor, thus demonstrating that NDI<sub>1</sub> is a viable chromophore choice in the design of a dye-sensitized solar fuel cell.

*Ab initio* constrained MD simulations of the oxidized model **1b** surrounded by explicit water solvent, reveal that a PCET mechanism is responsible for the first catalytic water oxidation step triggered by the photoinduced electron injection. These simulations highlight how the oxidation of water and the reduction of NDI<sub>1</sub> occur in a concerted process. The progressive diffusion of one proton from the coordinated water molecule (see **Scheme 5.1, 1b**) to the solvent bulk, induces a simultaneous electron transfer from the catalyst to the antenna in a cooperative PCET mechanism. The low free energy barrier evaluated along this reaction path corresponds with an estimated rate constant on the sub-nanosecond scale.

## **5.2. METHODS AND COMPUTATIONAL DETAILS**

### **5.2.1. System 1a: preparation and electron quantum dynamics simulation**

The chromophore is prepared by functionalizing the NDI<sub>1</sub> with a carboxylic acid group on one of the amide functionalities. This group is used to anchor the dye onto the TiO<sub>2</sub> surface to form model **1a** shown in **scheme 5.1**.

The ground state geometry of the functionalized NDI<sub>1</sub> is optimized separately from the TiO<sub>2</sub> slab. The calculation is performed in vacuum with the ADF software package<sup>18,19</sup>. The optimization is done at the density functional theory (DFT) level employing the exchange-correlation functional BLYP<sup>20,21</sup> and the TZP Slater type basis set.

The optimized geometry is employed as the starting point for a ground state *ab initio* MD simulation using the CPMD code<sup>22</sup>. The system is brought to 300 K by applying the Nosé-Hoover thermostat and is evolved for 300 fs using a time step  $\delta t = 0.1$  fs, while constraining the atoms of the anchoring group in their initial positions for the whole simulation. This CPMD simulation is performed in vacuum using the pseudopotentials of reference<sup>23</sup> with a plane wave cut-off of 70 Rydberg and the BLYP<sup>21,24</sup> exchange correlation functional. This predetermined ground state MD trajectory is then used to study the electron quantum dynamics in system **1a** presenting a (TiO<sub>2</sub>)<sub>32</sub> slab. During the EQD simulation, the atomic positions of the semiconductor slab are kept fixed.

The photoinduced electron injection from the chromophore to the semiconductor is quantum mechanically described by using a tight-binding Hamiltonian based on the extended Hückel (EH) theory<sup>25,26</sup>. This method employs a basis set of atom-centered



Slater-type orbitals with atomic effective charges  $\zeta$ . The effective Hamiltonian matrix is parameterized in terms of the atomic Coulomb integrals  $H_{\nu\nu}$  and the Wolfsberg-Helmholtz parameters<sup>25,27</sup>  $k_{\nu\mu}$ . More details on the method and the parameterization procedure are discussed in section 2.7 and 4.2 of this thesis. For the parameterization of the atoms of NDI<sub>1</sub>, the experimental ground-state (-6.16 eV vs. vacuum) and excited state (-3.82 eV vs. vacuum) redox potentials reported by Sakai et al.<sup>17</sup> for this chromophore are taken as target values for the HOMO and LUMO energies. A 6 eV downshift is applied to account for the extended Hückel results for the semiconductor surface (see section 4.2.1).

To model the TiO<sub>2</sub> surface, an orthorhombic supercell with lattice parameters  $a=10.239$  Å,  $b=15.137$  Å and  $c=40$  Å is used. The cell contains a two layers anatase slab (TiO<sub>2</sub>)<sub>32</sub> functionalized with the NDI<sub>1</sub> chromophore, and it is repeated along the [101] and the [010] directions by applying periodic boundary conditions. For the atoms of the semiconductor, standard EH parameters<sup>28</sup> are employed without any further modification.

The electron quantum dynamics simulation is performed by evolving the electronic wavepacket, initialized as the LUMO of the NDI<sub>1</sub> chromophore, under the influence of the classical nuclear Car-Parrinello dynamics obtained beforehand. The evolution of the initial reactant excitonic state into the final charge transfer product state is carried on following the AO/MO time propagation method<sup>29</sup> described in section 4.2.2.

### **5.2.2. System 1b: preparation, characterization and constrained *ab initio* MD**

Using the ADF software package, the ground state geometry of system **1b** is initially optimized at the DFT level making use of the exchange-correlation functional OPBE<sup>30</sup> and the TZP basis set. The optimization is performed in an aqueous environment simulated with the continuous solvation model (COSMO<sup>31,32</sup>) implemented in ADF.

The choice of the OPBE functional is dictated by the presence of the Ruthenium atom in system **1b**. In fact, the OPBE exchange-correlation functional has been shown to provide accurate descriptions of several complexes bearing transition metals<sup>33-35</sup>, among which the [(cy)Ru<sup>II</sup>bpy(H<sub>2</sub>O)]<sup>2+</sup> catalyst<sup>15</sup> used in system **1b**. Moreover the same computational setting closely reproduces the experimental ground state oxidation potential for NDI<sub>1</sub> within the **1b** complex, calculated using the  $\Delta$ SCF approach. In fact, the ground-state oxidation potential calculated for the dyad **1b** is -6.05 eV vs. vacuum. As it will be reported in section 5.3.3, the removal of one electron from **1b** results in oxidizing the NDI<sub>1</sub> subunit.

To verify that  $\text{NDI}_1$  acts as the only visible light antenna unit in system **1b**, the dyad absorption spectrum is computed with the TD-DFT method. The TD-DFT calculations are performed using the ADF software package at the B3LYP<sup>36</sup>/TZP level of theory, in an aqueous solution simulated with the COSMO model. The choice of the exchange correlation functional is justified by the results presented in section 3.3.1, where B3LYP has been shown to accurately reproduce the experimental optical properties of the  $\text{NDI}_1$  molecule.

To investigate whether the photoinduced oxidation of the dyad can initiate the catalytic process of water oxidation, *ab initio* MD simulations are performed for the singly oxidized form of the catalyst-antenna complex with the CPMD program. The structure of the dyad optimized with the ADF software at the OPBE/TZP level is used as starting point for the *ab initio* MD. To obtain a realistic description of the PCET reaction, the solvent is explicitly introduced in the calculation. An orthorhombic box of dimensions 25x17.6x14.5 Å<sup>3</sup> is used, containing the **1b** solute and 162 water molecules. Both the solvent and the solute molecules are treated at the same quantum-mechanical level employing the OPBE exchange correlation functional and the dispersion-corrected atom-centered pseudopotential of reference<sup>28</sup>. Periodic boundary conditions are applied together with a plane wave cut off of 70 Rydbergs.

Using a time step  $\delta t = 0.1$  fs, the system is equilibrated for  $\sim 3$  ps at room temperature by applying the Nosé-Hoover thermostat.

Maintaining the same computational set up, constrained MD<sup>37,38</sup> simulations are performed to obtain an estimate for the free-energy variation along the PCET occurring during the first step of catalytic water oxidation. The distance between one of the protons of the water molecule coordinated to the Ru atom, and the oxygen of one of the adjacent solvating water molecules is chosen as the constrained reaction coordinate. Five points within the range 1.4-0.98 Å are considered for this coordinate. For each constraint value, the system is evolved until the associated average Lagrange multiplier, corresponding to the gradient of the free energy associated to the reaction coordinate, is equilibrated. The free energy variation of the whole process is then obtained via thermodynamic integration.

### 5.3. RESULTS AND DISCUSSION

In this section the results are organized as follows: in section 5.3.1 the optical properties of the  $[(\text{cy})\text{Ru}^{\text{II}}\text{bpy}(\text{H}_2\text{O})]^{2+}$ -NDI<sub>1</sub> dyad (**1b**) are presented, showing that the only excitation observed in the visible light range involves molecular orbitals localized solely on the chromophore unit. This result justifies the choice of the model **1a** for the study of the electron injection presented in section 5.3.2. The tight-binding nonadiabatic dynamics shows that the excited electron is injected in the semiconductor within a few hundred fs. Thus, in section 5.3.3 the first water oxidation step is studied under the assumption that model **1b** has been oxidized through the photoinduced electron injection in TiO<sub>2</sub>.

#### 5.3.1. TDDFT characterization of the electronic excitations of the dye-catalyst complex and Molecular Orbitals localization

In order to evaluate to what extent the optical properties of the NDI<sub>1</sub> antenna may be altered by the covalent coupling to the water oxidation catalyst  $[(\text{cy})\text{Ru}^{\text{II}}\text{bpy}(\text{H}_2\text{O})]^{2+}$ , a time-dependent DFT calculation is performed for the dyad **1b** in a water environment, simulated through a continuous solvent model.

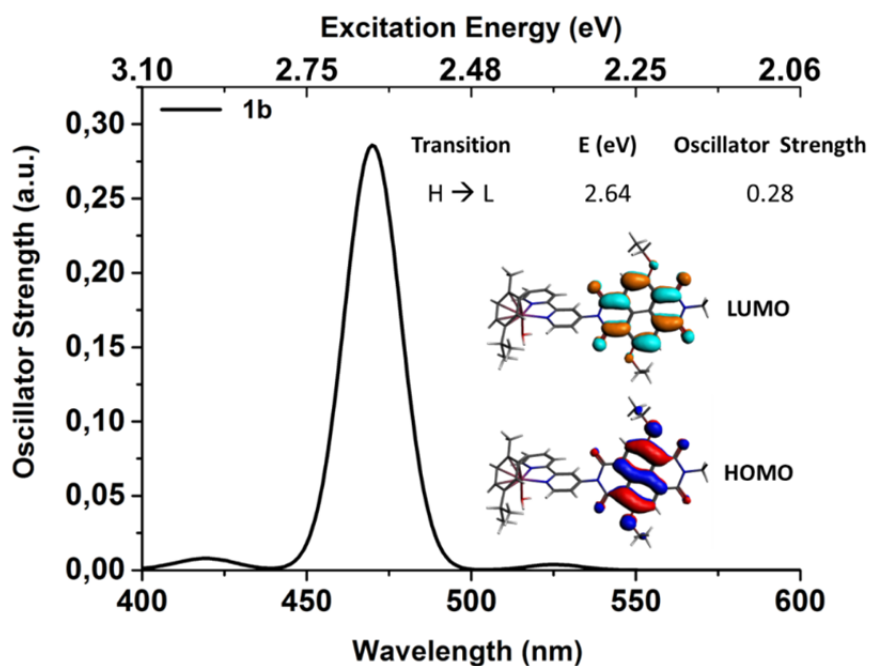


**Figure 5.1.** Optical absorption spectrum of system **1b**, computed at the B3LYP/TZP level of theory. The water solvent is included through the continuum solvation model (COSMO). The inset shows the localization of the HOMO (H) and LUMO (L), which are the only orbitals involved in the optical transition at 2.64 eV.

The results in **Figure 5.1** show the presence of a single dominant peak within the visible light range at  $\sim 470$  nm. The analysis of this electronic excitation reveals that it is associated to the HOMO to LUMO transition, localized on the chromophore dyad

subunit (see inset **Figure 5.1**).

The computed optical absorption energy compares well to the experimental results for the monomer chromophore  $\text{NDI}_1$  already discussed in chapter 3<sup>39</sup>. This result provides enough evidence that the formation of the dyad does not significantly alter the optical properties of the chromophore.

As a consequence of the nature and localization of the HOMO and the LUMO, the Ru-based catalyst is not expected to play a significant role in the formation of the sensitizer excitonic state. Consequently, in the next section we investigate the process of photoinduced electron injection into the semiconductor without explicitly including the catalyst in the definition of the electron donor (see model **1a**).

### 5.3.2. Photoinduced electron injection dynamics in the dye- $\text{TiO}_2$ model

The photoinduced electron injection dynamics is performed using the same tight-binding extended Hückel approach described in chapter 4. The optimization of the extended Hückel parameters is performed by taking the experimental oxidation potentials for the  $\text{NDI}_1$  (**Table 3.2**) as target values for the HOMO and LUMO energies of the dye.

As already explained in section 4.2.1, the conduction band edge obtained with the unmodified extended Hückel parameters is shifted down by about 6 eV with respect to experimental value ( $\sim -4$  eV)<sup>40,11,41,42</sup>. Therefore, for consistency, the target values for the chromophore orbital energies have to be as well downshifted by the same amount. The density of states (DOS) has been computed for the entire system **1a**. **Figure 5.2** shows only the region of the DOS corresponding to the semiconductor conduction band.

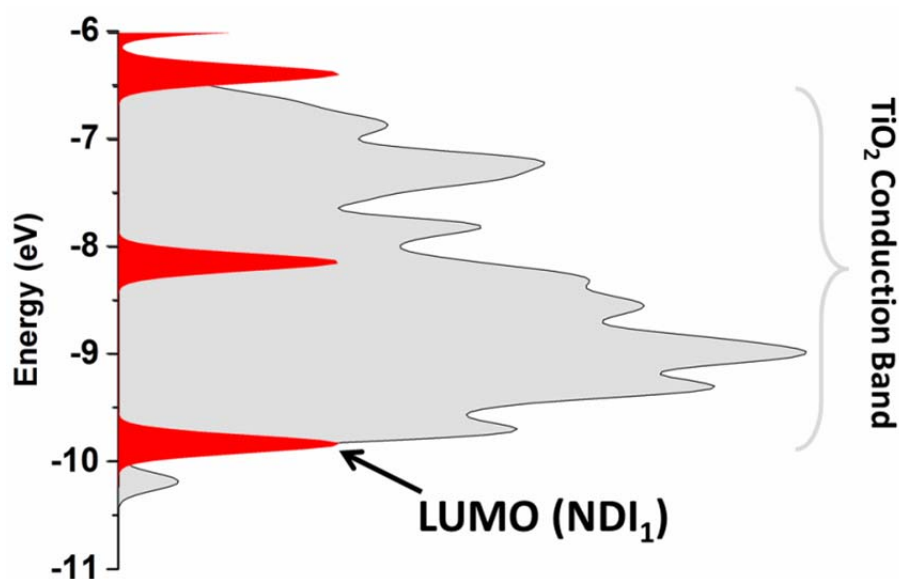


**Figure 5.2.** Density of the unoccupied states of system **1a** projected onto the  $\text{TiO}_2$  conduction band (in grey) and on the  $\text{NDI}_1$  chromophore (in red). To account for the extended Hückel results for the semiconductor surface, the zero of the energy scale has been shifted downwards by 6 eV (see section 4.2.1).

It appears clearly that the chromophore presents a LUMO energy very close to the conduction band edge of  $\text{TiO}_2$ . This confirms that the  $\text{NDI}_1$  is an appropriate choice as sensitizer, since it is able to inject into the  $\text{TiO}_2$  conduction band, while limiting to a minimum the loss of the potential induced by the photexcitation in the form of heat.

The initial wavepacket for the quantum electron dynamics is initialized as the LUMO of the chromophore. This is done to simulate the instantaneous photoexcitation of  $\text{NDI}_1$ . This initial wavepacket state is reported in **Figure 5.3** (inset (a)).

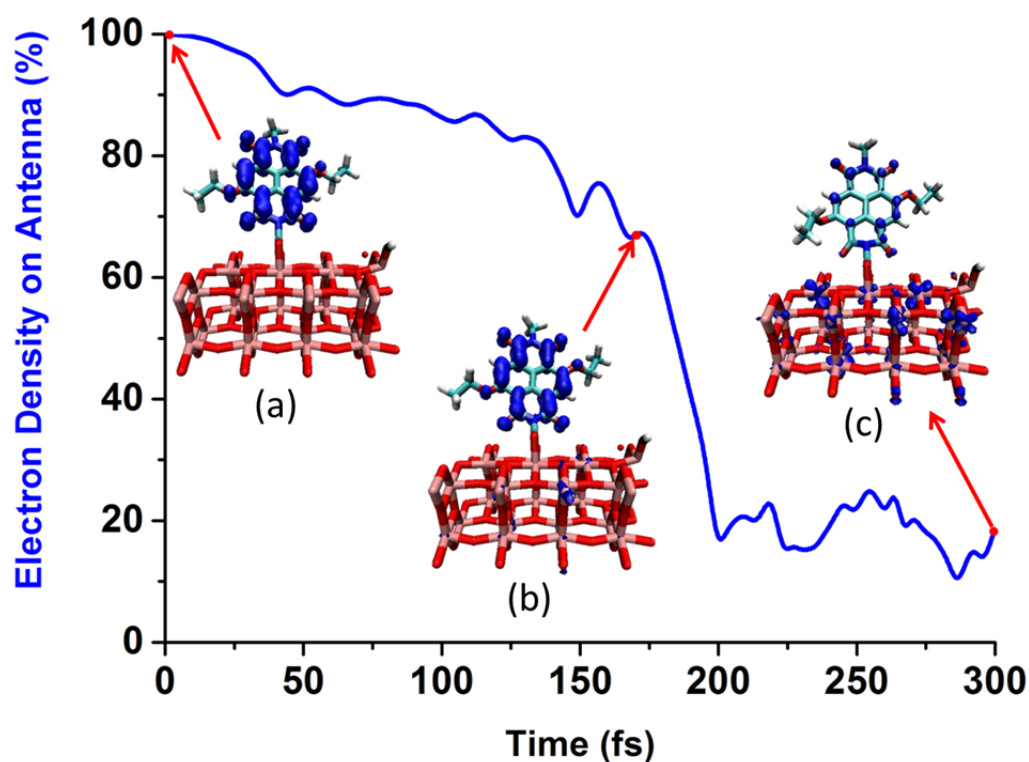


**Figure 5.3.** Electron injection profile obtained through the time-dependent population analysis of the wavepacket projected only over the  $\text{NDI}_1$  antenna (blue line). The insets show the distribution of the total wavepacket after initialization (a), and along the dynamics trajectory (b and c).

The results of the electron quantum dynamics coupled to the motion of the nuclei treated classically show a fast electron injection that is almost completed after only 200 fs.

Inset (c) in **Figure 5.3**, shows that after 300 fs the wavepacket is almost completely localized onto the  $\text{TiO}_2$  surface. Overall these results provide evidences that system **1** can undergo ultrafast electron injection, upon photoexcitation of its  $\text{NDI}_1$  antenna unit.

The analysis of the nuclear trajectory shows interesting correlations between the electron injection dynamics and specific nuclear motions at the interface between the

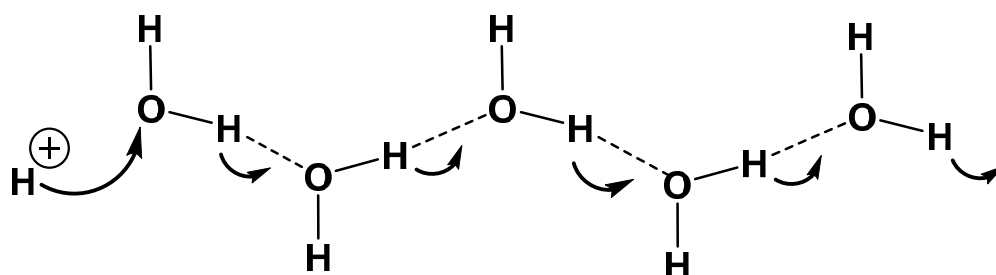
dye and the  $\text{TiO}_2$  surface. In particular, as reported in **Figure A5.1** in the appendix, it emerges that the electron injection is driven by a large distortion of the planarity of the ring defined by the naphthalene core and the amide group at the semiconductor interface (see **Figure A5.1**, top panel). Additionally, the shortening of the distance between that amide and the anchoring group (see C-N in **Figure A5.1**, lower panel) correlates with the electron injection profile. This suggests that this motion plays a role in enhancing the electron coupling between the electron donor state on the  $\text{NDI}_1$  and the acceptor state on the semiconductor.

In general, water oxidation catalysis is known to occur over time scales orders of magnitude larger than the sub-picosecond electron injection process observed here for system **1a**. Therefore, it is reasonable to assume that, upon photoexcitation, the electron injection will occur before the catalytic water oxidation can take place, leaving the antenna-catalyst dyad in an oxidized state.

In the next section, it is investigated whether this oxidized state of the antenna-catalyst dyad (**1b**) is able to drive the first catalytic step of water oxidation.

### 5.3.3. First PCET catalytic water oxidation step

*Ab initio* molecular dynamics simulations are performed for the oxidized dyad model **1b** in an explicit water solvent treated at the same DFT quantum-mechanical level. Since we are interested in describing the proton-coupled electron transfer step, it is essential to provide an appropriate quantum description of the water molecules in the system. It is indeed well known that proton diffusion in liquid water is a complex process that involves covalent bond breaking and formation within the hydrogen bonding network. This process is often referred to as the Grotthuss mechanism (see **Scheme 5.2**). Here a water chain is depicted with a proton lattice that is incommensurate with the underlying  $\text{H}_2\text{O}$  molecular chain due to the presence of an 'excess' proton. Such a defect diffuses through the hydrogen bond network of water molecules by barrier-less motion, involving switching of hydrogen bonds by formation and cleavage of covalent bonds<sup>43-46</sup>. It is named after Theodor Grotthuss who in 1806 first proposed this mechanism in its theory for water conductivity<sup>47</sup>.



**Scheme 5.2.** Schematic representation of the Grotthuss proton transfer mechanism in water.

After equilibration of the dyad in its initial stable intermediate at near-neutral pH  $[(\text{cy})\text{Ru}^{\text{II}}\text{bpy}(\text{H}_2\text{O})]^{2+}\text{-NDI}_1$ , the instantaneous photoexcitation and ultrafast electron injection are mimicked by removing an electron from the simulation box. The removal of one electron induces a change in the multiplicity of the system from a singlet to a doublet state. Therefore, we can monitor the localization of the photoinduced hole by tracing the total spin density of the system along the *ab initio* MD trajectory.

The oxidized system is then equilibrated at room temperature for about 3 ps. At the beginning of this trajectory we clearly see the hole being localized on the  $\text{NDI}_1$ . The analysis of this MD trajectory shows that the water molecule w1, coordinated to the Ru center (see **Figure 5.4**), forms strong hydrogen bonds with nearby solvent molecules. In **Figure 5.4**, the  $\text{H}(\text{w1})\text{-O}(\text{w1})$  and the  $\text{H}(\text{w1})\cdots\text{O}(\text{w2})$  distances along the MD trajectory are reported. It is possible to observe spontaneous attempts of proton transfer from w1 to the neighbor water molecule w2 after about 1.6 ps and 1.9 ps, when these two distances become almost equal. During these attempts the  $\text{H}(\text{w1})\cdots\text{O}(\text{w2})$  distance is reduced from an average value of  $\sim 1.7 \text{ \AA}$  to  $\sim 1.2 \text{ \AA}$ , while the  $\text{H}(\text{w1})\text{-O}(\text{w1})$  distance increases from  $\sim 0.96 \text{ \AA}$  to the same value of  $\sim 1.2 \text{ \AA}$ . When the two distances are almost equivalent, the  $\text{H}(\text{w1})$  proton can be considered as part of both w1 and w2 (see inset in **Figure 5.4**).

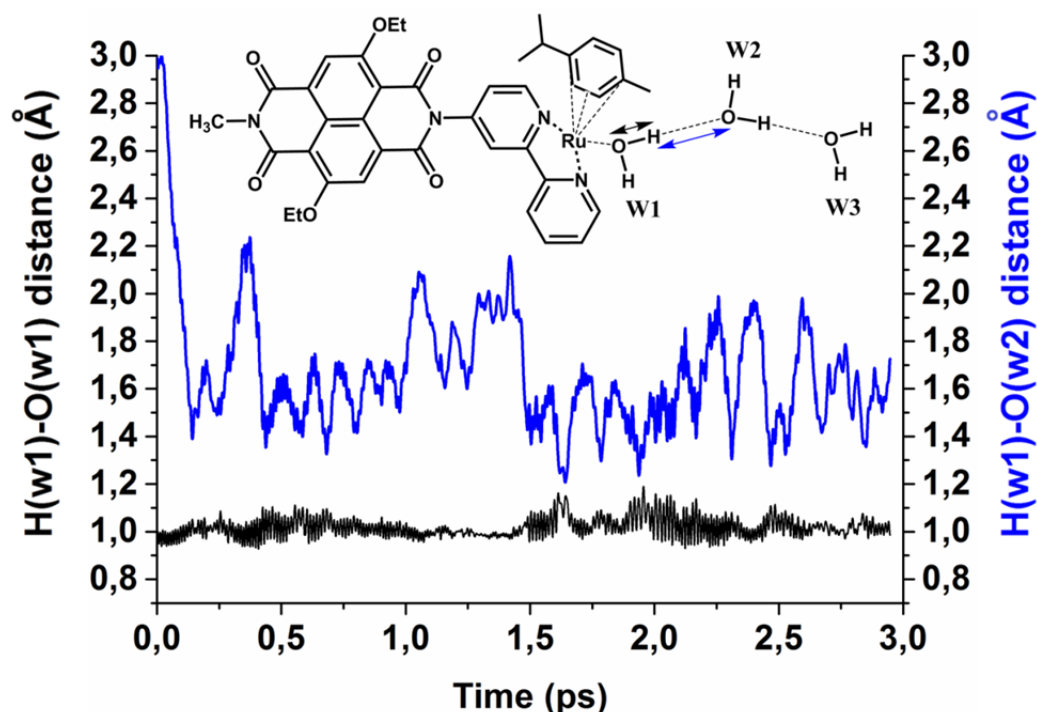
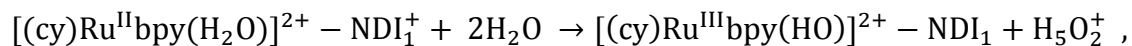


**Figure 5.4.** Time evolution of the geometrical parameters  $\text{H}(\text{w1})\cdots\text{O}(\text{w2})$  (blue line) and  $\text{H}(\text{w1})\text{-O}(\text{w1})$  (black line) along the unconstrained *ab initio* MD for the explicitly solvated  $[(\text{cy})\text{Ru}^{\text{II}}\text{bpy}(\text{H}_2\text{O})]^{2+}\text{-NDI}_1^+$  complex. The inset schematically shows the dyad structure together with a few water molecules along the hydrogen bonding network.

These events may be indicative of the initial attempts of the system to undergo the first PCET step in the water oxidation catalytic cycle of  $[(\text{cy})\text{Ru}^{\text{II}}\text{bpy}(\text{H}_2\text{O})]^{2+}$ .

This first expected PCET step corresponds to the transition



where an electron has been transferred from the Ru-catalyst to the  $\text{NDI}_1$  antenna, and at the same time a proton has been released into the solvent. In the reaction above the water solvent has been arbitrarily represented by only two water molecules for convenience.

This PCET process may in fact occur on a time scale longer than the few ps investigated in our *ab initio* MD simulations. The solvent has in fact to reorganize in response to changes in both the electron and the proton localization to stabilize the final product, and this may occur within a longer time frame<sup>48,49</sup>.

Therefore a rare event simulation technique is more appropriate to describe this process. A constrained MD approach is then considered using the  $\text{H}(\text{w}1)\cdots\text{O}(\text{w}2)$  distance as the reaction coordinate driving the transition between the reactant and the product state. The results of the different constrained MD trajectories are collected in **Figure 5.5**, together with the unconstrained MD of the product state obtained at the end of the constrained simulations.



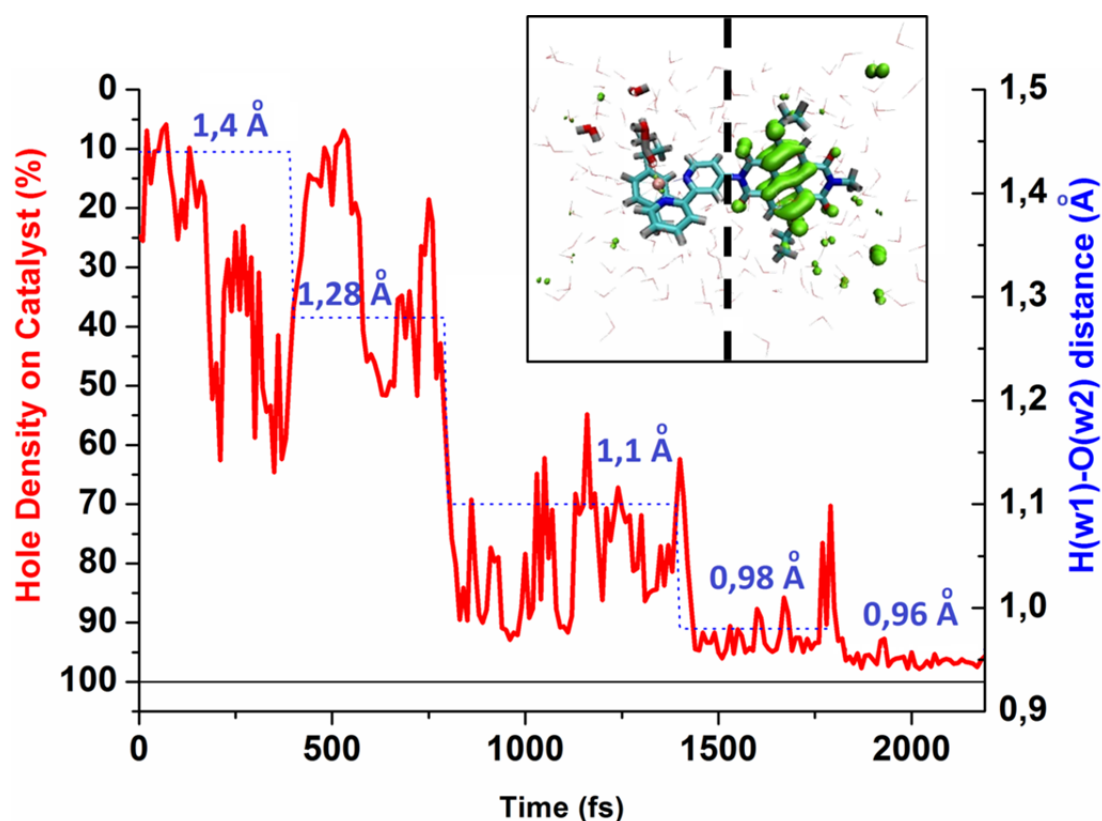


**Figure 5.5.** Percentage of the hole density (red line) visualized by integrating the spin density in the region of the simulation box occupied by the catalyst on the left hand side of the dashed black line in the inset. The blue dotted line indicates the value of the corresponding constrained H(w1)···O(w2) reaction coordinate. The results reported after 1800 fs correspond to an unconstrained simulation of the final product in which the average H(w1)–O(w2) distance is 0.96 Å. The inset shows a snapshot from the beginning of the trajectory corresponding to a constraint value of 1.4 Å, where the spin density is almost completely localized over the NDI<sub>1</sub>.

During these trajectories, the total spin density of the system is used to visualize the localization of the unpaired electron. To obtain a quantitative estimate of the spin density repartition between catalyst and antenna units, the total spin density is integrated over the volume of the half of the simulation box that contains the catalyst subunit. This corresponds to the left hand side of the inset in **Figure 5.5**.

This analysis provides information on how the electron transfer process between NDI<sub>1</sub><sup>+</sup> and [(cy)Ru<sup>II</sup>bpy(H<sub>2</sub>O)]<sup>2+</sup> is coupled to variations in the reaction coordinate H(w1)···O(w2).

For constrained distances between 1.4–1.28 Å, the hole density localized on the catalyst fluctuates around an average value of ~35%. This behaviour is observed also during the unconstrained MD performed before applying the constraints and can be rationalized based on the similar oxidation potentials for NDI<sub>1</sub> and the Ru-catalyst.

Instead, the shortening of the H(w1)⋯O(w2) distance to 1.1 Å induces a stronger localization of ~80% of the spin density on the catalyst.

A further displacement of the H(w1) proton towards the water molecule w2 reduces the charge fluctuations, leading to the stabilization of the Ru<sup>III</sup>-catalyst oxidation state. The stability of this state is confirmed by removing the constraint: the MD results after 1800 fs, indeed show that the unpaired electron remains localized over the Ru<sup>III</sup>-catalyst and the newly formed H(w1)–O(w2) bond oscillates around an equilibrium distance of 0.96 Å.

**Figure 5.6** shows how the localization of the spin density gradually changes from the NDI<sub>1</sub> to the Ru-catalyst along the trajectory, in response to the shortening of the H(w1)⋯O(w2) distance. It is worth noticing that in some snapshots the spin density is partially localized on a few water molecules. This is attributed to an induced polarization effect due to the electron transfer.

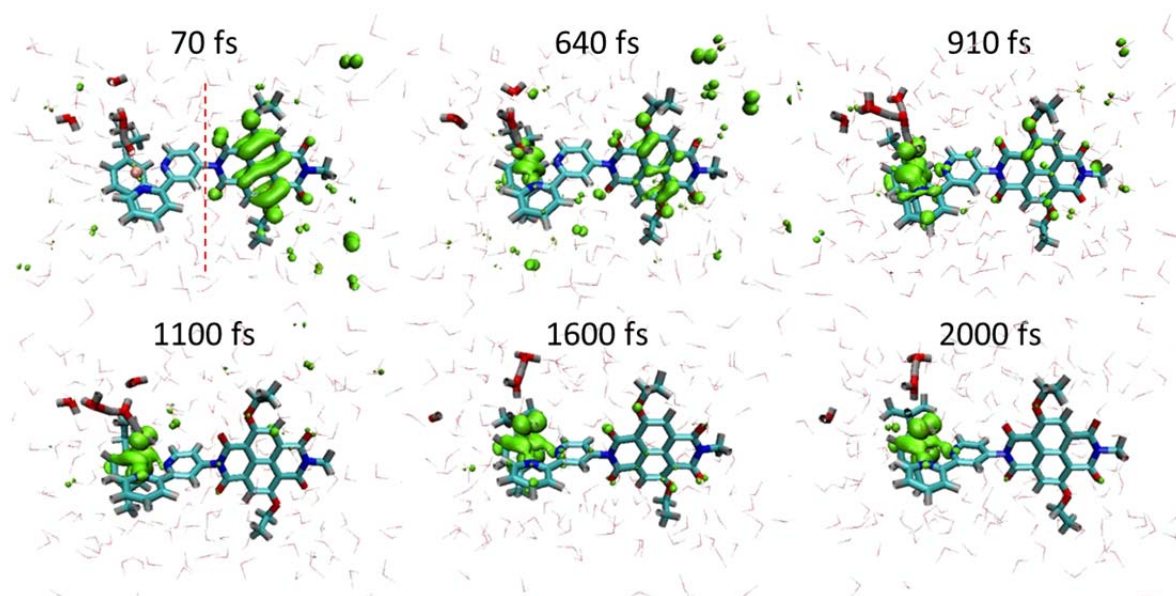


**Figure 5.6.** Spin density localization (in green) along the MD trajectory discussed in **Figure 5.5**. The labels refer to the time at which the snapshot has been taken along the collected trajectory.

The analysis of the collected trajectories shows that the response of the solvent water molecules to the variation in the H(w1)⋯O(w2) distance does not only stabilize the spin density localization on the ruthenium catalyst, but it also creates the conditions for the diffusion of one proton from the w1 molecule into the water bulk. These results provide strong evidence that the concomitant antenna reduction and first catalytic water oxidation step represent a cooperative event and proceed via a PCET process. It should be underlined that this process proceeds along an adiabatic PES as in the adiabatic limit of Marcus theory of equation 1.4.

This is clearly visible by comparing **Figure 5.6** and **Figure 5.7**.

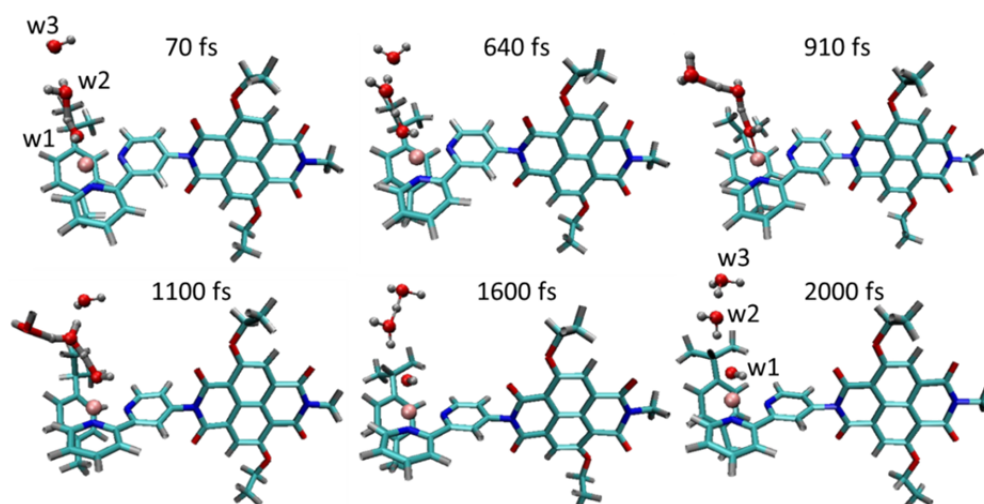


**Figure 5.7.** Mechanism of proton diffusion from the w1 molecule into the solvent bulk driven by H(w1)–O(w2) distance modifications along the collected trajectory.

In **Figure 5.7**, it is possible to observe how the hydrogen bonding network around the proton accepting molecule w2 rearranges in response to the progressive formation of the H(w1)–O(w2) bond.

During the constrained dynamics at 1.1 Å it is observed that the H(w1)–O(w1) distance oscillates around an average value of  $\sim 1.5$  Å, making H(w1) effectively part of w2. As a response to accepting this proton, w2 tends to share another one of its protons with one adjacent water molecule (see snapshot at 910 fs and 1100 fs). This is the first step in the Grotthuss like proton diffusion mechanism.

In the last two snapshots at 1600 fs and 2000 fs, shown in **Figure 5.7**, it is observed how the excess proton is now solvated as part of a complex cation such as  $\text{H}_5\text{O}_2^+$ , while the catalyst assumes the  $[(\text{cy})\text{Ru}^{\text{III}}\text{bpy}(\text{HO})]^{2+}$  coordination form. By continuing the unconstrained simulation, it is observed that the proton further diffuses throughout the solvent via the same mechanism, generating mixing entropy.

This  $[(\text{cy})\text{Ru}^{\text{III}}\text{bpy}(\text{HO})]^{2+}$ -NDI<sub>1</sub> product state reached for system **1b** represents the first photoinduced catalytic intermediate in the Ru-catalyst water oxidation cycle<sup>15</sup>. The PCET nature of this process is also in agreement with the suggested catalytic mechanism<sup>15</sup>.

An estimate of the free-energy profile along the reaction coordinate can be extracted from the constrained dynamics. The mean force values together with the polynomial fit used for this analysis are reported in the appendix (**Figure A5.2**). The free-energy profile obtained is shown in **Figure 5.8**, which is in line with an adiabatic process with a modest energy barrier.

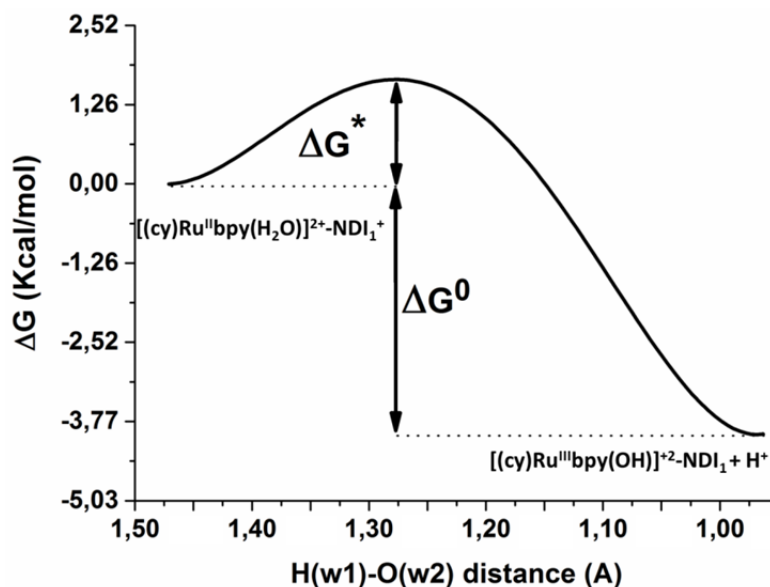


**Figure 5.8** Free-energy profile along the reaction coordinate  $H(w1)-O(w2)$  for the first water oxidation catalytic step in system **1b**.  $\Delta G^*$  represents the height of the reaction energy barrier, while  $\Delta G^0$  is the reaction driving force for the transition between the reactant (left hand side) and the product (right hand side) state.

The activation energy barrier  $\Delta G^*$  is estimated to be  $\sim 1.7$  kcal mol<sup>-1</sup>, which is equivalent to  $\sim 3$   $k_B T$  for  $T=300$  K. The maximum of the free-energy profile corresponds to a  $H(w1)\cdots O(w2)$  distance of 1.28 Å. Interestingly,  $H(w1)\cdots O(w2)$  distances comparable to 1.28 Å are explored by the reactant approximately every 1.5 ps during the unconstrained MD simulation (see **Figure 5.4**).

These results suggest that the PCET step can occur on a time scale of  $\sim 20$  ps at room temperature. This value is calculated using the Arrhenius equation with the estimated  $\Delta G^*$  (equation 1.4 in section 1.4.1). The pre-exponential factor is associated with the rate of proton transfer attempts between  $w1$  and  $w2$  observed in the unconstrained trajectory for the reactant. In addition, from the free energy profile we predict that this PCET step is exothermic by  $\sim 4$  kcal mol<sup>-1</sup> (see **Figure 5.8**).

#### 5.4. CONCLUSIONS

In this chapter, various computational tools are used to investigate the light-driven catalytic properties of the proposed photanode **1** for solar water splitting.

Quantum-classical simulations based on the Extended Hückel semi-empirical Hamiltonian demonstrate that the chosen NDI<sub>1</sub> chromophore can achieve sub-picosecond photoinduced electron injection when covalently coupled to a TiO<sub>2</sub> surface and photoexcited with visible light of ~470 nm. The photoinduced oxidation of the chromophore drives the first water oxidation step at the covalently bound [(cy)Ru<sup>II</sup>bpy(H<sub>2</sub>O)]<sup>2+</sup> catalyst.

DFT based *ab initio* MD simulations for the explicitly solvated dyad **1b** show that the Ru-catalyst is able to reduce the oxidized antenna to its neutral state. Moreover, it is observed that the electron transfer towards the antenna unit takes place in concomitance with the diffusion of one proton from the metal-coordinated water to the solvent bulk. These results confirm the PCET nature of the first catalytic water splitting step. These simulations also underline the primary role played by the solvent molecules in promoting the process of photoinduced water oxidation through the creation of an hydrogen bonding network necessary for the charge stabilization and the proton diffusion. A very low activation barrier of ~1.7 kcal mol<sup>-1</sup> is calculated, suggesting that this first catalytic step can proceed adiabatically at room temperature in a sub-nanosecond time scale.

These results represents one of the few examples of photoanode for water oxidation involving a molecular catalyst<sup>50</sup> and provide a better understanding of the dynamics by which PCET can drive the photoinduced catalytic water oxidation process.

**5.5. REFERENCES**

- (1) Gust, D.; Moore, T. A.; Moore, A. L. Solar Fuels via Artificial Photosynthesis. *Acc. Chem. Res.* **2009**, *42* (12), 1890–1898.
- (2) Tachibana, Y.; Vayssieres, L.; Durrant, J. R. Artificial Photosynthesis for Solar Water-Splitting. *Nat Photon* **2012**, *6* (8), 511–518.
- (3) Youngblood, W. J.; Lee, S.-H. A.; Kobayashi, Y.; Hernandez-Pagan, E. A.; Hoertz, P. G.; Moore, T. A.; Moore, A. L.; Gust, D.; Mallouk, T. E. Photoassisted Overall Water Splitting in a Visible Light-Absorbing Dye-Sensitized Photoelectrochemical Cell. *J. Am. Chem. Soc.* **2009**, *131* (3), 926–927.
- (4) Yu, Z.; Li, F.; Sun, L. Recent Advances in Dye-Sensitized Photoelectrochemical Cells for Solar Hydrogen Production Based on Molecular Components. *Energy Environ. Sci.* **2015**, *8* (3), 760–775.
- (5) Young, K. J.; Martini, L. A.; Milot, R. L.; Snoeberger III, R. C.; Batista, V. S.; Schmuttenmaer, C. A.; Crabtree, R. H.; Brudvig, G. W. Light-Driven Water Oxidation for Solar Fuels. *Coordination Chemistry Reviews* **2012**, *256* (21–22), 2503–2520.
- (6) Kärkäs, M. D.; Verho, O.; Johnston, E. V.; Åkermark, B. Artificial Photosynthesis: Molecular Systems for Catalytic Water Oxidation. *Chem. Rev.* **2014**, *114* (24), 11863–12001.
- (7) Swierk, J. R.; McCool, N. S.; Mallouk, T. E. Dynamics of Electron Recombination and Transport in Water-Splitting Dye-Sensitized Photoanodes. *J. Phys. Chem. C* **2015**.
- (8) Zhao, Y.; Swierk, J. R.; Megiatto, J. D.; Sherman, B.; Youngblood, W. J.; Qin, D.; Lentz, D. M.; Moore, A. L.; Moore, T. A.; Gust, D.; et al. Improving the Efficiency of Water Splitting in Dye-Sensitized Solar Cells by Using a Biomimetic Electron Transfer Mediator. *PNAS* **2012**, *109* (39), 15612–15616.
- (9) Ding, X.; Gao, Y.; Zhang, L.; Yu, Z.; Liu, J.; Sun, L. Visible Light-Driven Water Splitting in Photoelectrochemical Cells with Supramolecular Catalysts on Photoanodes. *ACS Catal.* **2014**, *4* (7), 2347–2350.
- (10) Moore, G. F.; Blakemore, J. D.; Milot, R. L.; Hull, J. F.; Song, H.; Cai, L.; Schmuttenmaer, C. A.; Crabtree, R. H.; Brudvig, G. W. A Visible Light Water-Splitting Cell with a Photoanode Formed by Codeposition of a High-Potential Porphyrin and an Iridium Water-Oxidation Catalyst. *Energy Environ. Sci.* **2011**, *4* (7), 2389–2392.
- (11) Pastore, M.; De Angelis, F. First-Principles Modeling of a Dye-Sensitized TiO<sub>2</sub>/IrO<sub>2</sub> Photoanode for Water Oxidation. *J. Am. Chem. Soc.* **2015**, *137* (17), 5798–5809.
- (12) Vagnini, M. T.; Smeigh, A. L.; Blakemore, J. D.; Eaton, S. W.; Schley, N. D.; D'Souza, F.; Crabtree, R. H.; Brudvig, G. W.; Co, D. T.; Wasielewski, M. R. Ultrafast Photodrivn Intramolecular Electron Transfer from an Iridium-Based Water-Oxidation Catalyst to Perylene Diimide Derivatives. *PNAS* **2012**, *109* (39), 15651–15656.
- (13) Ji, Z.; He, M.; Huang, Z.; Ozkan, U.; Wu, Y. Photostable P-Type Dye-Sensitized Photoelectrochemical Cells for Water Reduction. *J. Am. Chem. Soc.* **2013**, *135* (32), 11696–11699.
- (14) Ai, X.; Anderson, N. A.; Guo, J.; Lian, T. Electron Injection Dynamics of Ru Polypyridyl Complexes on SnO<sub>2</sub> Nanocrystalline Thin Films. *J. Phys. Chem. B* **2005**, *109* (15), 7088–7094.
- (15) Vallés-Pardo, J. L.; Guijt, M. C.; Iannuzzi, M.; Joya, K. S.; de Groot, H. J. M.; Buda, F. Ab Initio Molecular Dynamics Study of Water Oxidation Reaction Pathways in Mono-Ru Catalysts. *ChemPhysChem* **2012**, *13* (1), 140–146.
- (16) De Respinis, M.; Joya, K. S.; De Groot, H. J. M.; D'Souza, F.; Smith, W. A.; van de Krol, R.; Dam, B. Solar Water Splitting Combining a BiVO<sub>4</sub> Light

- Absorber with a Ru-Based Molecular Cocatalyst. *J. Phys. Chem. C* **2015**, *119* (13), 7275–7281.
- (17) Sakai, N.; Mareda, J.; Vauthey, E.; Matile, S. Core-Substituted Naphthalenediimides. *Chem. Commun.* **2010**, *46* (24), 4225–4237.
- (18) ADF: The ADF program for accurate density functional theory calculations of molecules <http://www.scm.com/ADF/> (accessed Mar 7, 2013).
- (19) Te Velde, G.; Bickelhaupt, F. M.; Baerends, E. J.; Fonseca Guerra, C.; van Gisbergen, S. J. A.; Snijders, J. G.; Ziegler, T. Chemistry with ADF. *Journal of Computational Chemistry* **2001**, *22* (9), 931–967.
- (20) Lee, C.; Yang, W.; Parr, R. G. Development of the Colle-Salvetti Correlation-Energy Formula into a Functional of the Electron Density. *Phys. Rev. B* **1988**, *37* (2), 785–789.
- (21) Becke, A. D. Density-Functional Exchange-Energy Approximation with Correct Asymptotic Behavior. *Phys. Rev. A* **1988**, *38* (6), 3098–3100.
- (22) CPMD, <Http://www.cpmc.org/>, Copyright IBM Corp 1990-2008, Copyright MPI für Festkörperforschung Stuttgart 1997-2001.
- (23) Lin, I.-C.; Coutinho-Neto, M. D.; Felsenheimer, C.; von Lilienfeld, O. A.; Tavernelli, I.; Rothlisberger, U. Library of Dispersion-Corrected Atom-Centered Potentials for Generalized Gradient Approximation Functionals: Elements H, C, N, O, He, Ne, Ar, and Kr. *Phys. Rev. B* **2007**, *75* (20), 205131.
- (24) Lee, C.; Yang, W.; Parr, R. G. Development of the Colle-Salvetti Correlation-Energy Formula into a Functional of the Electron Density. *Phys. Rev. B* **1988**, *37* (2), 785–789.
- (25) Ammeter, J. H.; Bürgi, H. B.; Thibeault, J. C.; Hoffmann, R. Counterintuitive Orbital Mixing in Semiempirical and Ab Initio Molecular Orbital Calculations. *J. Am. Chem. Soc.* **1978**, *100* (12), 3686–3692.
- (26) Hoffmann, R. An Extended Hückel Theory. I. Hydrocarbons. *The Journal of Chemical Physics* **1963**, *39* (6), 1397–1412.
- (27) Wolfsberg, M.; Helmholz, L. The Spectra and Electronic Structure of the Tetrahedral Ions  $\text{MnO}_4^-$ ,  $\text{CrO}_4^{2-}$ , and  $\text{ClO}_4^-$ . *The Journal of Chemical Physics* **1952**, *20* (5), 837–843.
- (28) Santiago Alvarez. Table of Parameters for Extended Huckel Calculations, Collected by Santiago Alvarez, Universitat de Barcelona (1995). **1995**.
- (29) Da Silva, R.; Hoff, D. A.; Rego, L. G. C. Coupled Quantum-Classical Method for Long Range Charge Transfer: Relevance of the Nuclear Motion to the Quantum Electron Dynamics. *Journal of Physics: Condensed Matter* **2015**, *27* (13), 134206.
- (30) Swart, M.; Ehlers, A. W.; Lammertsma, K. Performance of the OPBE Exchange-Correlation Functional. *Molecular Physics* **2004**, *102* (23-24), 2467–2474.
- (31) Klamt, A.; Jonas, V. Treatment of the Outlying Charge in Continuum Solvation Models. *The Journal of Chemical Physics* **1996**, *105* (22), 9972–9981.
- (32) Klamt, A. Conductor-like Screening Model for Real Solvents: A New Approach to the Quantitative Calculation of Solvation Phenomena. *J. Phys. Chem.* **1995**, *99* (7), 2224–2235.
- (33) Carvalho, A. T. P.; Swart, M. Electronic Structure Investigation and Parametrization of Biologically Relevant Iron–Sulfur Clusters. *J. Chem. Inf. Model.* **2014**, *54* (2), 613–620.
- (34) Groenhof, A. R.; Ehlers, A. W.; Lammertsma, K. Proton Assisted Oxygen–Oxygen Bond Splitting in Cytochrome P450. *J. Am. Chem. Soc.* **2007**, *129* (19), 6204–6209.
- (35) Conradie, J.; Ghosh, A. Electronic Structure of Trigonal-Planar Transition-Metal–Imido Complexes: Spin-State Energetics, Spin-Density Profiles, and the Remarkable Performance of the OLYP Functional. *J. Chem. Theory Comput.* **2007**, *3* (3), 689–702.
- (36) Stephens, P. J.; Devlin, F. J.; Chabalowski, C. F.; Frisch, M. J. Ab Initio Calculation of Vibrational Absorption and Circular Dichroism Spectra Using Density Functional Force Fields. *J. Phys. Chem.* **1994**, *98* (45), 11623–11627.

- (37) Sprik, M.; Ciccotti, G. Free Energy from Constrained Molecular Dynamics. *The Journal of Chemical Physics* **1998**, *109* (18), 7737–7744.
- (38) Otter, W. K. den; Briels, W. J. The Calculation of Free-Energy Differences by Constrained Molecular-Dynamics Simulations. *The Journal of Chemical Physics* **1998**, *109* (11), 4139–4146.
- (39) Kishore, R. S. K.; Kel, O.; Banerji, N.; Emery, D.; Bollot, G.; Mareda, J.; Gomez-Casado, A.; Jonkheijm, P.; Huskens, J.; Maroni, P.; et al. Ordered and Oriented Supramolecular N/p-Heterojunction Surface Architectures: Completion of the Primary Color Collection. *J. Am. Chem. Soc.* **2009**, *131* (31), 11106–11116.
- (40) Kavan, L.; Grätzel, M.; Gilbert, S. E.; Klemenz, C.; Scheel, H. J. Electrochemical and Photoelectrochemical Investigation of Single-Crystal Anatase. *J. Am. Chem. Soc.* **1996**, *118* (28), 6716–6723.
- (41) Mosconi, E.; Yum, J.-H.; Kessler, F.; Gómez García, C. J.; Zuccaccia, C.; Cinti, A.; Nazeeruddin, M. K.; Grätzel, M.; De Angelis, F. Cobalt Electrolyte/Dye Interactions in Dye-Sensitized Solar Cells: A Combined Computational and Experimental Study. *J. Am. Chem. Soc.* **2012**, *134* (47), 19438–19453.
- (42) De Angelis, F.; Fantacci, S.; Mosconi, E.; Nazeeruddin, M. K.; Grätzel, M. Absorption Spectra and Excited State Energy Levels of the N719 Dye on TiO<sub>2</sub> in Dye-Sensitized Solar Cell Models. *J. Phys. Chem. C* **2011**, *115* (17), 8825–8831.
- (43) Hassanali, A.; Giberti, F.; Cuny, J.; Kühne, T. D.; Parrinello, M. Proton Transfer through the Water Gossamer. *PNAS* **2013**, *110* (34), 13723–13728.
- (44) Marx, D.; Chandra, A.; Tuckerman, M. E. Aqueous Basic Solutions: Hydroxide Solvation, Structural Diffusion, and Comparison to the Hydrated Proton. *Chem. Rev.* **2010**, *110* (4), 2174–2216.
- (45) Agmon, N. The Grotthuss Mechanism. *Chemical Physics Letters* **1995**, *244* (5–6), 456–462.
- (46) Codorniu-Hernández, E.; Kusalik, P. G. Probing the Mechanisms of Proton Transfer in Liquid Water. *PNAS* **2013**, *110* (34), 13697–13698.
- (47) De Grotthuss, C. J. T. Memoir on the Decomposition of Water and of the Bodies That It Holds in Solution by Means of Galvanic Electricity. *Biochimica et Biophysica Acta (BBA) - Bioenergetics* **2006**, *1757* (8), 871–875.
- (48) Bosma, W. B.; Fried, L. E.; Mukamel, S. Simulation of the Intermolecular Vibrational Spectra of Liquid Water and Water Clusters. *The Journal of Chemical Physics* **1993**, *98* (6), 4413–4421.
- (49) Auer, B.; Soudackov, A. V.; Hammes-Schiffer, S. Nonadiabatic Dynamics of Photoinduced Proton-Coupled Electron Transfer: Comparison of Explicit and Implicit Solvent Simulations. *J. Phys. Chem. B* **2012**, *116* (26), 7695–7708.
- (50) Berardi, S.; Drouet, S.; Francàs, L.; Gimbert-Suriñach, C.; Guttentag, M.; Richmond, C.; Stoll, T.; Llobet, A. Molecular Artificial Photosynthesis. *Chem. Soc. Rev.* **2014**, *43* (22), 7501–7519.



## 5.6. APPENDIX

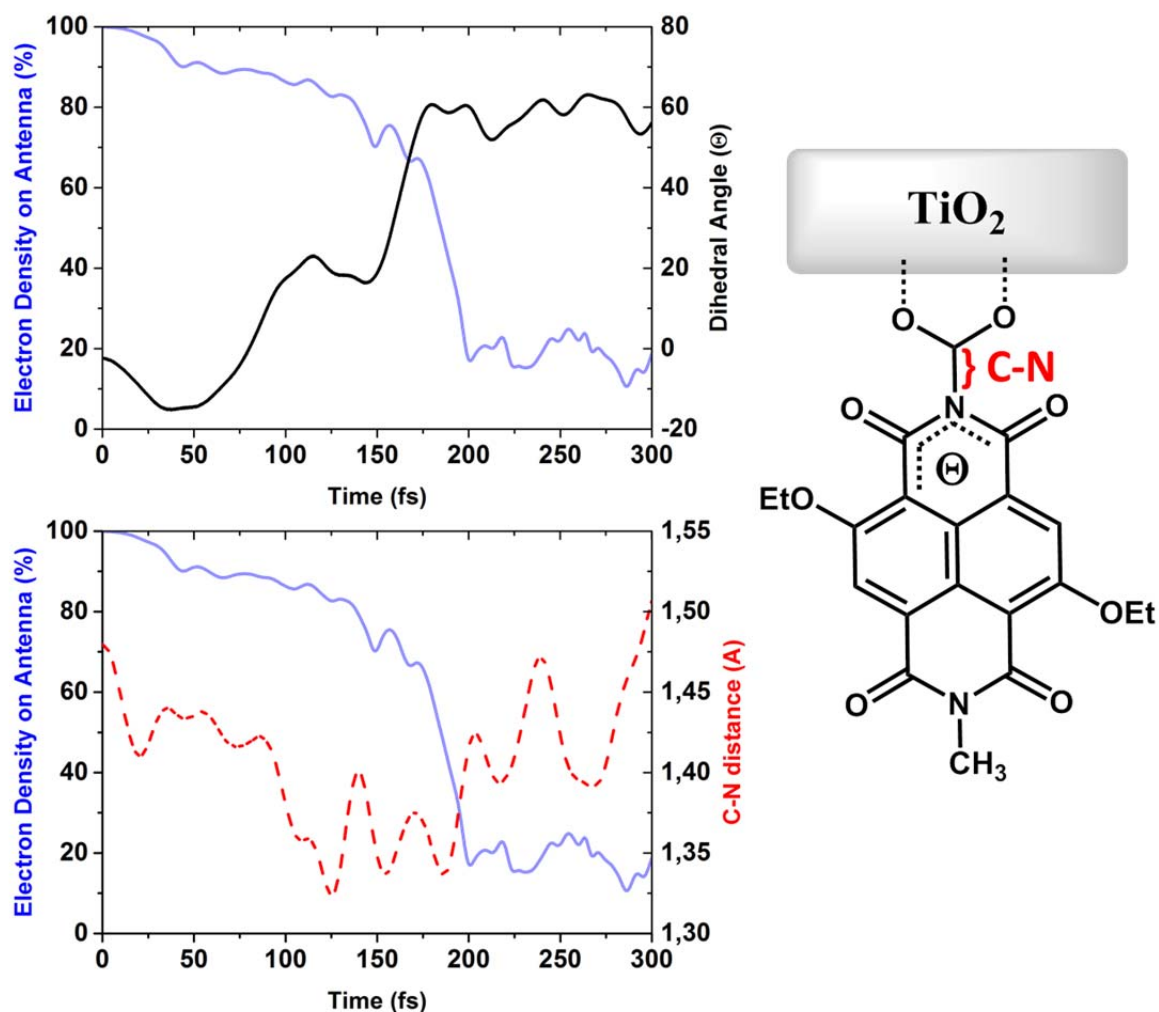


**Figure A5.1.** Top panel: Electron injection profile (blue line) plotted against the dynamical fluctuation of the dihedral angle  $\Theta$  (black line), along the ab-initio MD trajectory. Lower panel: the same electron injection profile is compared to the oscillations of the C-N bond (red dashed line) along the same MD trajectory. The two geometrical parameters used in the analysis are shown in the inset on the right hand side of the picture.

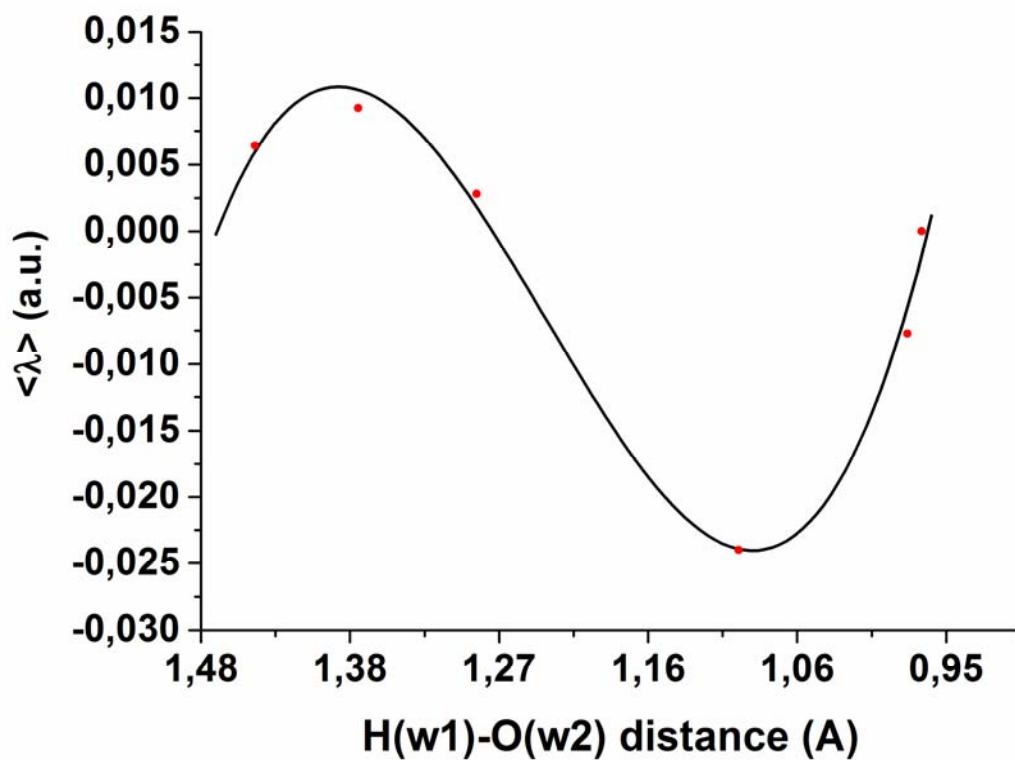


**Figure A5.2.** Average constraint force represented by the Lagrangian multiplier  $\langle \lambda \rangle$  (red dots) computed for each constrained MD simulation as a function of the reaction coordinate. A third order polynomial (black line) is used to fit all the six data points. It can be noted that the curve closely follows the data point with a determination coefficient  $R^2=0.96$ . The point at  $H(w1)-O(w2)=0.96$  Å corresponds to the equilibrium product state and thus its  $\langle \lambda \rangle$  is assumed to be 0. The point at  $H(w1)-O(w2)=1.37$  Å has been included in the data set to improve the polynomial fit around the maximum.



## Conclusions and Outlook

### **6.1. CONCLUSIONS**

To understand how to engineer molecular complexes able to achieve fast photoinduced unidirectional charge separation, static density functional theory calculations are performed on a series of molecular rectifiers employing the same PTZ donor, NDI<sub>1</sub> antenna, and NDI<sub>2</sub> acceptor subunits. The Marcus theory of electron transfer is used to predict the quality of the rectifiers, based on the calculated charge transfer rate constants.

All the molecular triads analyzed show absorption in the visible light spectrum leading to the formation of an excitonic state localized on the antenna. The Marcus parabolic terms  $\Delta G$  and  $\lambda$  between the exciton reactant state and product excited states with charge separated character are found to be dependent on the donor-antenna distance. At the same time, it is predicted that the electronic coupling between the donor and the acceptor is strongly influenced by the nature of the bridge units and by the strategy adopted to bind the bridges and the rectifier subunits. Molecular triads for fast charge separation can be then engineered by modifying the length and the nature of the bridge. Based on these findings, the complex PTZ-Ph-NDI<sub>1</sub>-C≡C-NDI<sub>2</sub> is proposed as a promising molecular rectifier for photoinduced direct ultrafast charge separation.

Quantum coherence effects due to the coupling of the electron-nuclear motion are observed to play a fundamental role during the process of heterogeneous electron transfer from a molecular chromophore, designed for unidirectional electron transfer, to a semiconductor surface. Nonadiabatic electron quantum dynamics simulations are performed within a quantum-classical framework, allowing the description of the electron transfer process on the ps time scale. It is observed that the electron transfer is not instantaneous, but rather proceeds gradually through strongly nonadiabatically coupled electronic states forming a coherent superposition. The energies of these states periodically cross each other due to resonant coupling with

specific nuclear vibrations. The photo-induced exciton reactant state localized on the chromophore is able to evolve into a product state localized on the semiconductor by selecting and coupling to specific nuclear vibrational modes that facilitate the electron transfer. Particularly, a rotational mode localized at the interface between the chromophore and the anchoring bridge is shown to open a preferential channel for the heterogeneous electron injection. When the channel is open, the evolution of the electronic wavepacket can proceed by coupling to the fast stretching modes that modulate the energy levels and the nonadiabatic coupling between the reactant and product states involved in the electron transfer.

Quantum-classical tight-binding nonadiabatic dynamics and density functional theory based *ab initio* MD simulations are used to investigate the first catalytic step in a fully solvated photoanode designed for solar water splitting. The photoexcitation leads to fast sub-picosecond electron injection from the sensitizing chromophore to the semiconductor electrode. The oxidized chromophore is then reduced to its neutral form by the water oxidation catalyst to which it is covalently bound. This process, leading to the first catalytic water splitting intermediate, occurs adiabatically via a proton-coupled electron transfer mechanism and has been estimated to take place on a sub-nanosecond time scale.

The presence of explicit solvent molecules surrounding the solute is found to be crucial for the catalysis. The water reorganization induces a stabilization of the catalytic intermediate, and provides the hydrogen bonding network necessary to accept and solvate a proton from the catalytically oxidized water molecule.

## **6.2. OUTLOOK**

Photoinduced electron transfer has a pivotal role in converting sunlight into power or solar fuel. Understanding the mechanisms that govern this process is thus essential to properly engineer devices for solar energy conversion.

Up until now, the Marcus theory of electron transfer<sup>1</sup> has been one of the most important theoretical tools for studying electron transfer processes and predict their rate constants. The quality of the materials for solar energy conversion is evaluated on the basis of the electron transfer rates obtained from Marcus theory. The design strategies for this type of materials are focused on optimizing the parameters entering the Marcus equation to increase the rate of electron transfer. The theory proposed by Marcus is fundamentally an equilibrium theory that considers reactant and product states at their equilibrium configurations. Thus, it can provide an accurate value for the electron transfer rate constant, but no information on the

microscopic mechanisms controlling the process. The major consequence of this methodological limitation is that material design and optimization are led by chemical intuition and trial and error approaches. This procedure could also be automatized by including a library of potentially useful building blocks and use genetic algorithms in combination with DFT to derive chromophores with specific optimized properties.

Recently, compelling evidences of quantum coherence effects driving electron transfer in artificial and natural systems have been reported<sup>2-6</sup>. The analysis of such processes requires to move from a static Marcus representation of reactant and product equilibrium states to the realm of nonadiabatic dynamics. By following the evolution of the electronic wavefunction in real time, it is possible to identify the vibrational modes driving the electron transfer process and use this information to improve the original design of a certain system. In this scenario, it would be interesting to perform such an investigation of the molecular charge separator proposed in chapter 3 to verify its predicted performances and further improve its design by accounting for the effects of coherent exciton-vibrational coupling.

The results reported in chapter 4 are obtained using a trajectory which is evaluated on the ground state potential energy surface. Using this result as a reference, it would be interesting to repeat the analysis by applying the Ehrenfest nonadiabatic dynamics method<sup>7</sup>. This comparison should provide information on the entity of the effect that the excited electronic wavefunction has on the nuclear motion, and thus on the necessity, or not, of using a trajectory evaluated on an excited state potential energy surface.

Finally, the results reported in chapter 5 for the photoanode for catalytic water splitting represent a very interesting starting point for the analysis of the entire catalytic cycle. The investigation of this complex should also be expanded to include structural modifications of the catalyst, the antenna and the anchoring unit aiming for rapid kinetics and optimal driving force for the catalytic and electron injection processes.

A risk associated with the current design of photoanode **1** is related to the possibility of exciton quenching by the electrons trapped at the TiO<sub>2</sub> surface along the catalytic cycle. This may be prevented by incorporating a molecular rectifier as separator between the antenna and the semiconductor. An obvious continuation of this work would be to integrate into the photoanode design the AM molecular rectifier, or one of its derivatives engineered to avoid charge recombination. The insertion of a molecular rectifier should elongate the lifetime of the charge separated state on a time scale sufficient to allow the different catalytic steps to take place.

Nonadiabatic simulations of the proton coupled electron transfer process will be

crucial to suggest structural modifications able to control the electron injection through the molecular rectifier and enhance the photodriven catalytic mechanism. Due to the required time scale of the simulation, the tight-binding semi-empirical method based on the Extended Hückel Hamiltonian used in chapter 4 and 5 would be extremely useful for such calculations.

### 6.3. REFERENCES

- (1) Marcus, R. A. On the Theory of Oxidation-Reduction Reactions Involving Electron Transfer. I. *The Journal of Chemical Physics* **1956**, *24* (5), 966–978.
- (2) Nieto-Pescador, J.; Abraham, B.; Gundlach, L. Photoinduced Ultrafast Heterogeneous Electron Transfer at Molecule–Semiconductor Interfaces. *J. Phys. Chem. Lett.* **2014**, *5* (20), 3498–3507.
- (3) Eisenmayer, T. J.; Buda, F. Real-Time Simulations of Photoinduced Coherent Charge Transfer and Proton-Coupled Electron Transfer. *ChemPhysChem* **2014**, *15* (15), 3258–3263.
- (4) Andrea Rozzi, C.; Maria Falke, S.; Spallanzani, N.; Rubio, A.; Molinari, E.; Brida, D.; Maiuri, M.; Cerullo, G.; Schramm, H.; Christoffers, J.; et al. Quantum Coherence Controls the Charge Separation in a Prototypical Artificial Light-Harvesting System. *Nat Commun* **2013**, *4*, 1602.
- (5) Falke, S. M.; Rozzi, C. A.; Brida, D.; Maiuri, M.; Amato, M.; Sommer, E.; Sio, A. D.; Rubio, A.; Cerullo, G.; Molinari, E.; et al. Coherent Ultrafast Charge Transfer in an Organic Photovoltaic Blend. *Science* **2014**, *344* (6187), 1001–1005.
- (6) Romero, E.; Augulis, R.; Novoderezhkin, V. I.; Ferretti, M.; Thieme, J.; Zigmantas, D.; van Grondelle, R. Quantum Coherence in Photosynthesis for Efficient Solar-Energy Conversion. *Nat Phys* **2014**, *10* (9), 676–682.
- (7) Curchod, B. F. E.; Rothlisberger, U.; Tavernelli, I. Trajectory-Based Nonadiabatic Dynamics with Time-Dependent Density Functional Theory. *ChemPhysChem* **2013**, *14* (7), 1314–1340.

# Summary

In 1912, the Italian biochemist Giacomo Ciamician expressed the hope for a future society in which coal would be substituted with solar energy. He wrote:

*"On the arid lands there will spring up industrial colonies without smoke and without smokestacks; forests of glass tubes will extend over the plains and glass buildings will rise everywhere; inside of these will take place the photochemical processes that hitherto have been the guarded secret of the plants, but that will have been mastered by human industry which will know how to make them bear even more abundant fruit than nature, for nature is not in a hurry and mankind is. And if in a distant future the supply of coal becomes completely exhausted, civilization will not be checked by that, for life and civilization will continue as long as the sun shines!<sup>1</sup>".*

More than a century later, we know a lot more about the *guarded secret of the plants* that is photosynthesis. However, there are still many open questions regarding how to translate this knowledge into the design of devices able to convert sunlight into power and fuel. Sunlight consists of discrete packets of energy called photons. In a similar way, matter can also be described in terms of quantum states possessing discrete energies. If one photon is equal to the energy difference between two quantum states of an object, energy can be exchanged between the sunlight and the object. In this case, it is said that the photon is absorbed and the object, or chromophore, is excited. The absorbed energy promotes the formation of an higher energy state of the chromophore called exciton state, in which an excited electron and a hole are strongly attracted to each other and remain localized in the same portion of space. This is the first step towards the conversion of sunlight into fuel and it is called light-harvesting process.

The exciton state cannot be used to generate fuel. To do so, the hole and the electron should be transferred in opposite directions towards respectively the water oxidation and the fuel evolving catalysts. A different quantum state has to be populated, in which the two charges are no longer bound. This state takes the name of charge separated state. An introduction to how charge separation is achieved in

(1) Ciamician, G. The Photochemistry of the Future. *Science* **1912**, 36 (926), 385–394.



natural systems and in artificial devices for sunlight conversion into electricity and solar fuel is presented in chapter 1.

Understanding the mechanisms that control the transition between the exciton and the charge separated state leading to solar fuel production is a fundamental question. The answer to this question can help to *master the photochemical process*.

This thesis is dedicated to the investigation of these mechanisms and to the identification of engineering principles that can be used to design materials able to control the process of photoinduced charge separation.

In chapter 3, the basic principles to follow when designing a molecular system for controlled charge separation are described. It is shown how the molecular elements to be included in the design can be chosen based on specific physical and chemical requirements, and how it is possible to systematically optimize the initial design by analyzing the effects of specific structural changes on the properties affecting the transition between exciton and charge separated state. This strategy, however, is based on a trial and error approach and strongly relies on personal chemical intuition regarding the structural modifications to introduce.

In chapter 4, the photoinduced electron injection from a chromophore to a semiconductor, which is one of the pivotal processes in solar energy conversion, is investigated. This analysis is extended beyond static calculations. Accounting for the motion of the nuclei is indeed crucial to gain insight into the mechanisms governing these processes in any material.

It is shown that the transition from the exciton to the charge separated quantum state proceeds through the propagating coherent superposition of the two states, and that this superposition is in resonance with specific nuclear vibrational motions. The quantum-classical simulations reveal that the electron injection proceeds coherently with selected vibrational motions at the interface between the reactant and the product quantum state. This investigation technique allows to draw conclusions on targeted structural modifications necessary to improve device performances. This dynamical analysis is therefore complementary to the design strategy described in chapter 3 and allows a less biased optimization of the materials.

Finally, in chapter 5, a photoanode for solar water splitting comprising the functions of light-harvesting, charge separation and catalysis is investigated. The system is designed by following the same principles used for the optimization of the triads. The components are selected to achieve both catalytic oxidation of water and fast charge separation from the chromophore to the semiconductor electrode. It is again observed that considering the system dynamics is necessary to understand the fundamental proton-coupled electron transfer mechanism driving the catalysis.

Additionally, it has been underlined the crucial role played by the solvent in creating the conditions for the catalytic reaction to occur.

In summary, it is shown that control over the photoinduced process of charge separation can be gained from careful materials design. Understanding the dynamics of these processes helps targeting structural modifications to improve the performances. Furthermore, it became clear that the explicit inclusion of the environment is fundamental for the description of photocatalytic processes.



# Samenvatting

In 1921, sprak de Italiaanse biochemist Giacomo Ciamician de hoop uit op een toekomstige samenleving waarin steenkool zou worden vervangen door zonne-energie. Hij schreef het volgende:

*“In dorre landen zullen industriële koloniën ontstaan zonder rook; Bossen van glazen buizen zullen zich strekken over de velden en glazen huizen zullen overal opduiken; daarin zal het fotochemische proces beginnen dat tot nu toe een bewaard geheim van planten is, maar dan nu ook door de mensheid zal worden beheerst. Wij zullen er meer profijt uit halen dan de natuur, omdat de natuur geen haast heeft maar men wel. En als er in de verre toekomst de voorraad steenkool volledig uitgeput zal zijn, zal de mensheid hier geen nadeel aan beleven, aangezien leven en beschaving zal voortbestaan, zolang de zon schijnt!<sup>1</sup>”.*

Meer dan een eeuw later weten we veel meer over dit bewaarde geheim van de planten dat fotosynthese is. Desalniettemin zijn er nog veel open vragen over het vertalen van deze kennis naar het ontwerpen van apparaten die het zonlicht kunnen omzetten naar energie en brandstof. Zonlicht bestaat uit kleine pakketjes energie genaamd fotonen. Op dezelfde manier kan materie ook omschreven worden in termen van kwantumtoestanden die uit discrete energieën bestaan. Als de energie van een foton gelijk is aan het energie verschil tussen twee kwantumtoestanden van een object, kan er uitwisseling van energie ontstaan tussen het zonlicht en het object. In dit geval wordt de foton geabsorbeerd en het object, de chromofoor, geëxciteerd. De geabsorbeerde energieën zorgen voor het ontstaan van een hoger energieniveau van de chromofoor, de aangeslagen toestand. Hierin zijn het elektron en het elektronengat sterk aangetrokken tot elkaar en blijven ze gelokaliseerd in het zelfde deel van de ruimte. Dit is de eerste stap richting het omzetten van zonlicht naar energie, we noemen dit het “light-harvesting process”.

De excitatie toestand kan niet gebruikt worden om energie op te wekken. Om dit wel te bereiken moet het elektronengat en het elektron verplaatst worden in

(1) Ciamician, G. The Photochemistry of the Future. *Science* **1912**, 36 (926), 385–394.

teggengestelde richtingen naar een respectievelijke water oxidatie en brandstof katalysator. Een andere kwantumtoestand moet worden opgevuld, waarin de twee geladen deeltjes niet meer verbonden zijn. Deze toestand wordt de ladingsgescheiden toestand genoemd. Een introductie hoe deze ladingsscheiding wordt gedaan in natuurlijke systemen en kunstmatig fotosynthese systemen om zonlicht om te zetten in elektriciteit en zonne-energie wordt gepresenteerd in hoofdstuk 1.

Het begrijpen van de verschillende mechanismes die controle hebben over de transitie tussen de aangeslagen toestand en de ladingsgescheiden toestand die kan leiden tot zonne-energie productie is een fundamentele kwestie.

Het antwoord op deze vraag kan helpen bijdragen tot het beter begrijpen van het fotochemische proces.

Dit proefschrift is toegewijd aan het onderzoek van deze mechanismes en het identificeren van de uitgangspunten die gebruikt kunnen worden om materialen te ontwerpen die het proces van foto-geïnduceerde ladingsscheiding kunnen controleren.

In hoofdstuk 3, zijn de basisprincipes beschreven die nodig zijn voor het ontwerpen van een moleculair system om ladingsscheiding te controleren. Er wordt omschreven hoe de moleculaire elementen in het ontwerp kunnen worden inbegrepen gebaseerd op hun specifieke fysieke en chemische eisen. Ook is er gekeken naar hoe het mogelijk is om het uiteindelijke ontwerp systematisch te optimaliseren door de effecten van structurele veranderingen tussen de excitatie toestand en de aangeslagen toestand te analyseren. Deze strategie is echter gebaseerd op een trial-and-error aanpak berust op persoonlijke chemische intuïtie met betrekking tot de structurele wijziging.

In hoofdstuk 4 wordt het injecteren van een elektron van de chromofor naar een semiconductor onderzocht, een van de meest belangrijke processen in de zonne-energie omzetting. Deze analyse gaat verder dan alleen de statische berekeningen. Rekening houden met de bewegingen van de nucleus is van cruciaal belang om inzicht te krijgen in het mechanisme om het toe te kunnen passen in andere materialen.

Het is bekend dat de transitie vanaf excitatie naar aangeslagen toestand gaat door het stimuleren van een coherente superpositie, en dat deze superpositie in resonantie is met de specifieke nucleaire vibratie. De kwantum-klassieke simulaties

laten zien dat de elektron injecties coherent zijn met de geselecteerde vibraties aan het oppervlakte tussen de reagent en de kwantumtoestand van het product. Deze onderzoekstechniek maakt het mogelijk om conclusies te trekken over gerichte structurele aanpassingen die nodig zijn om de systemen te verbeteren. Deze dynamische analyse is dus een aanvulling op de design strategie beschreven in hoofdstuk 3 en zorgt voor een minder bevooroordeeld optimalisatie van het materiaal.

Als laatste in hoofdstuk 5, wordt en een anode van een foto-elektrische cel voor het ontleden van water geanalyseerd. Deze anode heeft de functie van licht opvangen, katalyseren en lading scheiding. Het systeem is ontworpen met dezelfde principes die worden toegepast voor het optimaliseren van verschillende trio's van moleculen. De componenten zijn geselecteerd om zowel de katalytische oxidatie van water als de snelle lading scheiding van de chromofoor naar de semi-conductor elektrode te bereiken. Het is nogmaals geconstateerd dat de dynamiek van het systeem van belang is om het mechanisme van proton-gekoppeld elektronen transport van de katalysator te begrijpen. Daarnaast blijkt dat het oplosmiddel een onmisbare rol speelt in het creëren van de ideale condities voor een katalytische reactie.

Kort samengevat, er is aangetoond dat de controle van foto-geïnduceerde ladingsscheiding kan worden behaald door het zorgvuldig design van materialen. Het begrijpen van de dynamiek van dit proces helpt om gerichter structurele modificaties te maken om de systemen te verbeteren. Bovendien is het duidelijk geworden dat het meenemen van de omgeving van fundamenteel belang is voor het beschrijven van het foto-katalytische proces.

# Curriculum Vitae

## EDUCATION

---

### **Ph.D. in Computational Chemistry**

Leiden University

2011–2015

Supervisors: Dr. Francesco Buda and Prof. Dr. Huub J.M. de Groot.

***Thesis Title:** Taking Control of Charge transfer: strategic design for solar cells.*

### **MSc. in Physical and Theoretical Chemistry**

Leiden University

2008–2011

Research Supervisor: Dr. Alexander Kros.

***Thesis Title:** Synthesis of mesoporous silica nanoparticles for drug delivery.*

### **Minor in Science Based Business**

***Thesis Title:** Structure and role of technology transfer and use of intellectual property by research institutes.*

Research Supervisors: Dr. Domenico Golzio and Mr. Art Bos.

### **BSc. in Chemistry**

Università degli Studi di Milano-Bicocca

2005–2008

Research Supervisor: Dr. Alessandro Abbotto.

***Thesis Title:** Synthesis of Heteroaromatic Compounds for nonlinear optics.*

## SOFTWARES AND COMPUTER SKILLS

---

### Software for chemical modeling:

- Gaussian 09
- Car-Parrinello MD
- Amsterdam Density Functional
- Octopus
- NWCHEM

### Programming languages and OS

- FORTRAN
- UNIX
- BASH

## LANGUAGES

---

ITALIAN: **Native**

ENGLISH: **Fluent**

SPANISH: **Good**

DUTCH: **Basic**

FRENCH: **Basic**

## CONFERENCE PRESENTATIONS

---

- "Bio-Inspired Molecular Rectifier for Artificial Photosynthesis" *SolarFuel Tandem Network Meeting, 2011*  
**Oral Presentation**
- "In-Silico Design of Molecular Triads for Efficient Unidirectional Charge Separation" *NWO CW Study Group Meeting, 2014.*  
**Oral Presentation**
- "Quantum Dynamics of Electron Injection in a TiO<sub>2</sub> Dye-Functionalized Surface" *Physics@FOM, 2015.*  
**Oral Presentation**
- "Crucial Role of Nuclear Dynamics for Electron Injection in a Dye-Semiconductor Complex" *Holland Research School of Molecular Chemistry Symposium, 2015.*  
**Oral Presentation**
- "Nuclear Dynamics Driving Photoinduced Charge Transfer" *CHAIN meeting, 2015.*  
**Oral Presentation**





# List of Publications

- Monti, A., Negre, C.F.A., Batista, V.S., Rego, L.G.C., de Groot, H.J.M., Buda, F. "Crucial Role of Nuclear Dynamics for Electron Injection in a Dye–Semiconductor Complex" *Journal of Physical Chemistry Letters*, **2015**, vol. 6, pp. 2393–2398.  
**DOI:** 10.1021/acs.jpcllett.5b00876
- Monti, A., de Groot, H.J.M., Buda, F. "In-Silico Design of a Donor–Antenna–Acceptor Supramolecular Complex for Photoinduced Charge Separation" *The Journal of Physical Chemistry C*, **2014**, vol. 118, pp. 15600-15609.  
**DOI:** 10.1021/jp505105a
- Eisenmayer, T.J., Lasave, J.A., Monti, A., de Groot, H.J.M., Buda, F. "Proton Displacements Coupled to Primary Electron Transfer in the Rhodobacter sphaeroides Reaction Center" *The journal of physical chemistry B*, **2013**, vol. 117, pp. 11162–11168.  
**DOI:** 10.1021/jp401195t
- Monti, A., de Ruiter, J.M., de Groot, H.J.M., Buda, F. "Fully Atomistic Simulation of Solvent Mediated Proton-Coupled Electron Transfer Assisting Photodriven Water Oxidation" **2015**, manuscript to be submitted.
- de Ruiter, J.M., Monti, A., Purchase, R.L., van der Ham, C.J.M., Gullo, M. P., Joya, K.S., D'Angelantonio, M., Barbieri, A., Hetterscheid, D.G.H., de Groot, H.J.M., Buda, F. "Electrochemical and Spectroscopic Study of Mononuclear Ruthenium Water Oxidation Catalysts: A Combined Experimental and Theoretical Investigation" **2015**, under revision.